Fire Resilience in Steel-Concrete Structures Part II: Advanced Solutions

Course No: S03-033
Credit: 3 PDH

Roman Titov, P.E., C.C.M., LEED AP.

Continuing Education and Development, Inc.

P: (877) 322-5800
info@cedengineering.com

This course was adapted from the NIST U.S. Department of Commerce, Publication No. NIST TN 2203, "Fire Resilience of a Steel-Concrete Composite Floor System: Full-Scale Experimental Evaluation for Influence of Slab Reinforcement (Test #2)", which is in the public domain.

Abstract

The National Institute of Standards and Technology is conducting a series of large compartment fire tests to investigate the behavior and fire-induced failure mechanisms of full-scale composite floor assemblies with a two-story steel gravity frame, two bays by three bays in plan. This report presents the experimental design and results from the second composite floor fire experiment (Test #2).

Test #2 investigates the influence of the slab reinforcement on the structural integrity of the 9.1 m × 6.1 m steel-concrete composite floor subjected to combined mechanical loads and compartment fire exposure. The fire test bay was situated on the ground floor in the middle edge bay of the two-story test building. The floor slab in the test bay was reinforced with 9.5 mm diameter deformed bars placed 30 cm on center (230 mm^2/m). The test floor was hydraulically loaded to 2.7 kPa to mimic the code-prescribed gravity loads for fire conditions. Natural gas burners created a peak gas temperature exceeding 1100 °C below the test floor. The test fire lasted about 131 min, but the hydraulic loading was not removed until the test floor cooled down over 2 hours after the fire was extinguished. This experiment confirmed that the steel reinforcement played a vital role in maintaining the integrity of the composite floor under prolonged compartment fire exposure. The mid-panel vertical displacement increased at a rate less than 1 mm/°C as the protected steel beams were heated to 850 °C on average. The peak vertical displacement of the test slab was recorded 475 mm surpassing the displacement limit prescribed in the standard fire test. Although the test slab developed extensive surface cracks, it successfully contained the test fire underneath while sustaining the imposed loads. When the test floor was loaded again after it cooled down to room temperature, it retained the post-fire flexural strength exceeding 90 % of the ambient strength, calculated using the measured mechanical properties, of the composite secondary beam prior to fire exposure. The experimental results presented in this report can be used for validation of predictive models to perform parametric studies incorporating the variability in the steel reinforcement scheme (area, spacing, and material) for safer and cost-effective composite floor construction for fire safety.

Key words

Composite floors; Slab reinforcement, steel buildings; fire resistance; compartment fire experiments.

Preface

This work was conducted as part of the project "Measurement of Structural Performance in Fire" under the National Institute of Standards and Technology (NIST) Engineering Laboratory's Fire Risk Reduction in Buildings Program. We thank William Baker (Skidmore, Owings & Merrill), Craig Beyler (Jensen Hughes), Luke Bisby (University of Edinburgh), Ian Burgess (University of Sheffield), Charles Carter (AISC), Charles Clifton (University of Auckland), Michael Engelhardt (University of Texas), Graeme Flint (Arup), Nestor Iwankiw (Jensen Hughes), Kevin LaMalva (Warrington Fire), Roberto Leon (Virginia Tech.), and Amit Varma (Purdue University) for their expert consultation. We also thank the NIST colleagues including William Grosshandler, Laurean DeLauter, Philip Deardorff, Marco Fernandez, Michael Selepak, Fahim Sadek, Joseph Main, Jonathan Weigand, and Mina Seif for their significant contributions to the design, construction, and execution of this test series.

Table of Contents

1. Introduction 9
1.1. Background 9
1.2. Composite Floor Test #1 11
1.3. Scope and Objectives 13
2. Experimental Design & Construction 14
2.1. Fire Test Setup 14
2.2. Design Basis of Composite Floor Test #2 16
2.3. Composite Floor Design and Construction 17
2.3.1. Mechanical Properties of Steel Components 20
2.3.2. Fireproofing Insulation 21
2.4. Concrete Placement and Curing 22
2.4.1. Mixture Design 22
2.4.2. Concrete Placement 22
2.4.3. Curing Conditions 23
2.4.4. Hardened Concrete Properties 25
2.5. Instrumentation & Measurement Uncertainty 27
3. Test Results 30
3.1. Test Protocol 30
3.2. Fire Test Condition 32
3.2.1. Mechanical Loading 32
3.2.2. Test Fire 33
3.3. Thermal Response 36
3.3.1. Concrete Slab and Steel Reinforcing Bars 36
3.3.2. Composite Beam and Girder 38
3.3.3. Beam-End Connection 39
3.4. Structural Response 42
3.4.1. Vertical Displacement 42
3.4.2. Horizontal Displacement 45
3.5. Post-Fire Residual Capacity 47
3.6. Post-Test Inspection 48
3.6.1. Concrete Slab 48
3.6.2. Steel Deck and Beams 50
3.6.3. Steel Connections 52

4. Summary and Conclusions 53
References 55
Appendix A: Instrumentation, Raw Data, and Photographs 57
A.1. Mechanical Loading 57
A.2. Gas Temperature 59
A.3. Concrete Temperature 61
A.4. Reinforcing Bar Temperature 64
A.5. Composite Section Temperature 66
A.6. Steel Beam and Girder Temperature 69
A.7. Steel Connection Temperature 71
A.8. Displacement 76
A.9. Additional Strain Measurements 78
A.10. Compartment Opening Velocity and Temperature 82
A.11. Additional Post-Test Photographs 85
A.12. High-Temperature Discoloration of SFRM 89

List of Tables

Table 1. Steel reinforcement in concrete slabs specified in design standards and used in research. 10
Table 2. Measured mechanical properties of steel components. 20
Table 3. Design and measured thickness of SFRM. 21
Table 4. Concrete design mixture proportions. 22
Table 5. Matrix of measured concrete properties. 25
Table 6. Fresh concrete properties. 26
Table 7. Hardened concrete properties for each truck. 26
Table 8. Average hardened concrete properties. 26
Table 9. Estimated measurement uncertainty. FSO_E = maximum measured values; N = number of samples used for estimating random errors 28
Table 10. Timeline of Test #2 on March 10th, 2021. 30
Table 11. Measured total heat release and fuel load density. 33
Table 12. List of thermocouples used to estimate the average temperatures plotted in Fig. 20. 62
Table 13. List of thermocouples used to estimate the average temperatures plotted in Fig. 21a. 63
Table 14. List of thermocouples used to estimate the average bar temperatures plotted in Fig. 21b. 65
Table 15. List of thermocouples used to estimate the average temperatures of composite beams and girders plotted in 69

List of Figures

Fig. 1. (a) Compartment fire test in the south middle bay of the two-story building under 20 MW exhaust hood; (b) Composite floor soffit exposed to natural gas fueled compartment fire. 12
Fig. 2. Still image showing top of the Test #1 composite floor developing slab breach at 106 min after burner ignition. 13
Fig. 3. (a) Photograph of the two-story test frame and (b) scale drawing of floor plan. Units are in cm. 14
Fig. 4. Scale drawings of (a) south wall with main ventilation opening and (b) mechanical loading arrangement. Units are in cm. 15
Fig. 5. Slab reinforcement (a) Test #1 and (b) Test #2. 16
Fig. 6. Scale drawings of connection details in the test bay. Units are in inches. 17
Fig. 7. Scale drawings of composite floor beams in the test bay. Dimensions are in inches and rounded to the nearest tenth. 18
Fig. 8. Photographs of Test #2 floor specimen: (a) steel work; (b) beam-to-column connections; (c) beam-to-girder connections prior to fireproofing insulation. 18
Fig. 9. Scale drawings of slab reinforcement. Dimensions are in inches. 19
Fig. 10. Top of test floor assembly prior to concrete placement. 20
Fig. 11. Air temperature and relative humidity in test hall. 23
Fig. 12. Temperature in the test specimen and surrounding bays. 24
Fig. 13. Relative humidity in the test specimen and surrounding bays. 24
Fig. 14. Snapshots from the test video showing (a) inside the test compartment at ignition of the burners and (b) top of the test floor specimen at 120 min after the burner ignition. 31
Fig. 15. (a) Average load applied by a single actuator and (b) stroke displacement of the north actuators (DispNE and DispNW) and the south actuators (DispSE and DispSW). 32
Fig. 16. Heat release data (HRRburner and HRR) measured (a) first 30 min and (b) during entire heating. 33
Fig. 17. Snapshots of the video showing inside the test compartment with the times recorded following the burner ignition. 34
Fig. 18. Front view of the main vent opening of the fire test compartment during Test #2. .. 34
Fig. 19. (a) Averaged values and standard deviation of the upper layer gas temperatures measured using TCC channels and (b) gas temperatures measured at 100 cm, 200 cm, 300 cm from the floor of the test compartment along with the average upper layer gas temperature (AvgULG). 35
Fig. 20. Average temperatures of (a) 15.9 cm deep sections and (b) 8.3 cm deep sections of the test floor slab. Error bars indicate the maximum standard deviation of temperatures recorded from multiple thermocouples installed at the same distance from the steel deck. Dimensions are in cm. 37
Fig. 21. (a) Average temperature measured 3 mm below the top (unexposed) surface of composite slab and (b) average temperatures of No.3 deformed bars within the test floor slab. 37
Fig. 22. Locations of thermocouple probes within the 9.1 m composite beam and the 6.1 m composite girder at midspan. Dimensions are in cm. 38
Fig. 23. Average temperatures of (a) 9.1 m composite beam and (b) 6.1 m composite girder at midspan. The error bars indicate the maximum standard deviation of temperature readings at different sections. 39

Fig. 24. Typical locations of temperature measurements in the beam-end (left) and girder-end (right) connection regions. 39
Fig. 25. Average temperatures of the beam-end connections of (a) north edge beam, (b) secondary beam, and (c) south edge beam with W16x31 shapes. Error bars indicate a maximum value of standard deviation of temperatures measured at multiple locations. 40
Fig. 26. Average temperature of (a) east girder end connection and (b) west girder end connection attached to W18x35 shapes. Error bars indicate a maximum value of standard deviation in temperatures measured at multiple locations. 41
Fig. 27. Location of the vertical displacement (VD) measurements. Dimensions and coordinates are in cm. 42
Fig. 28. Measured vertical displacements as a function of (a) fire exposure time and (b) bottom flange temperatures of the floor beams. 43
Fig. 29. Video image showing top of the test floor at 120 min after fire ignition. 43
Fig. 30. Vertical displacement profile of the test floor assembly at (a) the north-south centerline and (b) the east-west centerline. The upper horizontal axes indicate the corresponding position of each vertical displacement sensors. 44
Fig. 31. Location of horizontal displacement (HD) measurements. The Z datum is defined at the laboratory strong floor. Coordinates are in cm. 45
Fig. 32. Measured lateral displacements of the exterior columns. 45
Fig. 33. Measured horizontal displacements as a function of bottom flange temperatures; (a) thermal elongation and contraction in the east-west direction and (b) thermal elongation and contraction in the north-south direction. 46
Fig. 34. (a) Initial bending stiffness and (b) load-displacement relationship during the post-fire loading test. 47
Fig. 35. Post-test photographs of the test floor slab, including closeups of concrete damage at locations 2 through 7. 49
Fig. 36. Post-test photograph of the floor specimen soffit. 50
Fig. 37. Closeup photographs of steel damage at locations 1 through 6 shown in Fig. 36. 51
Fig. 38. Post-test photographs of the standard shear tab connections of the north edge beam (top) and the extended shear tab connections of the east girder (bottom). 52
Fig. 39. Screenshot of the test video to monitor hydraulic actuators at the basement of the NFRL strong floor (prior to fire testing). 57
Fig. 40. Locations of (a) loading points tied to four hydraulic actuators (NE, NW, SE, SW) and (b) strain gauges installed at midspan of the test bay floor beams. Dimensions are in cm. 57
Fig. 41. Actuator data: (a) mechanical force and (b) stroke displacement of four hydraulic actuators (NE, SE, NW, and SW) used in the test. 58
Fig. 42. Beam strains prior during the ambient temperature mechanical loading: (a) secondary beam and (b) girders at midspan in the test bay. 58
Fig. 43. Locations of thermocouple probes used for gas temperature measurements within the fire test bay. The Z datum of NorthTC and SouthTC probes is at top surface of the compartment floor. Dimensions and coordinates are in cm. 59
Fig. 44. Photographs of installed TCC1 and SouthTC probes. 60
Fig. 45. Gas temperatures inside the test compartment. Fire was extinguished at 131 min. 60
Fig. 46. Locations of thermocouples installed within the test floor slab. Dimensions and coordinates are in cm. 61

Fig. 47. Concrete temperatures through the depth of the test floor slab. Fire was extinguished at 131 min. 62
Fig. 48. Locations of thermocouple probes used for temperature measurements of top (unexposed) surface of the test floor slab. Dimensions and coordinates are in cm. 63
Fig. 49. Top surface temperatures of the test floor slab. Fire was extinguished at 131 min. . 63
Fig. 50. Screenshots of the test video showing the west half of the test slab captured at 15 min, 45 min, 70 min, and 120 min following the fire ignition. 64
Fig. 51. Distribution of thermocouple probes mounted on No.3 deformed bars. Dimensions and coordinates are in cm. 64
Fig. 52. Temperatures of No.3 deformed bars placed inside the test floor slab. 65
Fig. 53. Photographs of typical thermocouples installed in the composite girder near its midspan. 66
Fig. 54. Labels and locations of the group of thermocouples installed at the midspan composite beams (W16×31) and girders (W18×35). Dimensions and coordinates are in cm. 66
Fig. 55. Locations of individual thermocouples mounted at midspan of W16×31 composite beams, where i = thermocouple group number, 2, 6, or 11. Dimensions are in cm. 67
Fig. 56. Locations of individual thermocouples mounted at midspan of W18×35 composite girders, where i = thermocouple group number, 13 or 16. Dimensions are in cm. 67
Fig. 57. Measured temperatures of midspan composite beam and composite girder sections in the test bay 68
Fig. 58. Locations of thermocouples mounted on steel beams and girders of the test floor assembly. Dimensions and coordinates are in cm. 70
Fig. 59. Measured temperatures of steel beams and girders. Fire was extinguished at 131 min. 70
Fig. 60. Locations of thermocouples mounted on the beam-end connection regions. Dimensions and coordinates are in cm. 74
Fig. 61. Measured temperatures of the beam-end connection regions. Fire was extinguished at 131 min. 75
Fig. 62. Additional displacement data not included in Sect. 3.4. 76
Fig. 63. Video snapshots showing the test floor at 15 min and 120 min after fire ignition.... 77
Fig. 64. (a) Locations and labels of strain measurements, (b) strain gauges installed at column base, and (c) strain gauges on the surrounding beams at the test floor level. Dimensions are in cm. 79
Fig. 65. Strains of test bay columns. 80
Fig. 66. Strains of surrounding columns (top) and steel beams (bottom). 81
Fig. 67. Locations of opening velocity and temperature measurements. NO3 is located in the NE vent opening (not shown here). Dimensions and coordinates are in cm. 82
Fig. 68. Installed bi-directional probes and thermocouples on south and north vent openings of the test compartment during fire loading. 83
Fig. 69. Vent opening temperatures and gas velocities. Plotted are the moving average values over 120 s. 84
Fig. 70. Post-test photographs of headed studs after concrete removal: (a) Northwest steel decking; (b) Secondary beam; (c) North edge beam; (d) South edge beam. The beam-end stud is in a red color ring 85

Fig. 71. Post-test photographs of shear tab connections: (a-b) secondary beam, (c) north beam, and (d) east girder. Fireproofing was removed manually. 86
Fig. 72. Post-test photographs: Secondary beam. 86
Fig. 73. Post-test photographs: South edge beam. 87
Fig. 74. Post-test photographs: North edge beam. 87
Fig. 75. Post-test photographs: Test-bay girders (left) and north and south ends of the west girder (right). 88
Fig. 76. Post-test photographs: West girder with rupture of the bottom web toe. 88
Fig. 77. Samples of fire exposed SFRM applied on the support steel beam framing. 89
Fig. 78. Chemical compositions of SFRM samples measured using a handheld XRF analyzer 89

List of Acronyms and Abbreviations

AISC	American Institute of Steel Construction
ASTM	American Society for Testing and Materials
ASCE	American Society of Civil Engineers
ANSI	American National Standards Institute
EC	Eurocode
IBC	International Building Code
ICC	International Code Council
UL	Underwriters Laboratories Inc.
ISO	International Organization for Standardization
NFPA	National Fire Protection Association
NFRL	National Fire Research Laboratory
NIST	National Institute of Standards and Technology
WTC	World Trade Center
SCI	Steel Construction Institute, United Kingdom
SCNZ	Steel Construction New Zealand
SFRM	Sprayed Fire Resistive Material
WWR	Welded Wire Reinforcement

1. Introduction

1.1. Background

Steel-concrete composite floors are widely used in modern steel buildings because of their cost effectiveness for spanning large open spaces. However, passive fire protection design of composite floors, regardless of their size and geometry, is mainly based on prescriptive fire-resistance rating of small-scale assemblies tested following the century-old fire testing standard. Even though this prescriptive approach provides the advantage of lower design cost as well as well-known construction cost, it (1) incurs high fire protection costs, (2) seldom provides a technical basis for risk-informed design decisions, and (3) can hinder industry innovation in fire protection and structural design of multistory complex buildings.

Over the last few decades, significant research efforts have been made to better understand the integrity of full-scale composite floor systems under fire loading. The Cardington test program [1, 2] in Europe, which was performed in an eight-story steel-framed building, demonstrated that the fire resilience of composite floor systems was superior to that observed in standard fire tests on isolated composite beams. Membrane action of the composite slabs was observed as secondary load-carrying mechanism after the support beams lost their flexural capacity at extremely high temperature. These findings led to the possibility of eliminating fire protection of the secondary (filler) beams and the development of simplified design methods [3–5] accounting for the load-displacement relationship of composite floor assemblies in tensile membrane action at elevated temperatures. Both the FRACOF [6] and COSSFIRE projects [7] further examined the benefit from membrane action by conducting standard fire tests on full-scale composite floor assemblies with the bare steel secondary beams. These tests indicated that the increased amount of steel reinforcement in composite slabs can significantly enhance their fire resistance beyond a specified rating period. Adequate lap splices of steel reinforcement in the concrete slab were recommended to develop tensile membrane action at large vertical displacement and to provide a load path to the surrounding structure.

The fire performance of reinforced concrete slabs and their failure characteristics associated with the amount of steel reinforcement were further investigated by conducting furnace testing of small-scale floor specimens with simply supported slab edges. Lim and Wade [8] tested two-way concrete slabs subjected to an imposed gravity load of 3 kPa and ISO 834 [9] standard fire exposure. The 3.3 m × 4.3 m flat slab specimens varied with the steel reinforcement area ranging from 198 mm^2/m to 565 mm^2/m. This study showed that the specimen with high reinforcement ratio exhibited only the surface cracks while the slab with smaller reinforcement ratio showed full-depth cracks at the same fire exposure time. Bailey and Toh [10] tested 20 mm thick flat slabs with two different sizes (1.2 m × 1.2 m versus 1.8 m × 1.2 m) to verify the applicability of a simple design method used to predict the displacement of heated concrete slabs undergoing tensile membrane action. The slab specimens were reinforced with mild steel mesh providing a ductility ranging from 1 % to 10 % and with stainless steel with a ductility of 31 % to 56 %. The reinforcement area varied from 45 mm^2/m to 155 mm^2/m. The study showed that (1) the aspect ratio of the slab affected the location of the concrete fracture lines in the slab: rectangular slabs failed by transverse concrete fracture at mid panel, whereas the square slabs exhibited concrete fracture either along the transverse or longitudinal spans, (2) the larger reinforcement area helped to increase failure time at elevated temperatures, and (3) the slab including steel reinforcement

with low ductility developed a sudden (brittle) failure mechanism. These small-scale tests demonstrated that the steel reinforcement scheme allowing tensile membrane action of the heated slabs played a significant role in preventing or delaying a collapse mechanism following the substantial reduction in flexural strength at high temperature.

A significant variation exists in steel reinforcement requirements for composite slabs with steel decking in current construction practice. Table 1 shows a summary of the minimum steel reinforcement prescribed in building design standards as well as that used in previous large-scale fire experiments which demonstrated superior fire resilience of composite floors exposed to structurally significant fires. In the United States (US), the Steel Deck Institute standard (ANSI/SDI C-2017) [11] specifies a minimum required shrinkage reinforcement ratio of 0.075 % for a composite floor slab with steel decking. The Underwriters Laboratories testing standard (UL 263) [12], essentially identical to the ASTM E119 standard [13], allows using a similar reinforcement area for standard furnace testing to determine a fire rating of small-scale composite floor or beam assemblies. The British standard, SCI-P56 [14], permitted a minimum slab reinforcement of 142 mm^2/m for the fire resistance design of composite floors with steel decking. The same amount of steel reinforcement was used in the Cardington test program. The post-Cardington large-scale experiments (e.g., FRACOF and COSSFIRE projects) used the reinforcement ratio designed using Bailey's method [3–5], ranging from 0.26 % to 0.33 %. The steel reinforcement ratio of composite slabs permitted in the US practice is considerably lower than that used in prescriptive or performance-based design of composite floors (incorporating tensile membrane action) used elsewhere. The floor integrity provision in the US fire testing standard tends to focus on the heat transfer aspect only (i.e., delaying the unexposed surface temperature by passive fire protection measures), not specifically accounting for the concrete damage associated with structural responses (i.e., excessive vertical displacements) of composite floors to fire. It is noteworthy that the fire resistance design in the US does not consider the slab reinforcement as a factor to determine fire resistance and is not always based on the displacement limit specified in the furnace testing standard.

Table 1. Steel reinforcement in concrete slabs specified in design standards and used in research.

Standard or Test Name	Reinforcement area	Reinforcement ratio*	Reinforcement details
ANSI/SDI C-2017 [11]		0.075 %	
SCI-P56 [14]	142 mm^2/m		6 mm mesh reinforcement at 200 mm spacing
Cardington Tests 3, 4, 7 [1, 2]	142 mm^2/m	0.20 %	6 mm mesh reinforcement at 200 mm spacing
FRACOF [6]	256 mm^2/m	0.26%	7 mm mesh reinforcement at 150 mm spacing
COSSFIRE [7]	256 mm^2/m	0.33%	7 mm mesh reinforcement at 150 mm spacing

*Computed as the ratio between the cross-sectional area of a steel wire to the cross-sectional area of the topping concrete above the fluted steel deck per unit slab width.

As alternatives to a prescriptive approach, the US building design standards (e.g., AISC 360 Appendix 4 [15], ASCE 7 Appendix E [16], and ASCE Manual of Practice 138 [17]) offer a

variety of resources that allow engineers to adopt performance-based design of buildings in fire. However, numerical analyses used in performance-based design require validation against test data and experimental evidence of the extent of fire-induced structural damage during and after fire exposure. Previous studies mentioned above have provided useful insights into the capability of composite floors to activate membrane action in fire; however, the data and findings from those studies are more relevant to the European standard practice.

The National Institute of Standards and Technology (NIST) has launched a large-scale experimental campaign at the National Fire Research Laboratory (NFRL) to fill knowledge gaps in realistic fire-structure interaction and failure of composite floor systems. The expected outcome includes the technical data and experimental evidence necessary for benchmarking and validating predictive computational models and design tools used for performance-based design of structures in fire. Currently, the Phase II project is in progress, which involves a series of large enclosure fire experiments using the full-scale two-story steel building. In this experimental campaign, a variety of factors influencing the fire resilience of full-scale composite floor systems will be investigated, including the steel reinforcement used in composite slabs (concrete slabs with steel decking), passive fire protection scheme of steel floor framing, and structural layout (e.g., connection type, slab continuity, or floor plate geometry).

The first fire experiment (Test #1) was conducted on November 14th, 2019, to generate the baseline data for current US prescriptive approach applied to a full-scale building floor system and to compare with forthcoming experiments. Literature review, experimental design, measurement systems, and results of Test #1 are reported in Choe et al. [18]. An overview of Test #1 and key findings from this study are summarized in Sect. 1.2.

1.2. Composite Floor Test #1

The initial experiment, Test #1, investigated the structural performance and failures of the 6.1 m × 9.1 m composite floor system designed following the current US practice, incorporating prescriptive fireproofing insulation details to achieve the 2-hour fire-resistance rating and the minimum steel reinforcement (with a cross-sectional area per unit width, 60 mm^2/m) prescribed for shrinkage and temperature crack control of a composite slab (a concrete slab with fluted steel decking).

The full-scale two-story steel frame two bays by three bays in plan was used to mimic the realistic boundary conditions of composite floors when exposed to fire (Fig. 1). The fire test compartment (10 m × 6.9 m × 3.8 m) with the main opening (5.8 m × 1.5 m) on the exterior wall was situated in the south middle bay of the two-story test building. There was a 5.8 m × 0.3 m slit on the north wall designed for air intake only. Four natural gas burners (1 m × 1.5 m each in size and rated 16 MW total) distributed on the floor of the test compartment created standard fire exposure to the soffit of the composite floor in the test bay (Fig. 2). During fire exposure, the composite floor in the test bay was hydraulically loaded to 2.7 kPa which resulted in a total design gravity load of 5.2 kPa according to the ASCE 7 [16] load combination for fire conditions (1.2 × dead load + 0.5 × live load). The composite floors in the adjacent bays, which remained cool during fire loading, were loaded to 1.2 kPa (equivalent to 0.5 times live load) using water-filled drums. Over 300 data channels were used to characterize the fire testing conditions as well as thermal and structural responses of the two-story building to a test fire at a variety of locations.

(a) (b)

Fig. 1. (a) Compartment fire test in the south middle bay of the two-story building under 20 MW exhaust hood; (b) Composite floor soffit exposed to natural gas fueled compartment fire.

The natural gas fueled compartment fire produced the upper layer gas temperature (below the composite floor) closely following the temperature-time relationship used in standard fire testing. The peak gas temperature of 1060 °C was recorded when both the test fire and hydraulic loading was removed at 107 min. Temperatures of the protected steel beams in the test bay reached a peak value of 800 °C. The peak heat release rate and total heat energy was measured 10.8 MW and 63.5 GJ, respectively.

During fire, the heated composite floor (with imposed mechanical loads on top) continuously sagged, reaching the peak vertical displacement of 60 cm at 107 min. The 9.1 m long floor beams (W16×31) buckled at their ends due to large compressive forces induced by the restraint to thermal elongation. The exterior columns (W12×106) bent outward due to thermal expansion of the heated floor assembly, resulting in partial shear ruptures in some bolts connected to those columns.

Whereas temperatures of the protected steel beams were acceptable compared to the ASTM E119 [13] limiting temperatures, significant integrity failure (concrete cracks) occurred in the heated composite floor before attaining the specified fire rating period. Large concrete cracks appeared around the hogging moment region (next to the test-bay column gridline) less than 30 min into heating, and the mid-panel concrete cracks began to occur at 70 min, exposing the hot glowing steel deck beneath along the longitudinal centerline (Fig. 2).

The limited ductility of the heated composite slab was the primary cause of the integrity failure which might initiate fire spread above the compartment of fire origin and eventually lead to local collapse mechanisms during longer (uncontrolled) fires. The steel wire reinforcement (60 mm^2/m) embedded in the test floor slab ruptured in tension at critical locations as the thermally degraded composite floor sagged but before reaching the ASTM E119 displacement limit. The minimum steel reinforcement (60 mm^2/m) prescribed for concrete crack control in normal conditions and permitted in standard furnace testing may not be sufficient to maintain the integrity of a full-scale composite floor undergoing the 2-hour standard fire exposure.

Fig. 2. Still image showing top of the Test #1 composite floor developing slab breach at 106 min after burner ignition.

1.3. Scope and Objectives

This report presents the second experiment of the Phase II program (Test #2) conducted on March 10, 2021. This study is aimed to investigate the influence of the steel reinforcement on the structural performance of the full-scale composite test floor assembly subjected to combined mechanical and fire loading. The improvement in the fire resilience of the composite floor and failure characteristics associated with the slab reinforcement scheme are discussed.

The experimental measurements include:

- fire characteristics including heat release rates, gas temperatures, velocity flow of the openings, and heat fluxes from the natural gas fueled compartment fire,
- thermal (temperatures) and structural responses (displacements, forces, and strains) of the test building, and
- any noteworthy observations during the fire test and post-test inspections critical to understand the overall fire performance and failure modes of the test floor assembly.

This report offers the unique experimental results that provide insight into the effects of standard fire exposure in a real building structure and potential failure mechanisms of full-scale steel-concrete composite floor systems including steel frame connections and slab continuity. This technical information can be used to guide the development and validation of physics-based computational models of composite floor assemblies in fully developed fires as well as after fire is extinguished. This research effort also provides important steps toward the improvement of the current fire testing methods and performance-based design provisions for steel-framed buildings in fire.

2. Experimental Design & Construction

2.1. Fire Test Setup

Details of the two-story steel-framed building and the fire test setup are presented in Choe et al. [18] and summarized herein.

The fire test was conducted on the two-story steel gravity frame two by three bays in plan constructed below the 15 m × 14 m exhaust hood at the NFRL, as shown in Fig. 3. The test frame has the footprint of 1036 cm × 1768 cm (34 ft. × 58 ft.) with an average 366 cm (12 ft.) story height. Composite floors were constructed on the first-floor level, whereas the second-floor steel framing provided braces to the steel columns of W12×106 shapes. A 5 cm thick plate was welded to the base of each column and anchored to the laboratory strong floor using high-strength steel bars.

The fire test bay (687 cm × 1008 cm × 377 cm) was situated in the south middle bay of the test building on the ground floor, with the footprint slightly greater than the column grid size (610 cm × 914 cm). Enclosing walls (along the red lines in Fig. 3b) were constructed as non-load bearing walls made of sheet steel with Type-C gypsum board lining at the exposed surface. Columns were not directly exposed to fire except for the upper region where the floor beams or girders of the test bay were joined. Four natural gas burners (1 m × 1.5 m each and rated 16 MW total) on the ground floor were used to create realistic fire exposure to the soffit of the composite floor in the test bay. Purpose-built slab splices (along the blue lines in Fig. 3b) were designed to reuse the same surrounding floors throughout the test program, and therefore only the fire-exposed floor assembly was reconstructed new for each test.

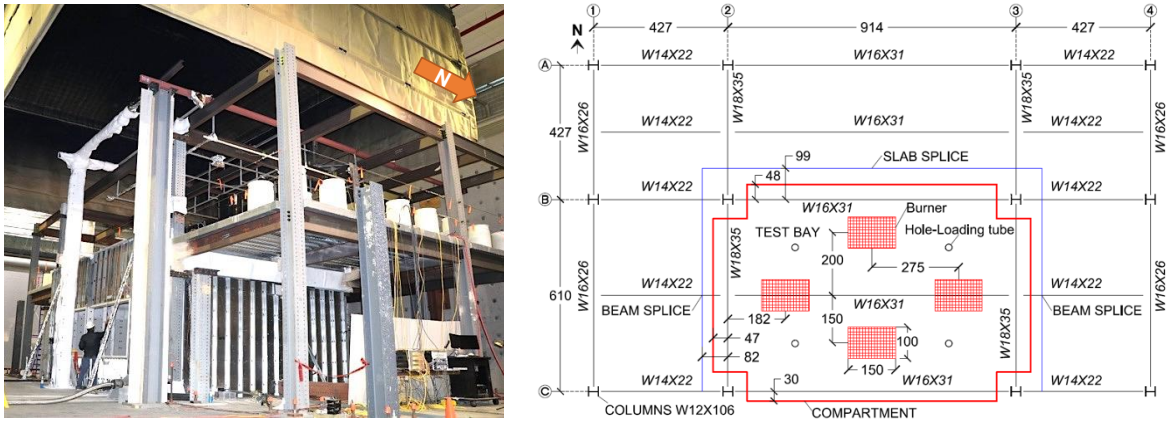

Fig. 3. (a) Photograph of the two-story test frame and (b) scale drawing of floor plan. Units are in cm.

The main ventilation opening was on the south exterior wall, approximately 150 cm tall × 582 cm wide as shown in Fig. 4a. There was a 30 cm tall × 582 cm wide slit on the north wall for air intake only. The height of the windowsill was 100 cm from the strong floor. The design basis of a test fire condition is presented in Zhang et al. [19].

The test-bay floor was hydraulically loaded to 2.5 kPa as imposed gravity loads during the test. The total gravity load (including the floor self-weight) was 5.2 kPa, which conforms to the gravity load demand determined from the ASCE 7 [16] load combination for

extraordinary events (1.2 times dead load plus 0.5 times live load). The surrounding floors were loaded by water-filled drums, providing an imposed gravity load of 1.2 kPa, equivalent to 50 % of an office live load as specified in the ASCE 7 standard. Fig. 4b shows the mechanical loading arrangement.

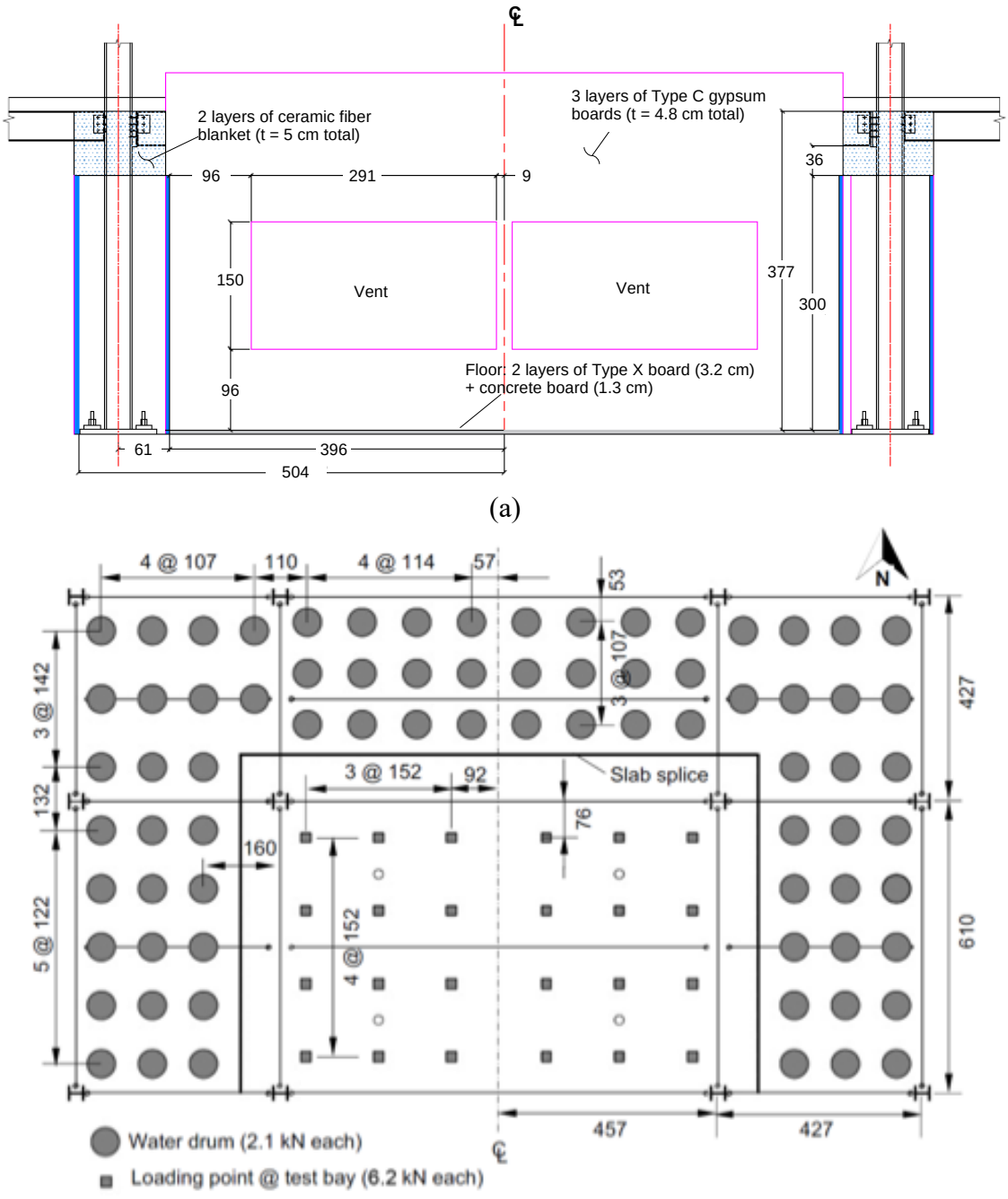

Fig. 4. Scale drawings of (a) south wall with main ventilation opening and (b) mechanical loading arrangement. Units are in cm.

2.2. Design Basis of Composite Floor Test #2

The primary difference between Test #1 and Test #2 was the steel reinforcement scheme used in the composite slab in the test bay. Test #1 demonstrated that the welded wire reinforcement (WWR) of 6×6 W1.4×W1.4 mesh mat (with a cross-sectional area of 60 mm^2/m slab width), shown in shown in Fig. 7a, was not sufficient to maintain slab integrity up to the specified rating period (2 h), with a potential risk of fire spread beyond the compartment of fire origin. Hence, for Test #2, it was decided to study the influence of the steel reinforcement on the fire resilience of the composite floor while other conditions remained mostly unchanged.

Since there is no specific guideline regarding the slab reinforcement requirements for standard fire testing in the US, the steel reinforcement ratio of 0.2 % in the floor slab was initially proposed for Test #2. This reinforcement ratio is similar to (a) the minimum required shrinkage reinforcement specified in the ACI 318 [20] provisions for reinforced concrete slabs and (b) the amount of the steel reinforcement used in the previous European studies where the test floor assemblies exhibited excellent fire resilience due to tensile membrane action at large vertical displacements.

With several iterations performed for the selection of slab reinforcement using the Slab Panel Method (SPM) [21] which has been used in the New Zealand (NZ) practice, the following two schemes were considered for the Test #2 design: (a) the 12×12 W9.1×W9.1 mesh mat (8.6 mm diameter cold formed plain steel wires with the spacing of 30.5 cm) with a reinforcement ratio of 0.23 % or (b) No.3 deformed reinforcing bars with the spacing of 30.5 cm in both orthogonal directions (9.5 mm diameter hot rolled deformed bars) with a reinforcement ratio of 0.28 %, shown in in Fig. 7b. Although the welded wire reinforcement is more commonly used in US composite floor construction, the 12×12 W9.1×W9.1 mesh mat has been rarely used and not available through local vendors. Hence, the No. 3 bars were proposed for Test #2. Deformed bars are often used in composite slabs to control cracks in the concrete caused by shrinkage and temperature effects during the curing period, to resist the tensile force in the hogging moment region, or to design diaphragms against lateral forces such as earthquake or wind [22].

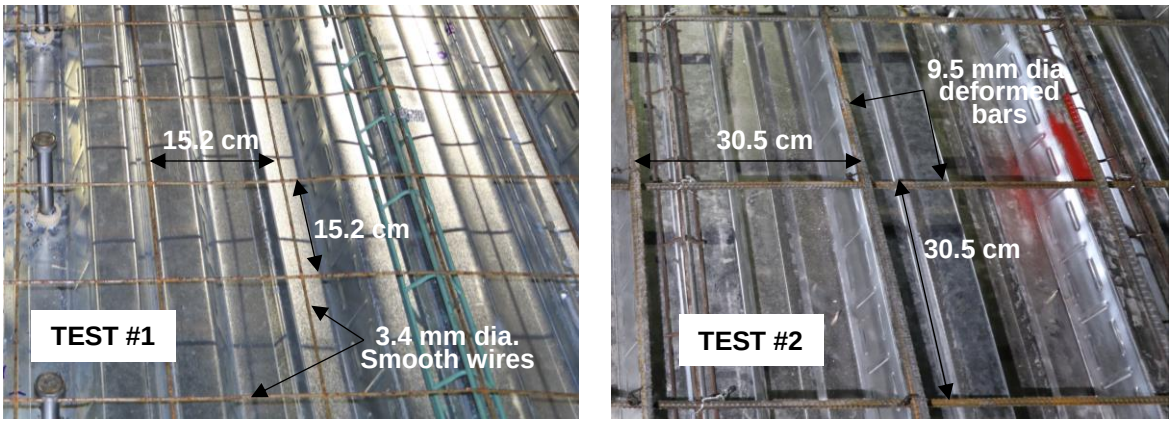

(a) (b)

Fig. 5. Slab reinforcement (a) Test #1 and (b) Test #2.

2.3. Composite Floor Design and Construction

The steel frames within the fire test bay consisted of three 914 cm (30 ft.) long W16×31 shapes and two 610 cm (20 ft.) long W18×35 shapes as shown in Fig. 3b. Refer to AISC Steel Construction Manual [23] for the dimensions of the steel shapes. The ends of the W16×31 beams were connected via standard shear tabs (PL8½×6×3/8) with three 1.9 cm (0.75 in.) diameter structural bolts whereas the W18×35 girders were connected to the webs of W12×106 columns using extended shear tabs (PL9-7/8×14½ ×3/8) with five 1.9 cm diameter structural bolts. The weld size used in the shear tab connections was 6.3 mm (0.25 in.). Short-slotted holes, 2.1 cm (13/16 in.) wide and 2.5 cm (1 in.) long, were drilled on the connecting elements, whereas the standard holes with the diameter of 2.1 cm were drilled on the webs of beams and girders. Details of the beam-end connections are shown in Fig. 6.

The composite floor was constructed with lightweight aggregate concrete and 7.6 cm (3 in.) deep profiled steel decking as shown in Fig. 7. The deck flute was oriented perpendicular to the 914 cm long beams. The topping concrete (above top ribs) was 8.3 cm (3.25 in.) thick as required to achieve the 2-hr fire resistance rating. Steel headed stud anchors with 19 mm shaft diameter were welded to the top flange of the W16×31 and W18×35 shapes at 30 cm (12 in.) and 36 cm (14 in.), respectively. The corresponding composite action was estimated to be about 65 % of the yield strength of steel shapes at ambient temperature. Photographs of the floor specimen soffit, beam framing, and connections are shown in Fig. 8.

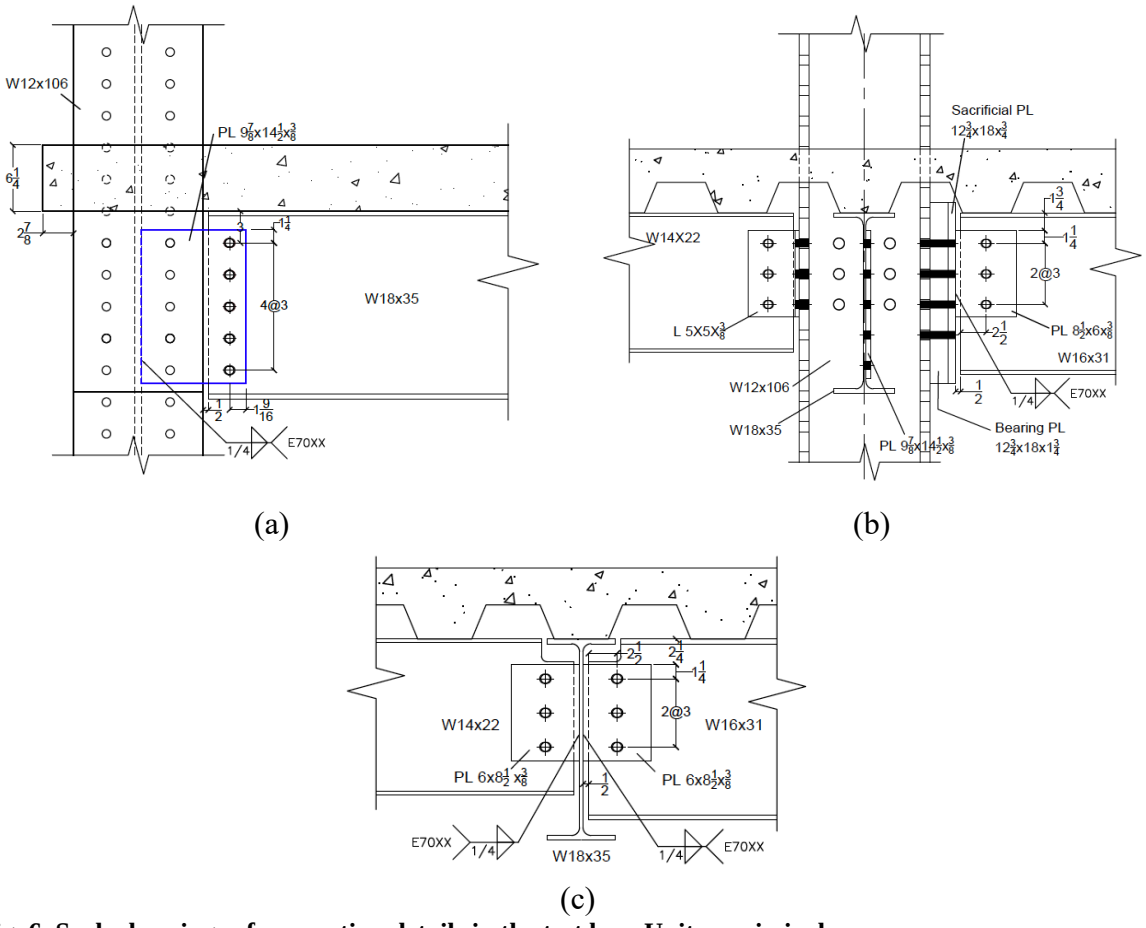

Fig. 6. Scale drawings of connection details in the test bay. Units are in inches.

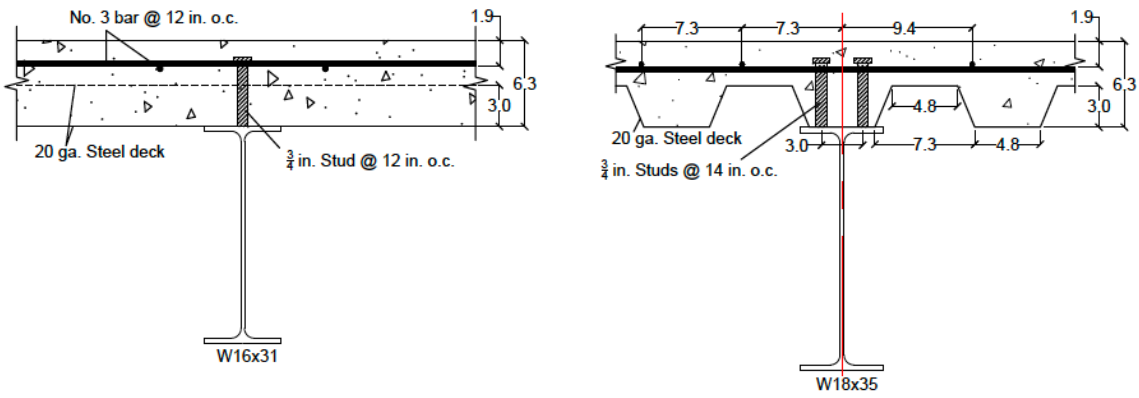

(a) (b)

Fig. 7. Scale drawings of composite floor beams in the test bay. Dimensions are in inches and rounded to the nearest tenth.

(a)

(b)

(c)

Fig. 8. Photographs of Test #2 floor specimen: (a) steel work; (b) beam-to-column connections; (c) beam-to-girder connections prior to fireproofing insulation.

The floor slab was reinforced with two layers of No. 3 deformed bars at 30 cm (12 in.) spacing on average as shown in Fig. 9. The spacing of some transverse bars above the W18×35 girders ranged from approximately 19 cm (7.5 in.) to 42 cm (16.5 in.) due to the bar

clear distance from support columns. The longitudinal bars had a clear cover of 4.8 cm (1.9 in.) from the top surface of the concrete, and the transverse bars had a clear cover of 3.8 cm (1.5 in.) from the top surface of the slab. The south ends of transverse bars had the 180-degree standard hooks to minimize separation of the concrete slab from the south edge beam during the fire test. Mechanical couplers were used within the test bay to splice the transverse bars at 99 cm (39 in.) from the centerline of the north edge beam and the longitudinal bars at 152 cm from the centerlines of the girders. These bars were also lapped with the 63.5 cm (25 in.) long No. 4 deformed bars extended from the slab splice line. A photograph of the test floor prior to concrete placement is provided in Fig. 10. Refer to Choe et al. [18] for the details of slab reinforcement in the surrounding floors.

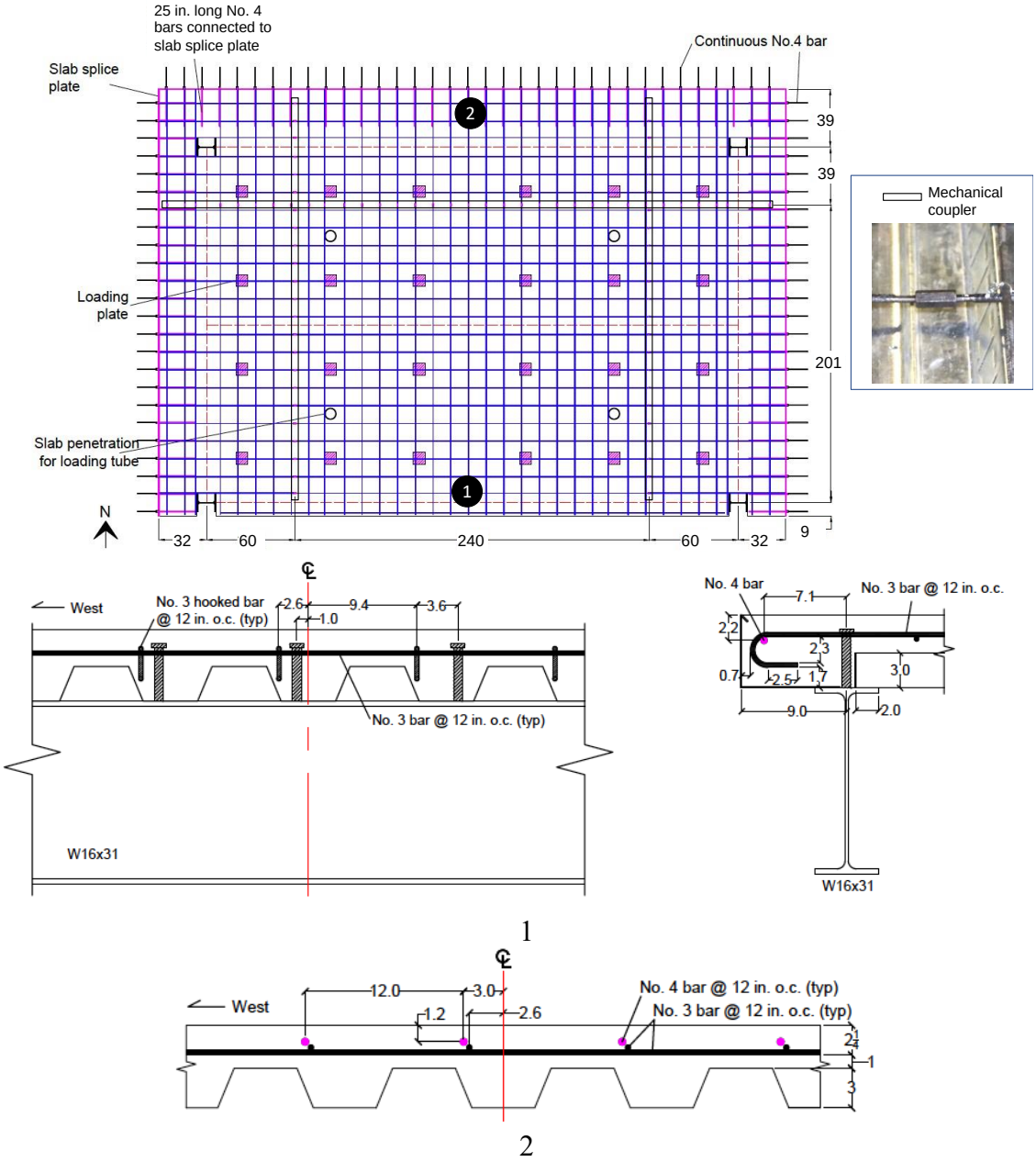

Fig. 9. Scale drawings of slab reinforcement. Dimensions are in inches.

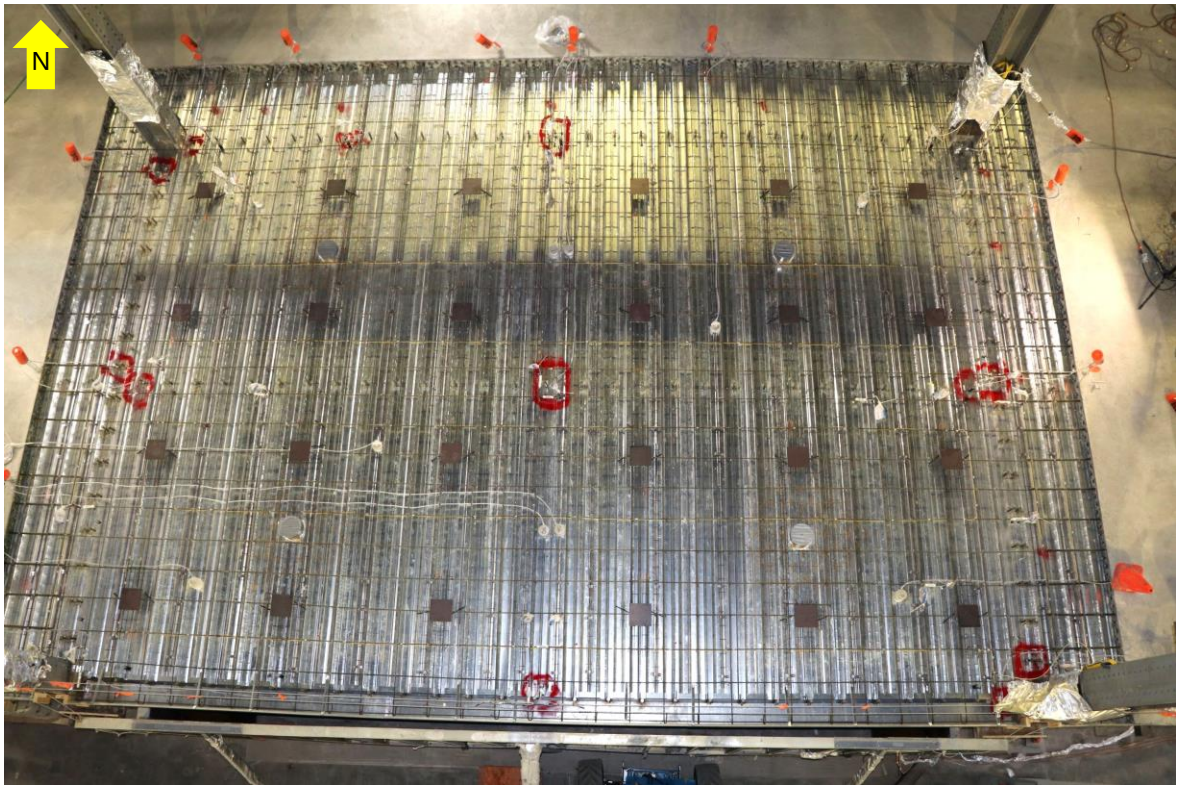

Fig. 10. Top of test floor assembly prior to concrete placement.

2.3.1. Mechanical Properties of Steel Components

The room-temperature mechanical properties of steel components constituting the test floor assembly were measured at a commercial testing facility. The fabrication of specimens (coupons) and testing procedures conformed to the ASTM E8/E8M [24] standard. Table 2 summarizes the average values of the 0.2 % offset yield strength (S_y), the ultimate tensile strength (S_u), and percent elongation at fracture (δ_u). The values after ± symbols indicate one standard deviation estimated using a uniform distribution of the two measured values.

Table 2. Measured mechanical properties of steel components.

Steel components	ASTM Designation	S_y (MPa)	S_u (MPa)	δ_u (%)
W16×31	A992	380 ± 50	500 ± 30	33 ± 5
W18×35	A992	360 ± 20	500 ± 6	33 ± 1
Shear tab plate	A36	290 ± 1	440 ± 30	37 ± 1
Headed stud anchor	A29	410 ± 2	510 ± 3	-
Structural bolt	A325 (F3125)	890 ± 10	970 ± 8	19 ± 1
Steel deck	A653	400 ± 4	470 ± 2	26 ± 1
No. 3 deformed bar	A615	480 ± 1	770 ± 2	22 ± 1

2.3.2. Fireproofing Insulation

The fire-exposed structural steel components were protected with a commercially available sprayed fire resistive material (SFRM), which was a cementitious gypsum-based material with a density ranging from 240 kg/m^3 to 350 kg/m^3. The thickness of the SFRM applied to steel substrate met the 2-hr fire-resistance rating requirement for Type IB construction in accordance with the IBC [25]. Table 3 shows the design and measured average values of the SFRM thickness. The values after ± are the coefficient of variation in the measurements.

Table 3. Design and measured thickness of SFRM.

Steel Component	UL Design No.	Design Thickness	Average Measured Thickness*
W16×31 (north primary beam)	N791	18 mm (11/16 in.)	20 mm ± 9 %
W16×31 (south primary beam)	N791	18 mm (11/16 in.)	21 mm ± 10 %
W16×31 (secondary beam)	D949	11 mm (7/16 in.)	14 mm ± 7 %
W18×35 (east girder)	N791	18 mm (11/16 in.)	22 mm ± 4 %
W18×35 (west girder)	N791	18 mm (11/16 in.)	21 mm ± 8 %
Standard shear tab (beam-end connections)	-	25 mm (1 in.)	26 mm ± 17 %
Extended shear tab (girder-end connections)	-	25 mm (1 in.)	33 mm ± 15 %

*The values after ± symbol are the coefficient of variation. The SFRM thickness measurement was performed at 81 discrete points on each beam and 6 to 9 discrete points on each end connection region.

2.4. Concrete Placement and Curing

2.4.1. Mixture Design

The concrete mixture was designed to provide a lightweight aggregate concrete with hardened mechanical properties typical of those used in current construction practice, but with a low propensity for fire-induced spalling. To reduce the likelihood of spalling, 2.37 kg/m^3 (4 lb/yd^3) of monofilament polypropylene microfibers were used in the mix as proposed in Maluk et al. [26]. To further reduce the chance of fire-induced spalling, expanded slate lightweight aggregate with low water-retention characteristics and high desorption was selected as suggested in Pour-Ghaz et al. [27], to expedite the reduction of moisture in the concrete during curing. The concrete design mixture proportion are provided in Table 4.

Table 4. Concrete design mixture proportions.

		water/cement: 0.41	Slump: 14.0±2.5 cm (5.5±1.0 in.)
	Material	Surface Saturated Dry, kg (lb)	Volume, m^3 (ft^3)
Cement:	ASTM C-150: Type I/II Lehigh	254 (560)	0.081 (2.85)
Fly Ash:	ASTM C-618: Separation Technologies Class F	64 (140)	0.025 (0.89)
Aggregate:	ASTM C-33: Carolina Stalite LTWT	404 (890)	0.269 (9.51)
Sand:	ASTM C-33: Chaney Sand	622 (1372)	0.240 (8.46)
Air:	2.5%	-	0.019 (0.67)
Water:	ASTM C-1602; ASTM C-1603	129 (284)	0.129 (4.55)
Admixture:	See details below	5 (10)	0.002 (0.07)
	Total	1477 (3256)	0.765 (27.00)
	Unit Weight kg/m^3 (pcf)	1932 (120.6)	
	Calculated Equilibrium Dry Density kg/m^3 (pcf)	1853 (115.7)	

Admixtures

FRC MONO-150 - 2.37 kg/m^3 (4 lb/yd^3)

Sika Visocrete 2100 - 1.75 ± 1.75 ml/kg (3 ± 3 oz/cwt)

Sika Plastocrete 161 - 2.91 ± 1.16 ml/kg (5 ± 2 oz/cwt)

SikaTard 440 - 1.16 ± 1.16 ml/kg (2 ± 2 oz/cwt)

Sika ViscoFlow 2020 - 2.33 ± 1.16 ml/kg (4 ± 2 oz/cwt)

2.4.2. Concrete Placement

The concrete was batched at a local ready-mix concrete plant and trucked to NIST for casting. A total of two trucks were used to cast the test floor slab. Although the design mixture proportions were the same for both batches (trucks), small adjustments were made by adding superplasticizer prior to the concrete placement. Immediately after casting, the concrete was covered with wet burlap to maintain a wet surface condition. The burlap was re-wet, as necessary, for the first 7 days of curing, after which the burlap was removed. The concrete in the surrounding bays had been cast on 6/4/2019 and remained in place.

2.4.3. Curing Conditions

The measured relative humidity and air temperature in the test hall where the specimens were cured from the date of casting until fire testing are plotted in Fig. 11.

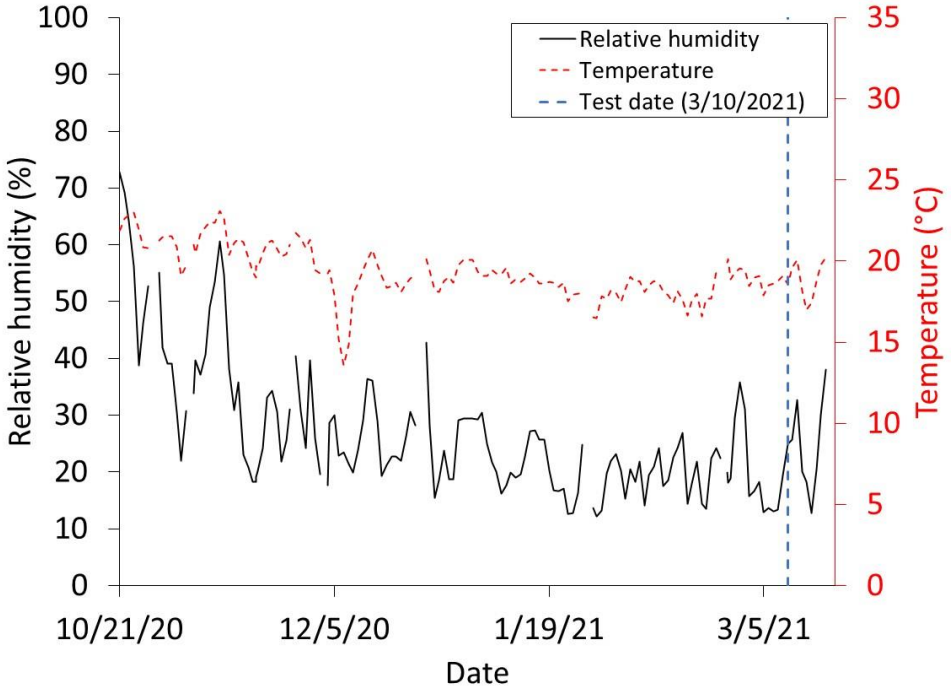

Fig. 11. Air temperature and relative humidity in test hall.

The relative humidity and temperature in the concrete during curing were measured using probes placed into perforated sleeves embedded in the concrete during casting. The manufacturer specified accuracy of the temperature and relative humidity in the applied temperature range are ± 0.2 °C and less than ± 2.5 %, respectively. The temperatures measured in the concrete are shown in Fig. 12 and the relative humidity measurements in Fig. 13. Measurement locations in the test specimen were in the southwest and northeast quadrants of the specimen to provide an indication of variation across the specimen. The measurement location for the surrounding bays was in the middle of the center north bay. No measurements were made in the surrounding bays until the time of testing. Therefore, the relative humidity in the concrete in the surrounding bays is significantly lower than in the test specimen. The moisture content of the specimens, which is related to the relative humidity, was measured separately on concrete cylinders cured under the same conditions as the slabs.

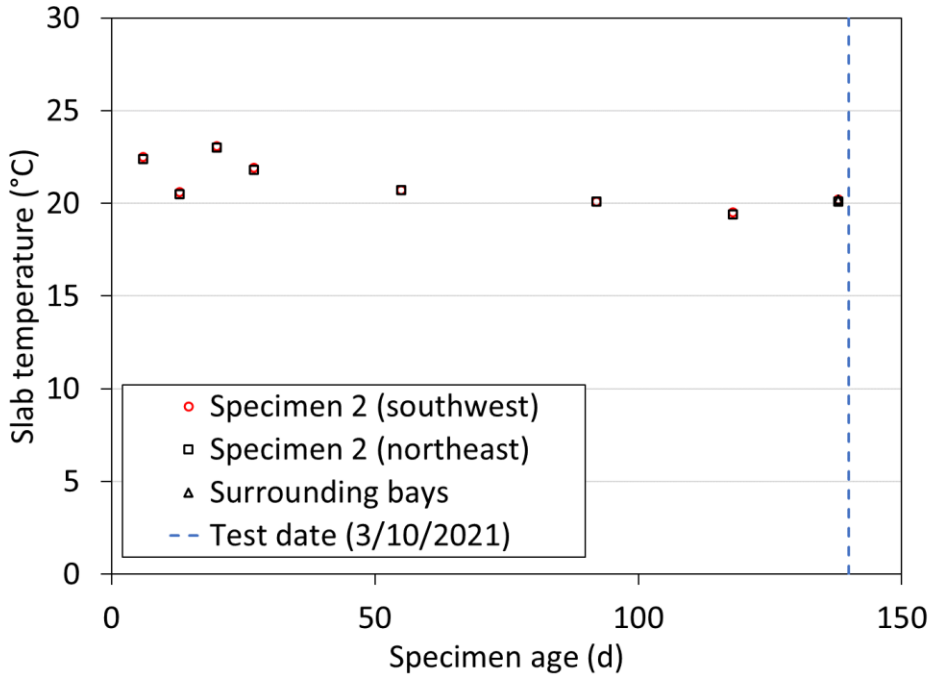

Fig. 12. Temperature in the test specimen and surrounding bays.

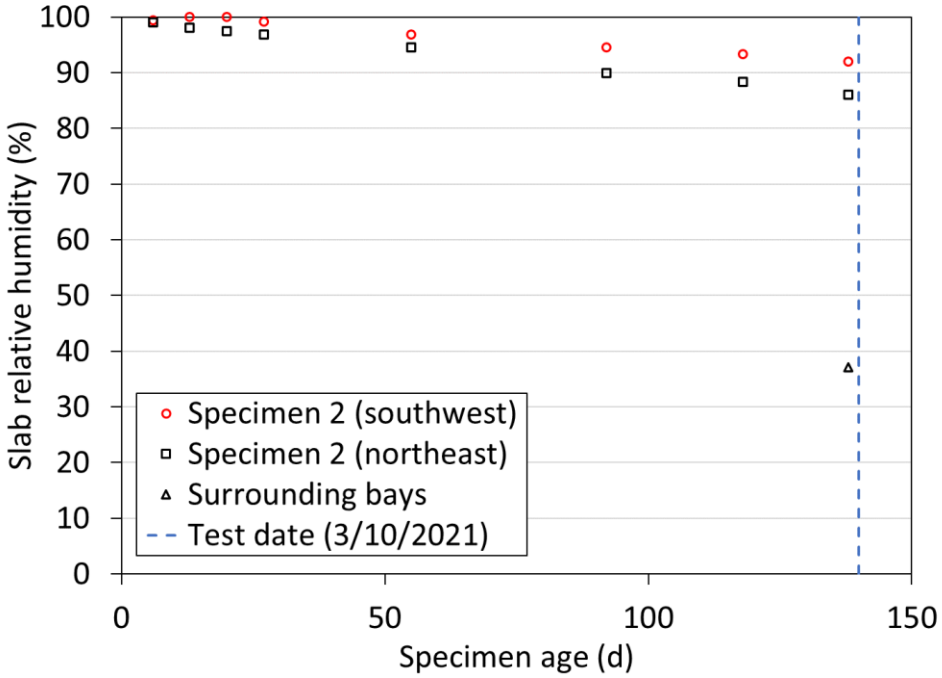

Fig. 13. Relative humidity in the test specimen and surrounding bays.

2.4.4. Hardened Concrete Properties

Table 5 summarizes the measured concrete properties. Where applicable, the relevant ASTM test standard used is provided in the table. The reader is directed to the current edition of these standards for details on those test methods. Details about the tests used to determine the thermal conductivity and specific heat of the concrete are provided in Choe et al. [18]. Except for the tension splitting strength tests, all tests were performed within one week after the large specimen fire test. Except for the measurements made at the time of casting of the concrete, all measurements were made from 102 mm × 204 mm concrete cylinders prepared according to ASTM C192 [28] and cured alongside the concrete slab in the test hall. All measurements were made at ambient laboratory temperatures; nominally 23 °C. No measurements of the concrete properties at elevated temperatures were made.

The slump and plastic unit weight of the concrete are reported in Table 6. No replicate measurements of the fresh concrete were made so standard deviation is not reported. Table 7 summarizes the measured properties (mean and one standard deviation) of the hardened concrete for each individual delivery truck (batch). Each value is from two or more replicates. Average values for the concrete in the test specimen and surrounding bays are provided in Table 8.

Table 5. Matrix of measured concrete properties.

Property	Number of cylinders			
	Casting 10/21/2020	28-day 11/18/2020	Day of Test	Total
Slump (ASTM C143)	✔	-	-	-
Plastic unit weight (ASTM C138) [b]	✔	-	-	-
Compressive strength (ASTM C39)	-	6	6	12
Density (ASTM C642)	-	-	[a]	-
Static modulus (ASTM C469)	-	-	[b]	-
Splitting strength (ASTM C496)	-	-	6	6
Moisture content (ASTM C642)	-	-	6	6
Thermal conductivity	-	-	2	2
Specific heat	-	-	[c]	-
			Total	26

[a] Use moisture content cylinders.

[b] Use tensile strength cylinders.

[c] Use microcores from thermal conductivity cylinders.

Table 6. Fresh concrete properties.

	Truck number	
Property	T1	T2
Water-to-binder (cement + fly ash), -	0.41	0.41
Slump, cm	15.9	17.8
Tare ==> Empty measure, kg	6.41	6.41
Mass ==> Measure + Concrete, kg	34.72	34.66
Unit weight kg/m^3	1995	1991

Table 7. Hardened concrete properties for each truck.

Category	Description	Truck T1	Truck T2
Structural	Compressive strength, MPa	78.4 ±0.5	77.5 ±1.2
	Splitting tensile strength, MPa	6.1 ±0.3	6.1 ±0.1
	Static modulus, GPa	24.6 ±0.7	26.0 ±0.6
Thermal	Bulk density, kg/m^3	1931 ±9.6	1964 ±18.6
	Moisture content, % mass	6.0 ±0.1	5.4 ±0.0
	Thermal conductivity, W/m·K	1.897 ±0.047	2.395 ±0.248
	Specific heat, J/kg·K	822 ±82	773 ±23

Table 8. Average hardened concrete properties.

Category	Description	Specimen 2 (T1+T2)	Surrounding bays*
Structural	Compressive strength, MPa	78.0 ±1.0	63.0 ±1.1
	Splitting tensile strength, MPa	6.1 ±0.2	not available
	Static modulus, GPa	25.3 ±0.9	24.9 ±0.2
Thermal	Bulk density, kg/m^3	1948 ±22	1911 ±10
	Moisture content, % mass	5.7 ±0.3	7.7 ±0.2
	Thermal conductivity, W/m·K	2.146 ±0.306	2.180 ±0.136
	Specific heat, J/kg·K	797 ±65	887 ±47

* Determined in November 2019.

2.5. Instrumentation & Measurement Uncertainty

Measurements were performed to quantify the applied mechanical and fire loading as well as the thermal and structural responses of the test structure during and after fire exposure. Details of the measurement system, data acquisition and recording systems are presented in Choe et al. [18] and briefly summarized herein. Appendix B provides the physical locations and channel names of the sensors.

The mechanical load applied on the floor specimen was controlled and measured using four servo-hydraulic actuators (Model: MTS 201.35TS). The heat release rate of the test fire was quantified using both the fuel consumption and oxygen consumption calorimetry [29]. The gas temperature produced in the fire test bay and temperatures of the floor specimen at various locations (including composite slabs, floor beams, and connections) were measured using K-type thermocouples (with 20-gauge or 22-gauge wires). Gardon gauges were used to measure instantaneous heat fluxes on the exposed surface of the compartment enclosure. Gas velocity through the ventilation opening of the test compartment was measured using bi-directional probes with high-precision capacitance manometers. Resistive displacement transducers were installed outside of the test compartment at a variety of locations to measure the vertical and horizontal displacement of the test structure. Linear strain gauges were mounted on the steel reinforcement in the test floor slab and at the base of the support columns and steel frames in the surrounding bays to measure the thermally induced forces during and after fire exposure.

The strain, voltage and temperature measurements were digitized and recorded using National Instruments (NI) CompactDAQ and PXI systems with signal conditioned I/O Modules. The heat release rate measured by the NFRL's calorimeters were digitized and recorded using a separate data acquisition system described by Bryant and Bundy [29]. An in-house software developed in LabVIEW™ called MIDAS (Modular In-situ Data Acquisition System) was used to allocate channels and control the data acquisition.

High-definition cameras were deployed to record and live-stream a variety of video scenes of the test building and the fire test compartment during the heating and cooling phases of a fire. Thermal imaging of the unexposed (top) surface of the test assembly was performed using a high-speed infrared camera (Model: FLIR SC8303).

The measurement uncertainty is summarized in Table 9. The estimated total expanded uncertainty values are rounded to the nearest integer, except for the construction dimensions and heat release rate of burners which are rounded to the nearest tenth. The users of this report are advised that the experimental results presented in Chapter 3 are either raw data or the statistics of raw data. The authors recommended incorporating the measurement uncertainty reported herein into validation of predictive models or verification of new metrology techniques.

The standard uncertainty in measurements is estimated based on four categories in accordance with Taylor and Kuyatt [30] as follows:

- Type A uncertainty estimated using statistical analysis of the measured data, e.g., in-house calibration or random error caused by the test environment

- Type B uncertainty estimated by other means, such as manufacturer's data sheets (e.g., sensor resolution or factory calibration) or operator's experience (e.g., assumed misalignment or temperature effects)
- Combined standard uncertainty estimated using 'root-sum-of-squares' method to combine all the Type A and Type B uncertainty components
- Total expanded uncertainty computed by multiplying the combined standard uncertainty by a coverage factor (k) of 2 for a 95 % confidence level

The components considered in the component standard uncertainty include resolution, calibration, installation, and random errors. The resolution is the minimum change in the data measurement the instrument can exhibit. Calibration error includes uncertainties from calibration of the sensor. The resolution and calibration uncertainties were derived from instrument specifications (Type B). Uncertainty due to installation method was estimated based on engineering judgement (Type B) considering misalignment, quality of the mounting method of the sensors, and previous data. Random error which resulted from random unpredictable variations in the environment and measurement process was estimated as Type A.

Table 9. Estimated measurement uncertainty. FSO_E = maximum measured values; N = number of samples used for estimating random errors

Measurement / Component	Uncertainty Type	Standard Uncertainty	Combined Standard Uncertainty	Total Expanded Uncertainty (k=2)
Actuator Load (FSO_E = 125 kN)				
Resolution	Type B	± 0.1 %	± 0.6 %	± 1 %
Calibration	Type B	± 0.5 %		
Random (N=6390)	Type A	± 0.4 %		
Vertical Displacement (FSO_E = 580 mm)				
Resolution	Type B	± 0.1 %	± 1.2 %	± 2 %
Calibration	Type B	± 0.2 %		
Random (N=12000)	Type A	± 1.2 %		
Horizontal Displacement (FSO_E = 35 mm)				
Resolution	Type B	± 0.1 %		
Calibration	Type B	± 1.1 %	± 2.9 %	± 6 %
Temperature compensation	Type B	± 2.0 %		
Random (N=12000)	Type A	± 1.8 %		
Strain (FSO_E = 4320 με)				
Resolution	Type B	± 0.1 %	± 0.5 %	± 1 %
Calibration	Type B	± 0.5 %		
Random (N=12000)	Type A	± 0.1 %		
Steel Temperature (FSO_E = 970 ºC)				
Resolution	Type B	± 0.1 %		
Calibration	Type B	± 0.4 %	± 3.2 %	± 6 %
Installation	Type B	± 2.0 %		
Random (N=12000)	Type A	± 2.4 %		
Concrete Temperature (FSO_E = 310 ºC)				

Measurement / Component	Uncertainty Type	Standard Uncertainty	Combined Standard Uncertainty	Total Expanded Uncertainty (*k*=2)
Resolution	Type B	± 0.1 %	± 4.1 %	± 8 %
Calibration	Type B	± 0.4 %		
Random (N=12000)	Type A	± 2.8 %		
Gas Temperature (FSO_E = 1110 ºC)				
Resolution	Type B	± 0.1 %		
Bias	Type B	± 0.4 %	± 4.1 %	± 8 %
Radiative cooling or heating	Type B	± 4.0 %		
Random (N=12000)	Type A	± 0.4 %		
Construction Dimensions (FSO_E = 9.1 m)				
Resolution	Type B	± 0.1 %	± 0.2 %	± 0.5 %
Misalignment	Type B	± 0.2 %		
Random	Type B	± 0.1 %		
Weight (FSO_E = 2.1 kN)				
Resolution	Type B	± 0.1 %	± 1.2 %	± 2 %
Bias	Type B	± 0.1 %		
Random	Type A	± 1.2 %		
Fuel Consumption Calorimetry (FSO_E = 10 MW)	Type B			± 1.4 %
Oxygen Consumption Calorimetry (FSO_E = 10 MW)	Type B			± 8 %

3. Test Results

This chapter describes the second compartment fire experiment (Test #2) conducted on the 9.1 m by 6.1 m composite floor assembly, data (including average values and standard deviation where applicable) and observations from the heating and cooling phase of a test fire. The raw data are presented in Appendix B.

3.1. Test Protocol

The following test protocol was used in this experiment:

1. Increase a total mechanical load to 125 kN at ambient temperature using four servo-hydraulic actuators.
2. Ignite pilot flames of the burners and increase natural gas flow to ignite the burners. The heat release rate of the burners (HRRburner) was initially set to 1000 kW for approximately 2 min to verify the uniformity of natural gas flow to all four burners.
3. Increase the value of HRRburner following the pre-determined HRRburner versus time relationship, which was designed to create the upper layer temperature similar to furnace temperatures prescribed in the ASTM E119 standard [13].
4. Remove the fire and hydraulic loading simultaneously when any of the following criteria was met: (i) detachment of the beam-to-column connection(s), (ii) breach of the fire test compartment (a test floor assembly, enclosing walls, or both), (iii) actuator piston stroke reaching its maximum of 690 mm, (iv) loss of exhaust hood flow, or (v) failure of the data acquisition system network connection for a period exceeding 5 min.

Table 10 provides key events during the fire test experiment, where the reported times are rounded to the nearest minute. As shown, hydraulic loading was continuously applied over a 2 hr cooling period following the burner extinguishment at 131 min.

Table 10. Timeline of Test #2 on March 10th, 2021.

Clock Time	Fire Exposure Time	Description
10:36 AM		Hydraulic loads of actuators began to ramp up
11:25 AM	0 min	The burner ignition was confirmed; See Fig. 14a.
12:45 PM	100 min	A breach became visible along the south wall above the test floor level allowing flame extension; See red circle in Fig. 14b.
1:36 PM	131 min	The burners were switched off
3:38 PM		Hydraulic pressure was released

(a)

(b)

Fig. 14. Snapshots from the test video showing (a) inside the test compartment at ignition of the burners and (b) top of the test floor specimen at 120 min after the burner ignition.

3.2. Fire Test Condition

This section describes the mechanical loading and fire conditions created during Test #2.

3.2.1. Mechanical Loading

A total of four hydraulic actuators (name: NE, NW, SE, and SW) were used to apply mechanical loads distributed at 24 points across the test bay. Locations of the hydraulic actuators and the raw data including loads and displacements applied using individual actuators are provided in Appendix A.1. The average value of applied loads and stroke displacements by a single actuator are shown in Fig. 15a. Four actuators increased a floor load simultaneously to a target value of 31 kN each at ambient temperature. This load level was then maintained throughout the heating and cooling phase of the test fire. The maximum variation in the load values from four actuators was 3.5 kN at ambient temperature. During the heating and cooling phase of the test fire, the load values varied by 0.3 kN. The total load applied using four actuators was maintained at (123 ± 11) kN.

As shown in Fig. 15b, the north half of the test floor slab loaded by the NE and NW actuators exhibited smaller displacements throughout the test period due to slab continuity to the north surrounding bay. The result indicated that the boundary (support) conditions of the test floor assembly was maintained symmetrical about its north-south (transverse) centerline. The maximum variation in actuator displacement values was estimated 5 mm between the NE and NW actuators and 2 mm between the SE and SW actuators.

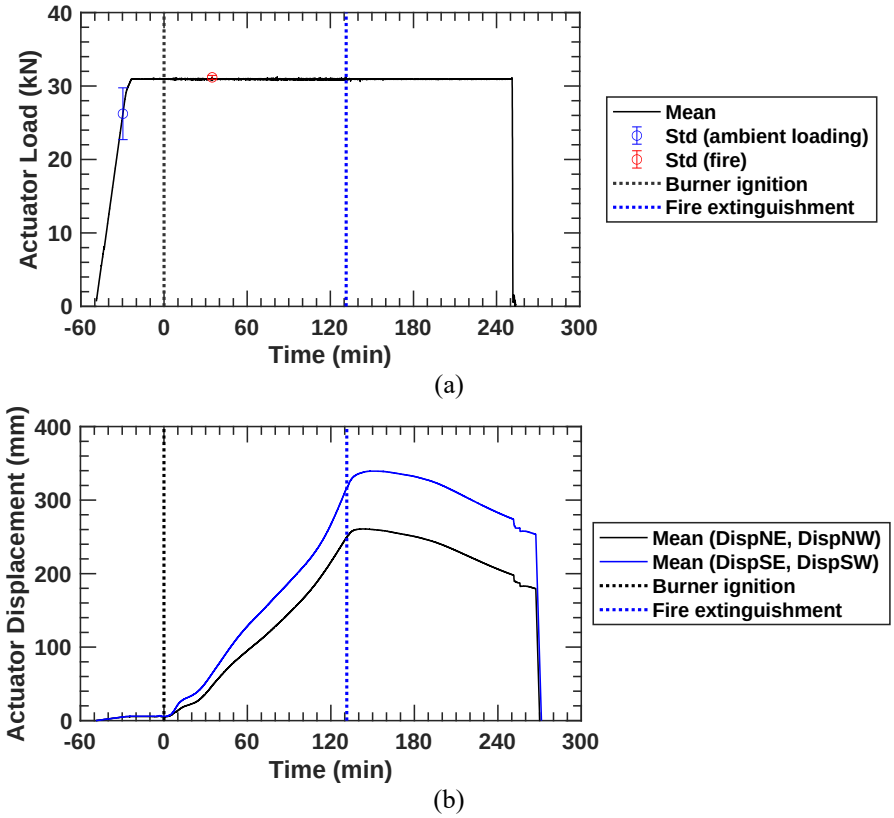

Fig. 15. (a) Average load applied by a single actuator and (b) stroke displacement of the north actuators (DispNE and DispNW) and the south actuators (DispSE and DispSW).

3.2.2. Test Fire

The test fire environment was created using four natural gas burners (1 m × 1.5 m each) distributed on the floor of the test compartment. The time variation of heat release rates and compartment temperatures recorded during the heating and cooling phases of the test fire is presented in the following subsections.

3.2.2.1. Heat Release Rate

The heat release from the test fire was measured using two methods: the natural gas fuel consumption based on mass flow to the burners (channel: HRRburner) and the oxygen calorimetry at the 20 MW exhaust hood (channel: HRR) as described in Bryant and Bundy [29]. The HRRburner and HRR data are provided in Fig. 16. The natural gas fire was controlled using the pre-programed fuel flow function to create the HRRburner versus time relationship. As shown in Fig. 16, the HRR values were approximately 630 kW greater than the HRRburner values. The fluctuation in HRR values was approximately ± 250 kW on average.

Table 11 shows a summary of the measured peak heat release rate, total heat energy, and fuel load density that was estimated as the total heat energy divided by the floor area of the test compartment. The difference of the peak heat release rate between the natural gas fuel delivery system and oxygen calorimetry was approximately 10 % at 12 MW.

Some images showing inside the test compartment and the test building captured during fire loading are shown in Fig. 17 and Fig. 18.

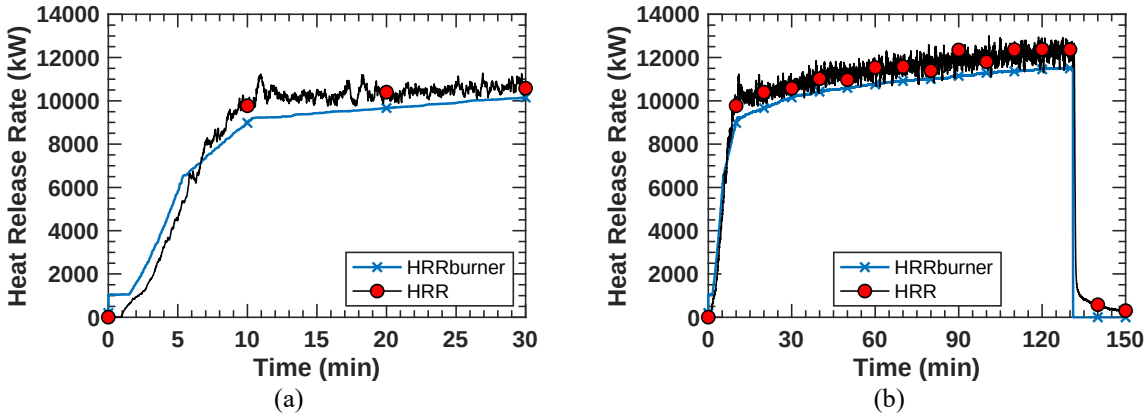

Fig. 16. Heat release data (HRRburner and HRR) measured (a) first 30 min and (b) during entire heating.

Table 11. Measured total heat release and fuel load density.

Method	Peak heat release rate (kW)	Total heat energy (MJ)	Fuel load density (MJ/m^2)
Oxygen calorimetry	12776	86908	1332
Fuel consumption	11508	81287	1252

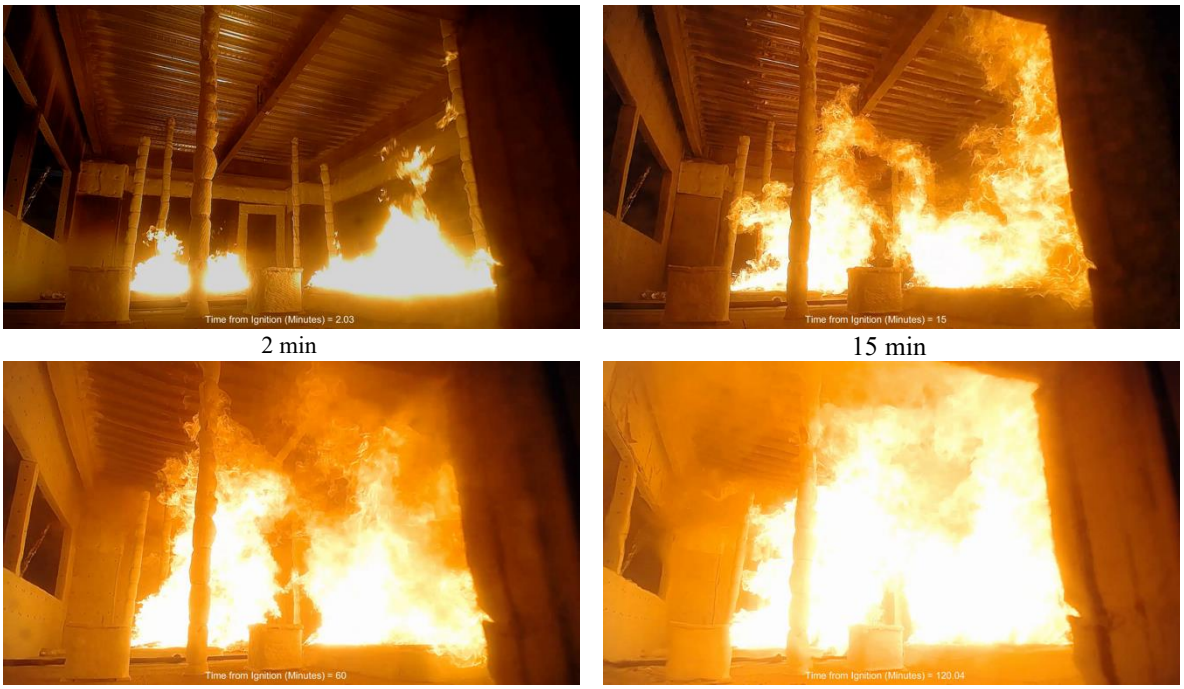

2 min 15 min

60 min 120 min

Fig. 17. Snapshots of the video showing inside the test compartment with the times recorded following the burner ignition.

Fig. 18. Front view of the main vent opening of the fire test compartment during Test #2.

3.2.2.2. Gas Temperature

Gas temperatures inside the test compartment were measured 30 cm below the floor specimen soffit (i.e., 346 cm above the compartment floor) using twelve thermocouples as well as two thermocouple trees mounted on the compartment floor. Locations of individual thermocouple probes and raw data are reported in Appendix A.2.

The natural gas fire created practically uniform upper layer gas temperatures to heat the floor specimen soffit, as shown in Fig. 19a. The standard deviation in the temperature measurements across the test bay was less than 50 °C during heating. The average upper layer gas temperature (AvgULG) measured in this test was about 5 % higher than that measured in Test #1. This difference was caused by the house natural gas supply pressure during fire loading. The incoming natural gas pressure was measured 160 kPa (23 psig) in Test #1 but 170 kPa (25 psig) in Test #2. Although the control valve position settings of the natural gas fuel delivery system were almost identical between the two tests (within 1% difference), the elevated supply gas pressure increased the actual fuel mass flow by 6 % and subsequently increased the HRRburner value by 0.5 MW.

A comparison of the gas temperature measured at three different heights within the test compartment, i.e., 100 cm, 200 cm, and 300 cm above the ground floor, is shown in Fig. 19b. The thermal gradient through the height of the test compartment was greater up to the first 15 min into heating. However, the temperature difference became much smaller at 1 hr after the burner ignition, approximately 30 °C on average.

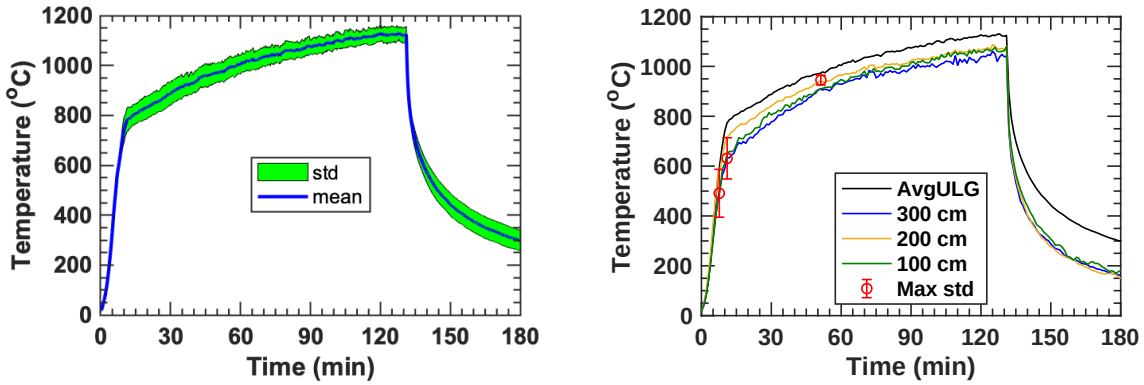

(a) (b)

Fig. 19. (a) Averaged values and standard deviation of the upper layer gas temperatures measured using TCC channels and (b) gas temperatures measured at 100 cm, 200 cm, 300 cm from the floor of the test compartment along with the average upper layer gas temperature (AvgULG).

Air flow through the windows of the test compartment was measured using a set of bi-directional probes with pressure transducers during fire loading. Refer to Appendix A.10 for locations of the sensors as well as velocity and gas-phase temperatures measured across the south and north windows of the test compartment.

3.3. Thermal Response

This section describes temperatures of the test floor assembly measured at a variety of locations during the heating and cooling phase of the test fire. Most of the data presented herein are the average values of temperatures measured by multiple thermocouples. All thermocouple locations and raw temperature data are reported in Appendix A.3 through A.7.

3.3.1. Concrete Slab and Steel Reinforcing Bars

The averaged values of concrete temperatures measured within the floor slab with profiled steel decking are illustrated in Fig. 20, where error bars indicate the standard deviation in temperature measurements across the test bay at the same concrete depth. Refer to Appendix A.3 and A.4 for locations of individual thermocouples and the list of temperature channels used to compute the average values of measured concrete or steel bar temperatures reported in this section.

As shown in Fig. 20, the change in concrete temperatures varied with the measurement locations (1 through 7) within the test floor slab. The concrete temperature near the exposed deck reached 800 °C on average during the fire exposure. Temperatures closer to top of the slab increased more slowly but increased continuously during the early cooling phase. Temperatures measured at locations 1, 2 and 5 were significantly influenced by evaporation of the moisture driven out toward the top of the slab during heating, as indicated by a 100 °C plateau. The magnitude of error bars indicates that the larger variation in temperatures was observed at locations 4, 5, and 5*. These temperature measurements appeared to be affected by several factors, such as the separation of concrete from the steel decking, concrete cracks, or combined effects. Temperatures measured at the mid-depth of the topping concrete in the test bay, where the steel reinforcement was placed, varied due to the concrete mass below. At 107 min, for instance, the temperature measured at location 1 and 6 was 140 °C and 420 °C, respectively.

A total of eight thermocouple probes were mounted 3 mm below the top surface of the concrete slab. The average values of temperatures measured at the top of the deep and shallow concrete slab sections are plotted in Fig. 21a. As shown, the temperature measurement at the top of the deep concrete section appeared to be affected by evaporation of the moisture in the concrete over a longer period. The top surface temperature of the shallow concrete section exceeded 160 °C at 100 min, i.e., 140 °C above the ambient temperature measured prior to the ignition of a test fire. For the deep section, the peak temperature reached 200 °C on average at about 110 min after the burners were switched off.

The average temperatures of No.3 deformed bars placed within the deep and shallow sections of the test floor slab are shown in Fig. 21b. The peak temperature of the bars with a large concrete cover (from the specimen soffit) reached about 350 °C on average about 5 min after the test fire was extinguished, whereas the bars embedded in the shallow section were heated to 540 °C at 125 min following the burner ignition.

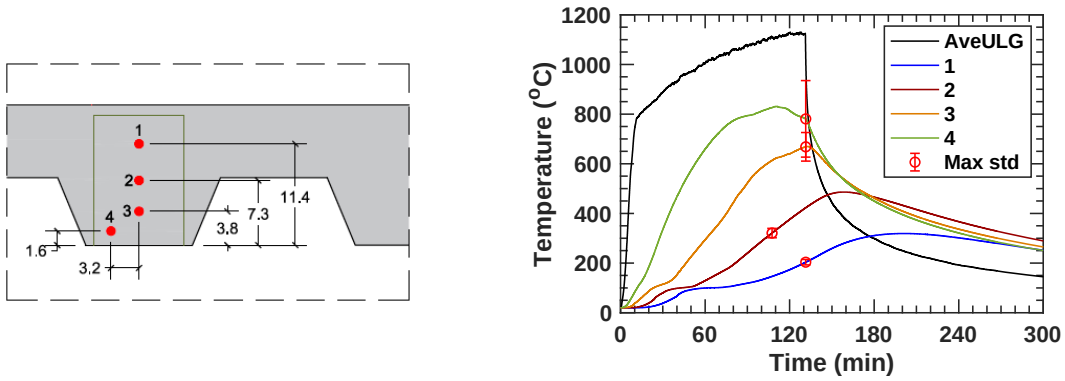

(a)

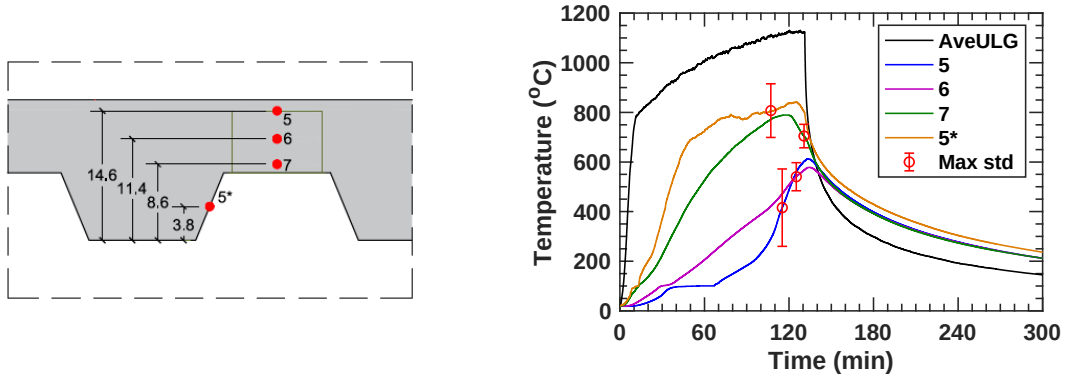

(b)

Fig. 20. Average temperatures of (a) 15.9 cm deep sections and (b) 8.3 cm deep sections of the test floor slab. Error bars indicate the maximum standard deviation of temperatures recorded from multiple thermocouples installed at the same distance from the steel deck. Dimensions are in cm.

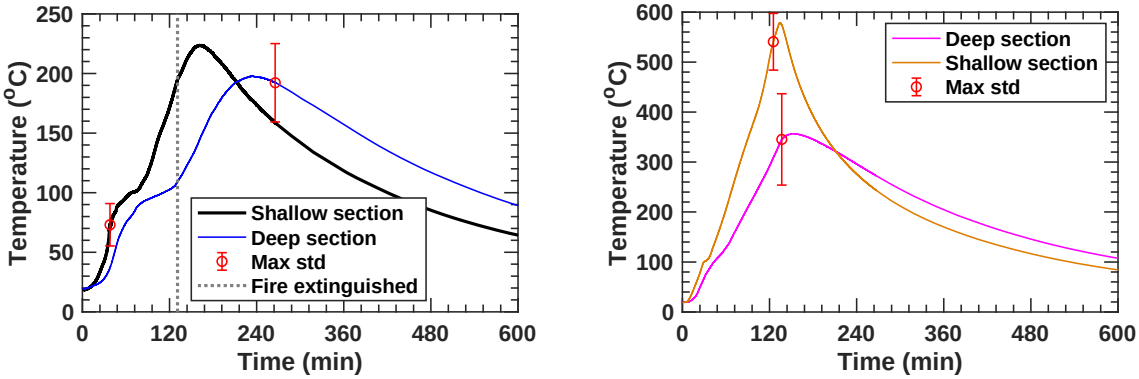

(a) (b)

Fig. 21. (a) Average temperature measured 3 mm below the top (unexposed) surface of composite slab and (b) average temperatures of No.3 deformed bars within the test floor slab.

3.3.2. Composite Beam and Girder

Temperatures of the 9.1 m span composite beams and 6.1 m span composite girders within the fire test bay were measured across the midspan cross section, as shown in Fig. 22. Temperatures of all five SFRM-protected steel beam shapes and the topping slab are reported in Appendix A.5 and A.6.

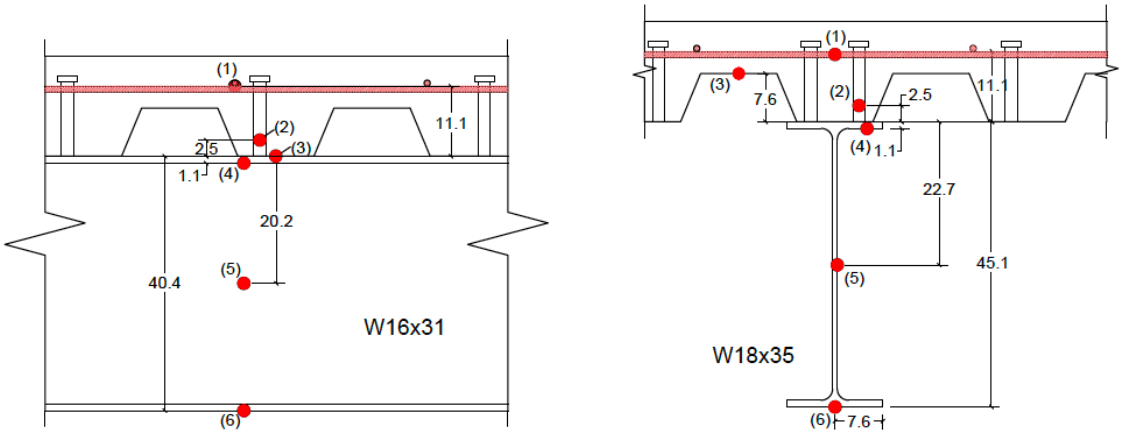

Composite beam (W16x31) Composite girder (W18x35)

Fig. 22. Locations of thermocouple probes within the 9.1 m composite beam and the 6.1 m composite girder at midspan. Dimensions are in cm.

The typical temperature change across the composite beam sections is presented in Fig. 23. The 9.1 m composite beam temperatures (Fig. 23a) are the average values of temperature readings of the north, south, and secondary beams at midspan. Similarly, the composite girder temperatures in Fig. 23b are the average temperature values of the east and west girders at midspan. As shown, during the fire exposure, temperatures of the SFRM-applied steel shapes reached a peak value of 850 °C at the bottom flanges and 500 °C at the top flanges on average. Temperatures of the embedded No. 3 reinforcing bars over the beams or girders increased to a peak value of 200 °C after the test fire was extinguished. The greater temperature variation (as large as 20 %) was observed at the top flange or within the concrete slab.

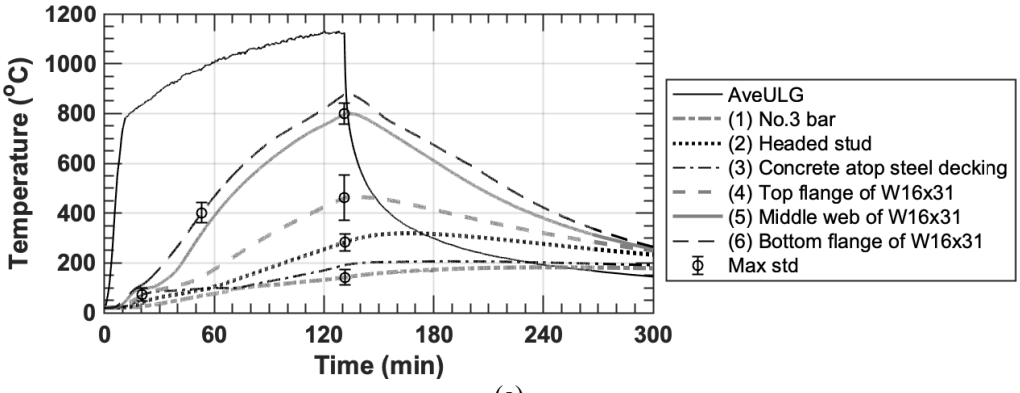

(a)

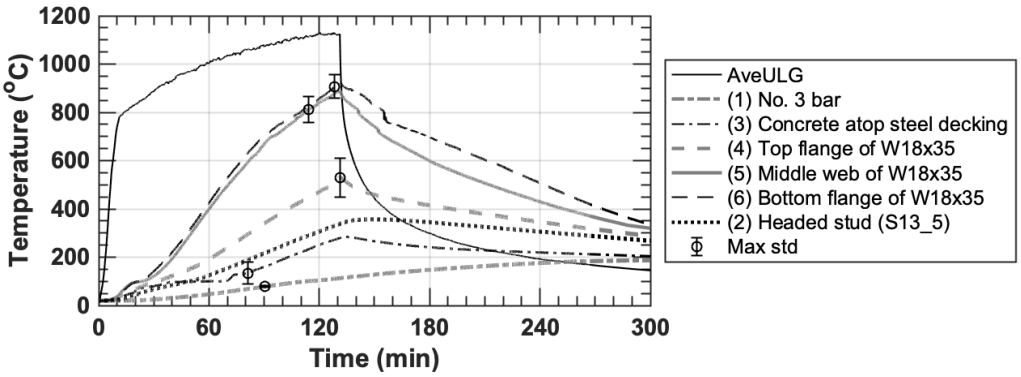

(b)

Fig. 23. Average temperatures of (a) 9.1 m composite beam and (b) 6.1 m composite girder at midspan. The error bars indicate the maximum standard deviation of temperature readings at different sections.

3.3.3. Beam-End Connection

All beam-end connections within the fire test bay were protected with the same SFRM used for the connected beams and girders. Refer to Table 3 for the thickness of applied SFRM. Typical locations of the thermocouples mounted on the shear-tab connections of the floor beams are shown in Fig. 24. The average temperatures of the beam-end or girder-end connection regions are provided in Fig. 25 and Fig. 26. Temperatures of all ten connections exposed to fire are reported in Appendix A.7.

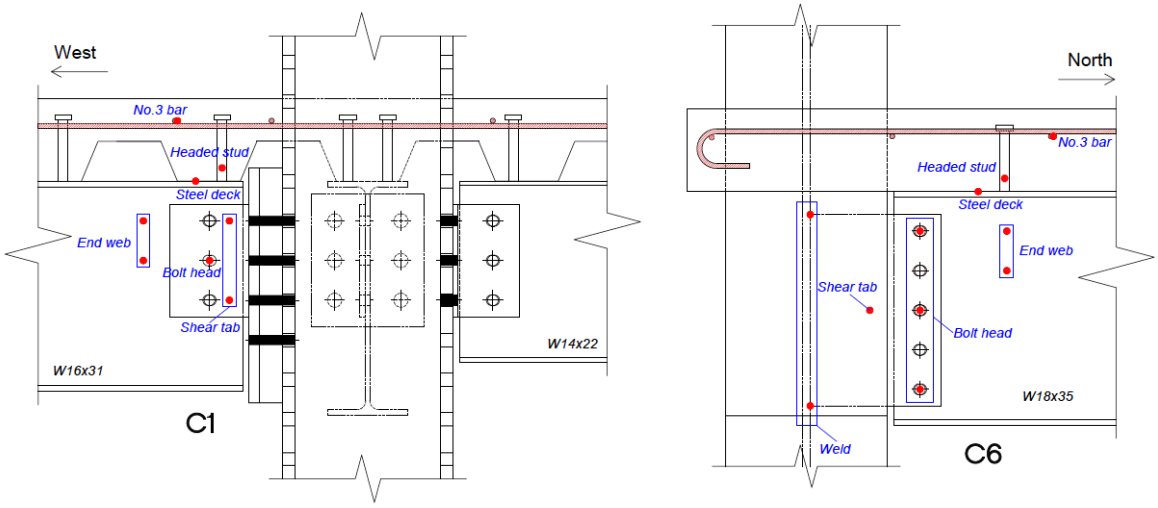

Fig. 24. Typical locations of temperature measurements in the beam-end (left) and girder-end (right) connection regions.

As shown in Fig. 25, the beam-to-girder connection region was heated more rapidly due to its proximity to the burners and a thinner layer of SFRM. The shear-tab connection temperature exceeded 800 °C on average during the fire exposure. Temperatures of the same connection at the north and south beam ends remained below 600 °C. The No.3 reinforcing bar over the connection remained below 200 °C for the north and secondary beams. However, the No. 3 bar temperature at the south beam ends sharply increased after 120 min, indicating concrete cracks.

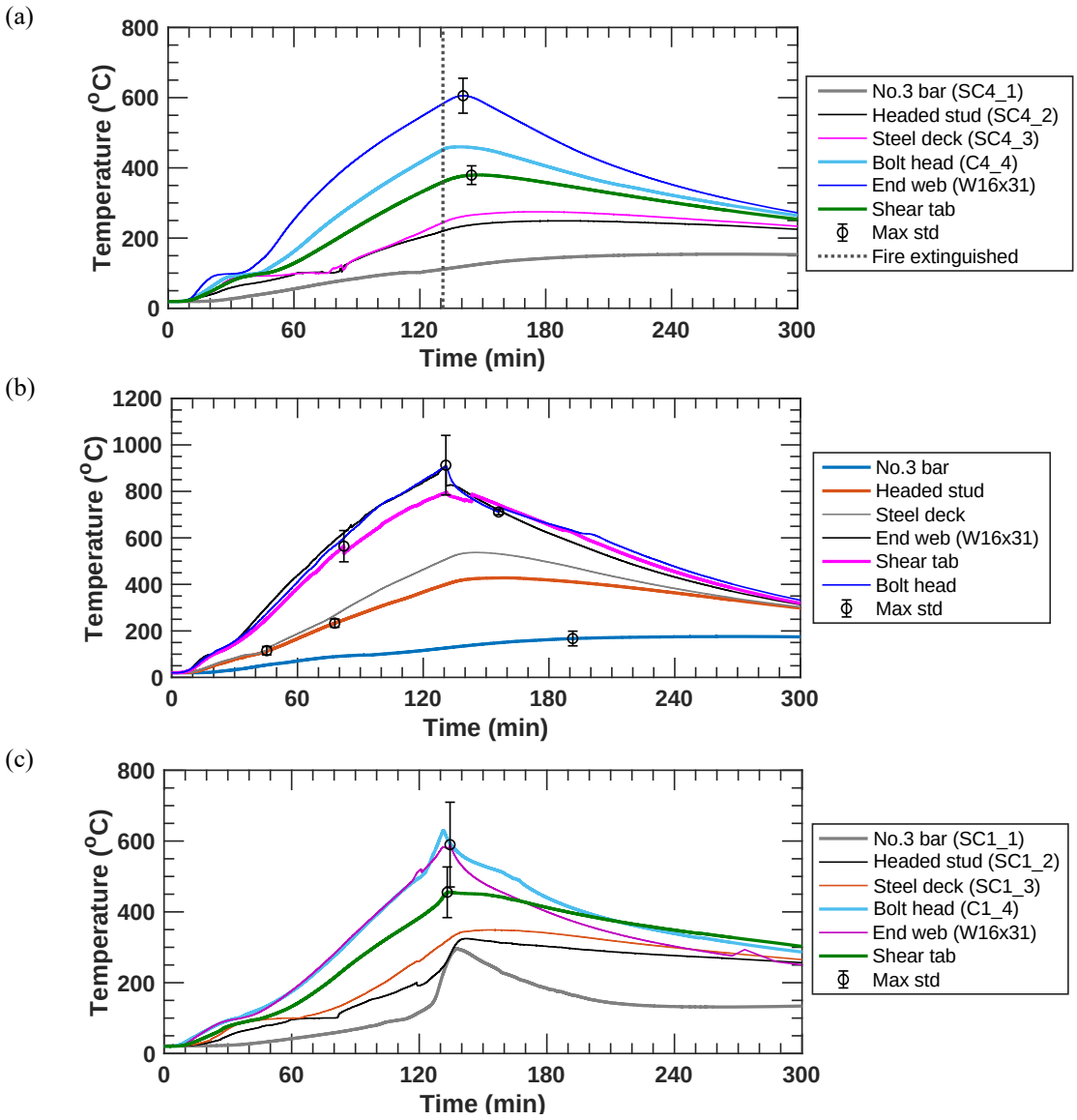

Fig. 25. Average temperatures of the beam-end connections of (a) north edge beam, (b) secondary beam, and (c) south edge beam with W16x31 shapes. Error bars indicate a maximum value of standard deviation of temperatures measured at multiple locations.

he girder end-connection regions indicated a similar change in temperatures (Fig. 26). The beam end web and bolt head reached over 600 °C on average. However, temperatures of the extended shear tabs and welded joints were approximately 200 °C and 400 °C lower, respectively, because thermocouples in those regions were shaded by the column flanges. The No.3 bar temperature was considerably low with a peak value of 200 °C during cooling.

he temperature variation in the beam or girder end webs as well as bolt heads was as large as 25 %. This might be caused by local buckling of the end web leading to physical damages (fissures, debonding, or both) to applied SFRM where thermocouples were installed.

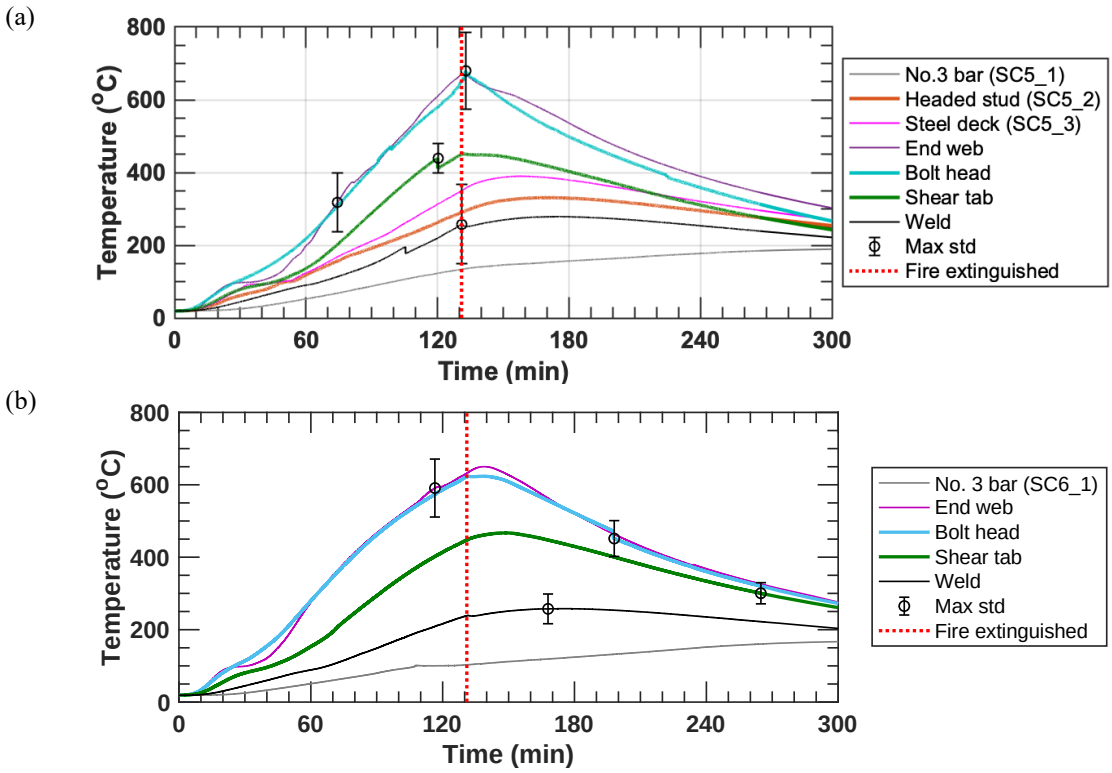

Fig. 26. Average temperature of (a) east girder end connection and (b) west girder end connection attached to W18x35 shapes. Error bars indicate a maximum value of standard deviation in temperatures measured at multiple locations.

3.4. Structural Response

This section presents the vertical and horizontal displacements of the hydraulically loaded composite floor assembly during the heating and cooling phases of a test fire. The displacement data not reported in this section and strain measurements of the support columns and surrounding beams of the two-story test building are included in Appendix A.8 and A.9, respectively.

3.4.1. Vertical Displacement

A total of fourteen displacement transducers (named VD1 through VD14) were deployed to measure the vertical deflection of the test-bay and surrounding floors as shown in Fig. 27. Some vertical displacements are plotted with fire exposure time and the average bottom flange temperatures of the floor beams, as illustrated in Fig. 28. Other displacements not presented in this figure are reported in Appendix A.8. The positive values of displacements indicate the downward vertical displacements as the test floor assembly sagged under fire exposure. As mentioned earlier, the actuator loading was not removed until the 2-hr cooling phase was complete (i.e., 252 min in test time), whereas the test fire was extinguished at 131 min.

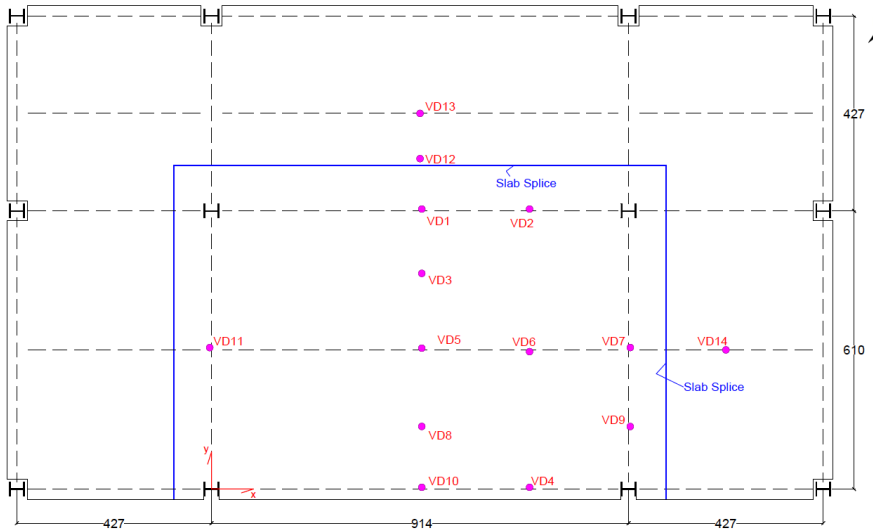

Name/ID	X East+	Y North+
VD1	461	613
VD2	697	309
VD3	461	472
VD4	697	4
VD5	461	309
VD6	697	301
VD7	918	310
VD8	461	137
VD9	918	137
VD10	461	4
VD11	4	310
VD12	461	724
VD13	461	823
VD14	1128	305

Fig. 27. Location of the vertical displacement (VD) measurements. Dimensions and coordinates are in cm.

As shown in Fig. 28, the vertical displacement of the secondary beam at midspan (VD5) increased to 455 mm (equivalent to the ratio L/20 where L = 9.1 m) at 131 min, finally reaching its peak value of 475 mm at 145 min (i.e., about 14 min into cooling). The maximum displacements of the north beam (VD1), the east girder (VD7), and the west girder (VD11) were 200 mm, 115 mm, and 125 mm, respectively. The vertical displacements of the south edge beam at midspan (VD10) became invalid after 130 min because Kaowool strips placed along the south wall were flipped over a measurement string of this displacement sensor as the south wall significantly bent toward the south (Refer to Fig. 14b).

The mid-panel vertical displacement (VD5) increased at an approximate rate of 0.4 mm/°C until the bottom flange temperature of the secondary beam reached 700 °C. The increase in the VD5 value became approximately 0.7 mm/°C afterward. The vertical displacement of the south (exterior) edge beam (VD10) increased more rapidly than other edge beams (VD1,

VD7 and VD11) because of their connectivity to the surrounding bays. A snapshot of the test video recording top of the test floor is shown in Fig. 29

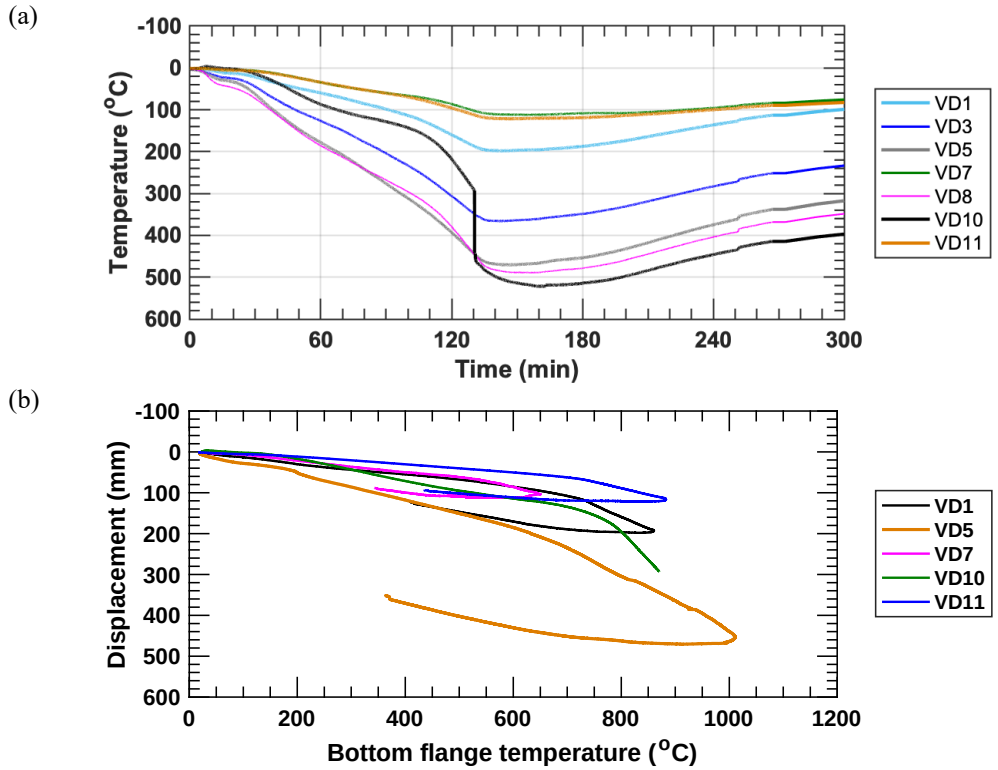

Fig. 28. Measured vertical displacements as a function of (a) fire exposure time and (b) bottom flange temperatures of the floor beams.

Fig. 29. Video image showing top of the test floor at 120 min after fire ignition.

The temporal change in the vertical displacement measured along the centerlines of the test bay is illustrated in Fig. 30. The south half of the floor specimen deflected more than its north half since the No. 3 deformed bars placed perpendicular to the north edge beam provided some degree of rotational restraints, maintaining a good continuity with the steel reinforcement placed in the north surrounding bay which remained cool during fire loading.

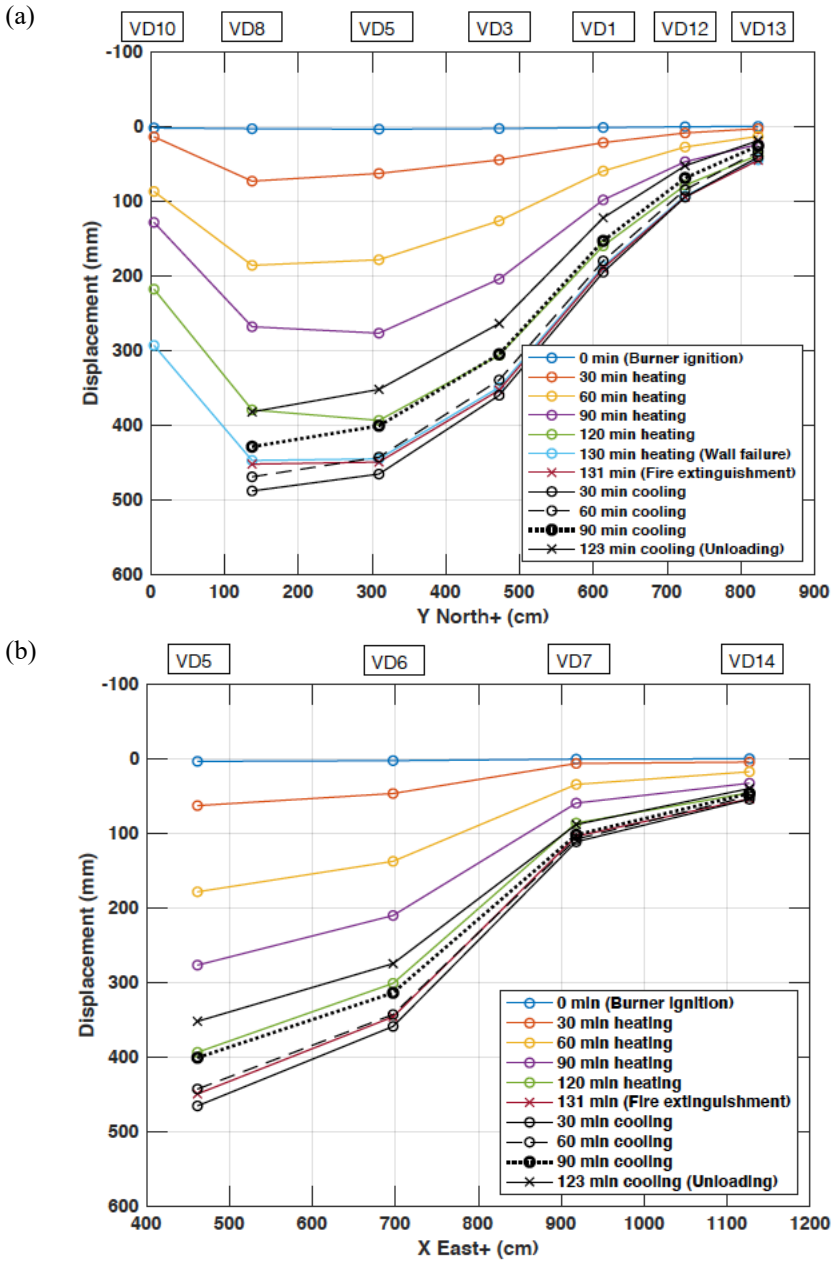

Fig. 30. Vertical displacement profile of the test floor assembly at (a) the north-south centerline and (b) the east-west centerline. The upper horizontal axes indicate the corresponding position of each vertical displacement sensors.

3.4.2. Horizontal Displacement

A total of eighteen string potentiometers (HD1 through HD18) were deployed to measure the horizontal displacement of the test floor assembly and at the perimeter of the two-story prototype building; See Fig. 31. The HD4, HD6, HD18 sensors were used to measure thermal expansion of the north, east, and west edges of the fire test bay, respectively. The lateral displacements of the first-story columns (HD1 through HD3, HD5, HD8 through HD10, and HD16) as well as HD4 and HD6 were measured at 15 cm above the top surface of the test floor slab.

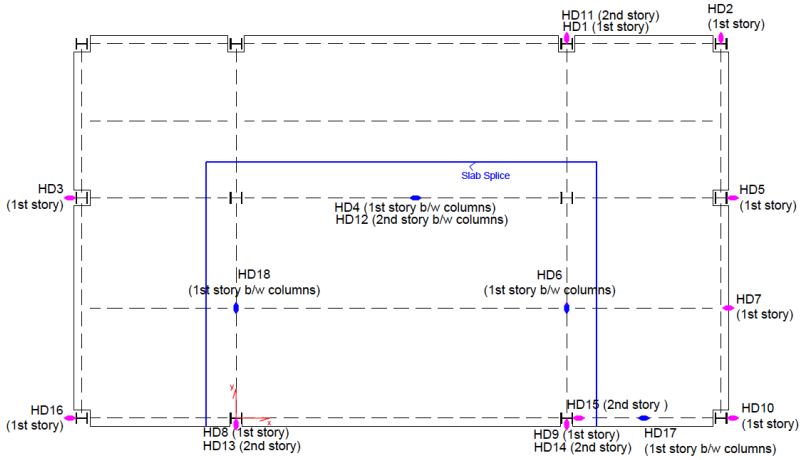

Name/ID	X East+	Y North+	Z Up+	Direction (+ value)
HD1	914	1037	412	North
HD2	1341	1037	412	North
HD3	-443	610	412	West
HD4	16	610	412	Expansion
HD5	1357	610	412	East
HD6	914	609	412	Expansion
HD7	1382	305	427	East
HD8	0	1	412	South
HD9	914	1	412	South
HD10	1357	0	412	East
HD11	914	1037	734	North
HD12	16	610	734	Expansion
HD13	0	1	729	South
HD14	914	1	729	South
HD15	931	0	734	East
HD16	-443	0	412	West
HD17	1325	0	412	East
HD18	0	594	412	Expansion

Fig. 31. Location of horizontal displacement (HD) measurements. The Z datum is defined at the laboratory strong floor. Coordinates are in cm.

Some horizontal (lateral) displacements of the exterior columns at the test floor level are illustrated in Fig. 32. Other displacements not presented in this figure are reported in Appendix A.8. As shown, approx. 5 min into fire loading, the displacements began to increase in the east or west direction due to thermal expansion of the test floor assembly. Simultaneously, the lateral displacement of the north column (HD11) at the second-story level increased toward south since this column was pulled together with the south columns deflecting toward the south during heating. The peak values of each displacement sensor occurred between 80 min and 120 min after the burner ignition. For instance, from 80 min to 95 min into heating, thermal expansion of the north edge beam (HD3) and the south edge beam (HD16) came to a halt, which suggests that local buckling could be initiated near the ends of these beams.

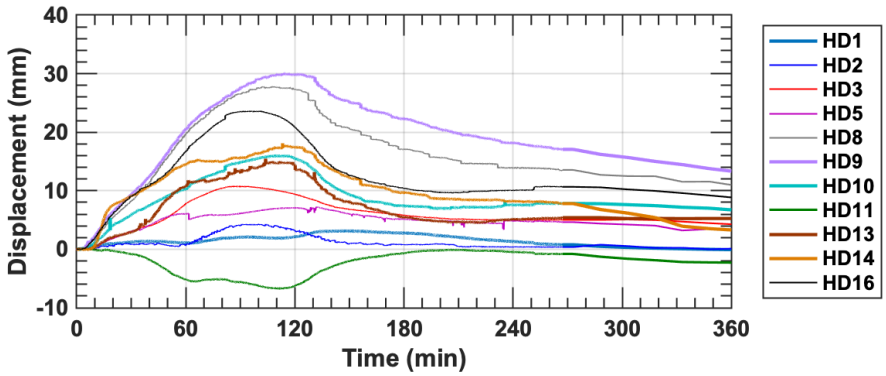

Fig. 32. Measured lateral displacements of the exterior columns.

The horizontal displacements of the floor specimen are plotted as a function of the bottom flange temperatures of the fire-exposed steel beams or girders in the test bay; See Fig. 33. HD4 is plotted with the average bottom flange temperature of the north primary beam; HD7 is plotted with the average bottom flange temperature of the secondary beam; HD1, HD6, and HD9 are plotted with the average bottom flange temperature of the east girder; and HD8 is plotted with the average bottom flange temperature of the west girder.

Thermal elongation along the north edge of the test assembly (HD4) was approximately equal to two times the average displacement of the east and west exterior columns (HD3 and HD5), as shown in Fig. 33a. The change in the displacement values became less sensitive to the temperature beyond 600 °C. Thermal elongation along the longitudinal centerline (HD7) continued until the bottom flange temperature of the secondary beam reached to 870 °C, followed by a descending trend afterward. Thermal elongation along the south edge of the test assembly (HD10) continued until the bottom flange temperature of the south edge beam reached to 720 °C, followed by a descending trend afterward.

With the presence of the north surrounding bay, the east and west edges of the test assembly thermally elongated mostly toward the south. As shown in Fig. 33b, the average thermal elongation of the east and west edges (HD6 and HD18, respectively) were very similar to the average lateral displacement of the southeast and southwest column of the test bay (HD9 and HD8, respectively). Beyond 800 °C, those displacements stopped increasing and began to slowly decrease until the test fire was removed.

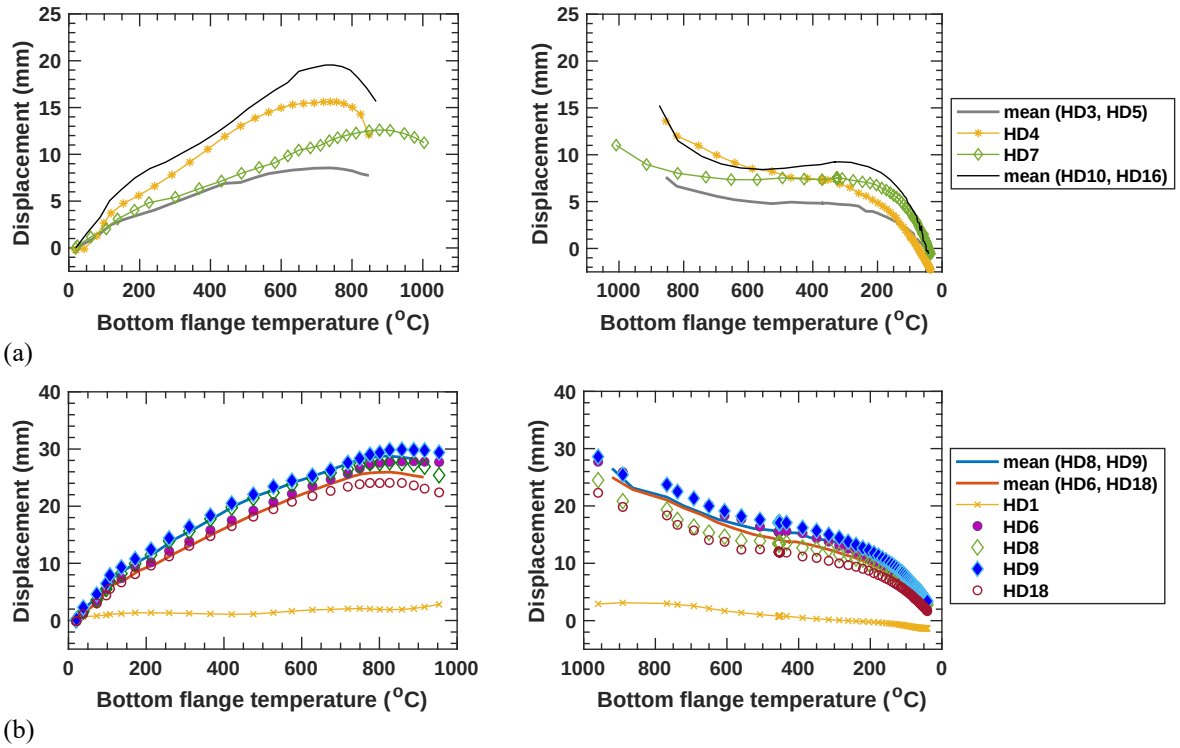

Fig. 33. Measured horizontal displacements as a function of bottom flange temperatures; (a) thermal elongation and contraction in the east-west direction and (b) thermal elongation and contraction in the north-south direction.

3.5. Post-Fire Residual Capacity

After cooldown, the test floor assembly was loaded again using the same hydraulic actuators used in the fire testing to examine its post-fire flexural behavior at ambient temperature. Locations of the loading points on the test floor remained unchanged (Refer to Fig. 4b). For this test, the mechanical loading was applied at an approximate rate of 9 kN/min until the hydraulic actuator system maxed out its load limit (836 kN). The bending stiffness of the test floor before and after the fire test is compared in Fig. 34a. As shown, the fire-damaged test floor retained approximately 42 % of its normal bending stiffness prior to fire exposure.

The total actuator load versus vertical displacement relationship is plotted in Fig. 34b. At a maximum load of 836 kN, the mid-span vertical displacement of the secondary beam (VD5) was about 85 mm, and the vertical displacement of the south middle slab (VD8) was about 91 mm, relative to the permanent displacement measured after cooldown from fire loading. The maximum gravity load was approximately 17.8 kPa (370 psf), which was estimated including self-weight of the test floor assembly prior to fire exposure and that of loading frames.

It is noteworthy that the test floor assembly still retained very large flexural strength (after cooldown) at least two times greater than the ASCE 7 load demand (9 kPa) for normal conditions determined from the load combination of 1.2 times dead load plus 1.6 times live load. A collapse mechanism was not developed even though the total floor load reached almost 90 % of the ambient-temperature moment capacity (21 kPa) of the as-designed secondary composite beam calculated in accordance with the AISC 360 specification [15] but with measured mechanical properties of steel and concrete at ambient temperature (Refer to Table 2 and Table 8, respectively).

Several factors might have influenced this high post-fire capacity of the test floor, including but not limited to (1) the rotational restraint provided by the steel reinforcement in the hogging moment region of the floor slab, (2) the negligible damage in headed stud anchors which developed the design composite action between the steel beams and concrete slabs under flexural loading, and (3) the concrete surrounding the headed studs appeared to be less affected by thermal degradation as temperatures were measured lower than 200 °C in those locations.

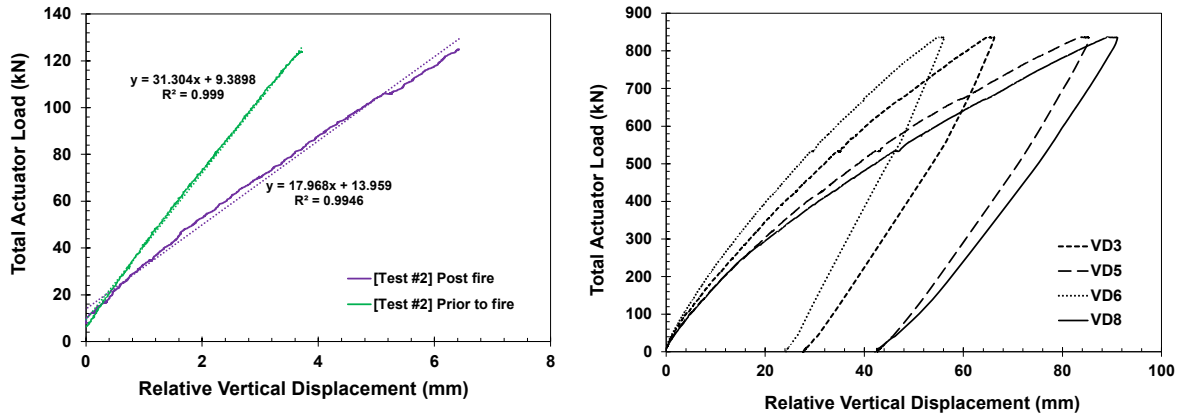

(a) (b)

Fig. 34. (a) Initial bending stiffness and (b) load-displacement relationship during the post-fire loading test.

3.6. Post-Test Inspection

Several visual inspections were performed to examine structural damages of the fire-exposed floor specimen after cool-down. This section presents the final crack pattern of the concrete floor slab as well as local ruptures and deflections of the exposed steel decking, support beams and connections.

3.6.1. Concrete Slab

Fig. 35 shows a concrete crack pattern on top of the floor specimen. The concrete cracks were less than 5 mm wide and randomly distributed across the test bay. The south half of the floor specimen exhibited more transverse cracks that resulted from tensile forces induced in the longitudinal direction (location 1). Longitudinal cracks appeared around the north edge beam as well as around the secondary beam indicating flexural and tensile forces induced in the transverse direction, respectively. Wider cracks were visible along the centerlines of the east and west girders. These cracks were larger toward the south columns but became smaller around the north columns (locations 2 through 5). There were several spots indicating localized aggregate spalling across the test floor slab, e.g., the center of the north edge beam (location 6) and the slab penetration holes (location 7) used for loading tubes.

Some short cracks within the test-bay column grid appeared to be full-depth cracks with visible soot marks but fully closed during cooldown. Overall, the No.3 bars effectively controlled the development of large crack openings in the hogging moment region as well as within the mid-panel zone. Only one longitudinal bar next to the southwest column was found to be ruptured.

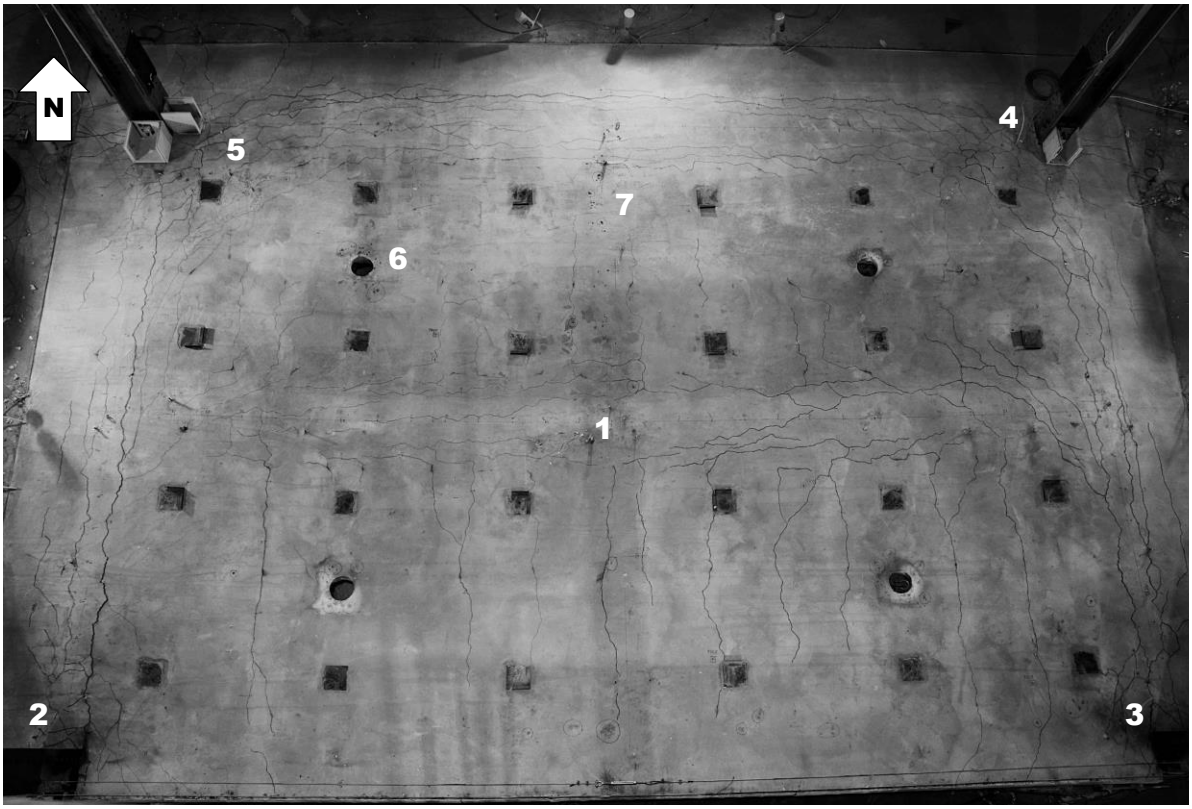

Top View

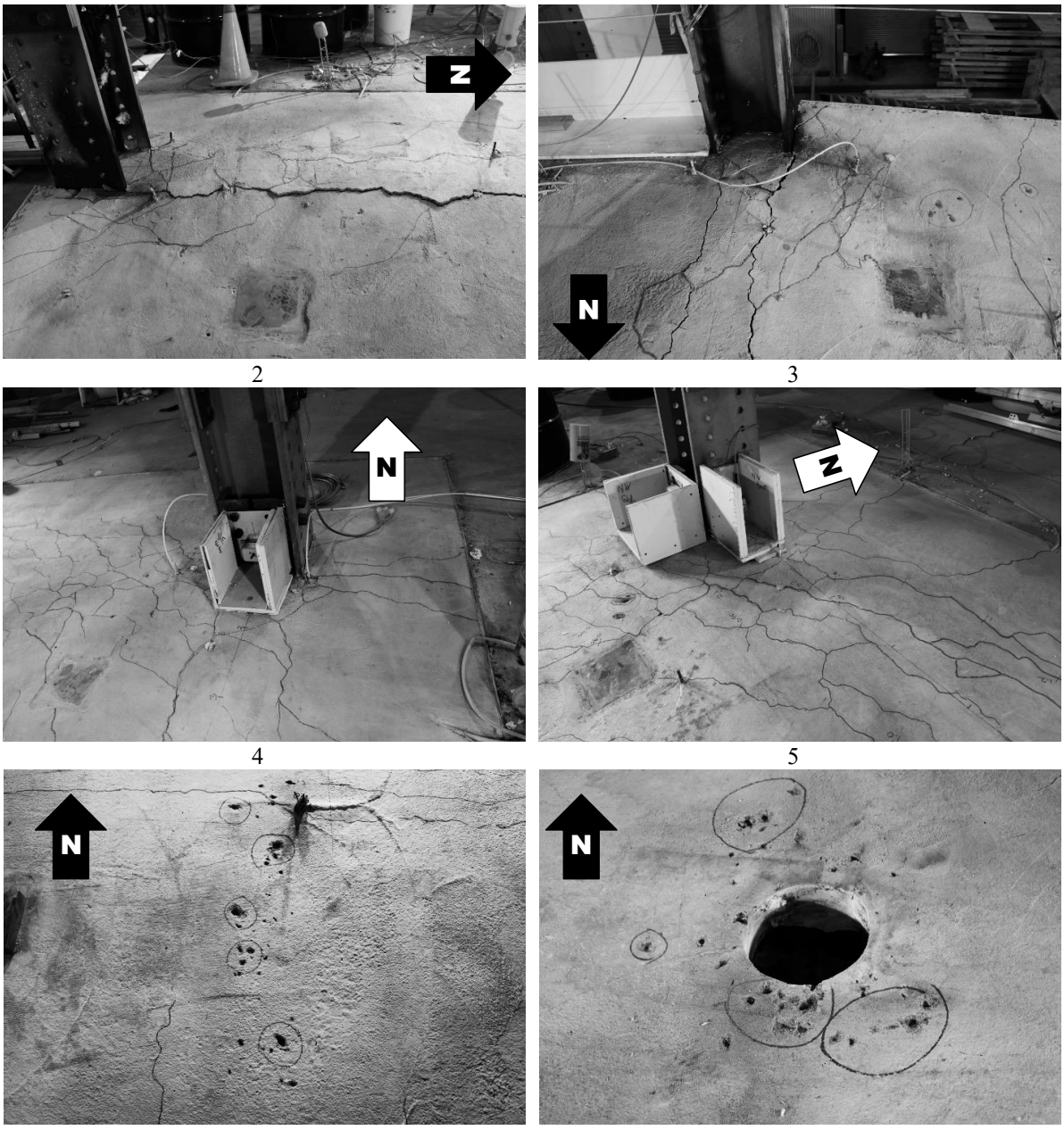

Fig. 35. Post-test photographs of the test floor slab, including closeups of concrete damage at locations 2 through 7.

3.6.2. Steel Deck and Beams

Some post-test photographs of the floor specimen soffit (i.e., the ceiling of the test compartment) and closeups of the damaged parts are provided in Fig. 36 and Fig. 37. As shown, the test fire caused extensive damages to the steel decking across the entire test bay. All floor beams, suffered from a test fire, exhibited permanent global deflection and local buckling, although the severity of steel deformations varied among beams. The north and south primary beams exhibited some degree of lateral deformation and twisting, whereas the secondary beam was mostly bent in its strong axis.

In this test, all three 9.1 m long beams (W16×31) as well as the west girder (W18×35) that was 6.1 m long exhibited both flange and web local buckling toward the end connections. The secondary beam (W16×31) clearly exhibited local buckling at its west end (location 6 in Fig. 37), but local buckling at its east end appeared to be minor. Instead, the W14×22 secondary beam framing to the east surrounding bay locally buckled near its connection to the east girder in the test bay (location 5). The west girder also exhibited a local rupture of the bottom web toe at the north end, possibly caused by local buckling at this end region. Refer to Appendix A.11 for additional photographs of the deflected beams and girders disassembled from the test bay. It is also noteworthy that the applied SFRM coating turned black particularly near the ends of the secondary beam (locations 5 and 6), directly above the east and west burners. This result was possibly involved with high temperature oxidation of steel at 900 °C or higher but needs further examination to confirm the cause of this discoloration. Refer to Appendix A.12 for the initial inspections of the black colored SFRM samples.

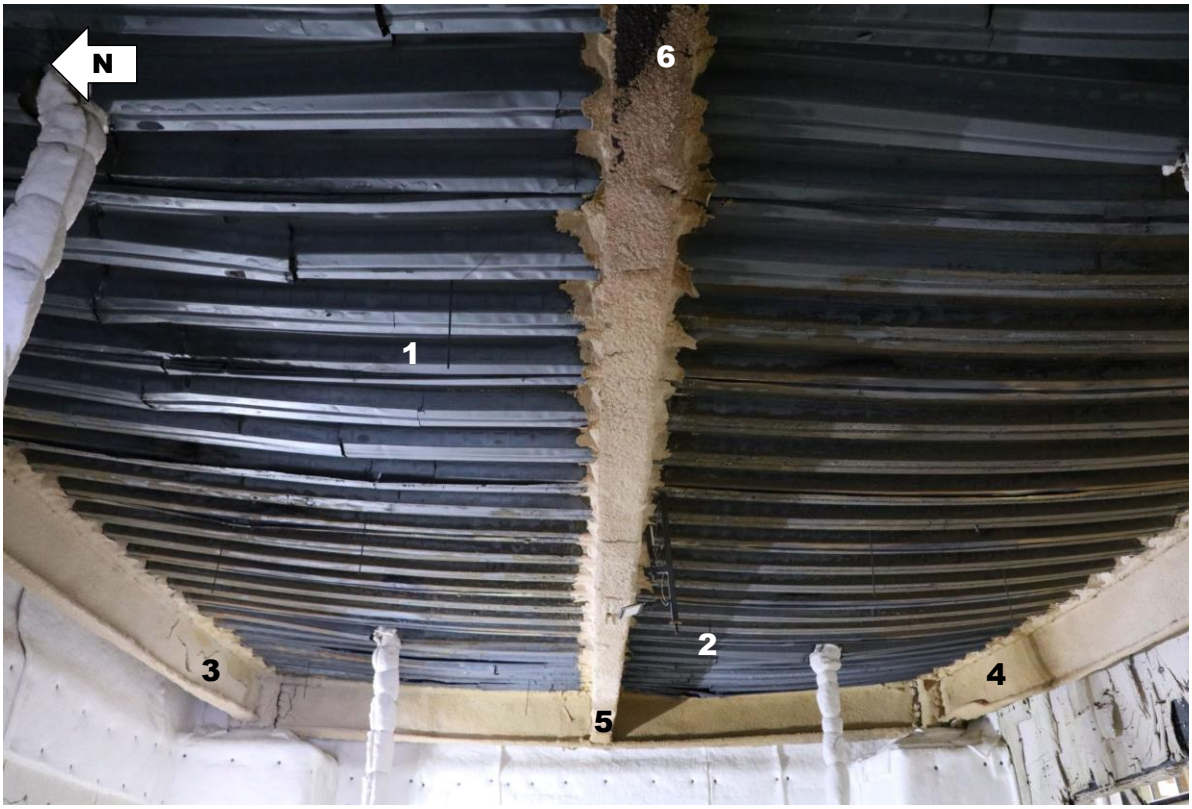

Fig. 36. Post-test photograph of the floor specimen soffit.

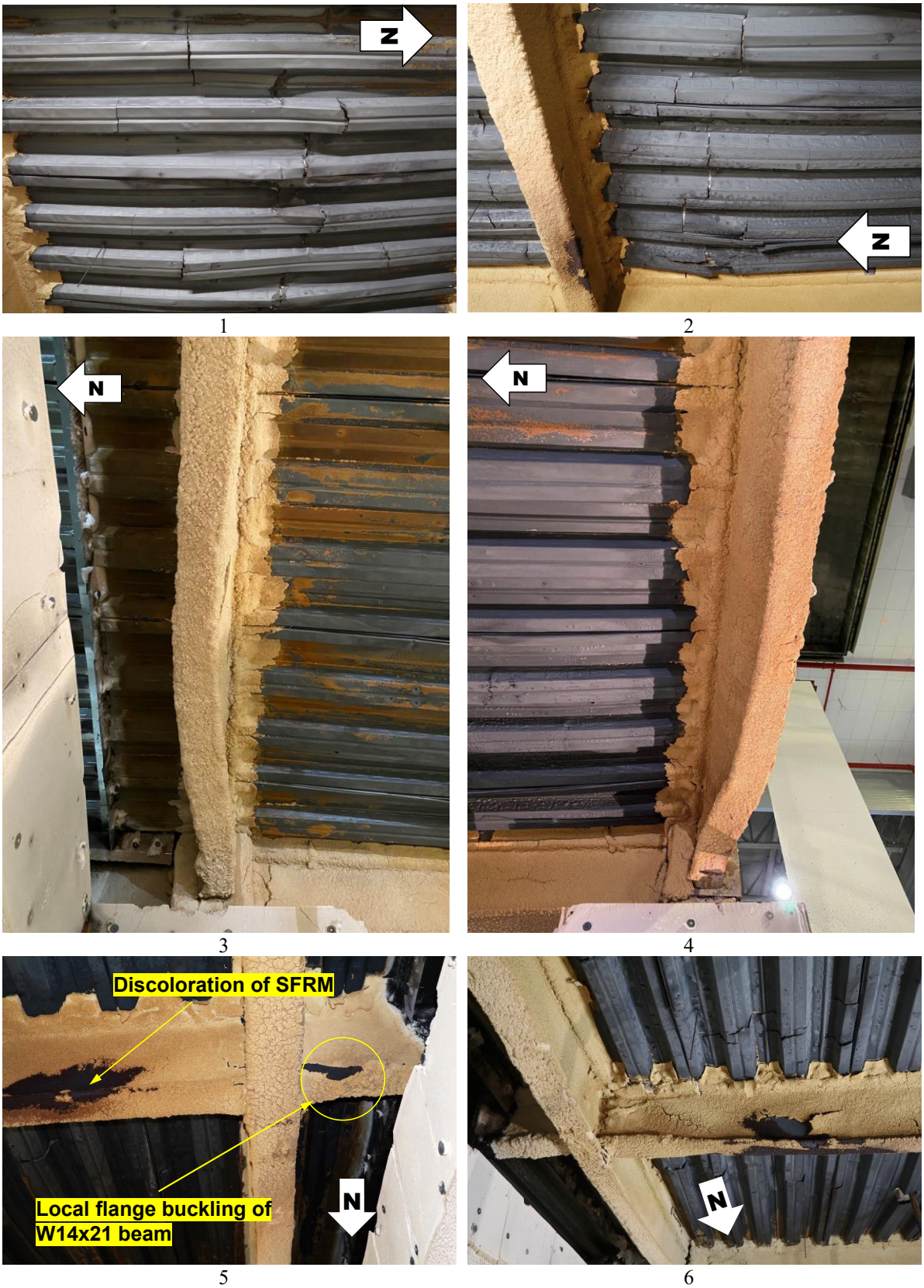

Fig. 37. Closeup photographs of steel damage at locations 1 through 6 shown in Fig. 36.

3.6.3. Steel Connections

Although the east and west girders (W18×35) exhibited relatively smaller deformations compared to the W16×31 beams, the girder-end connections deformed more than the beam-end connections. Overall, all shear tab connections appeared to be robust. Any indications of steel ruptures were not identified. The use of short-slot holes for the connecting plate and the slab continuity achieved by continuous No.3 reinforcing bars might help reduce the stress concentration in the connection region while allowing the large vertical displacement of the connected beams during the heating phases of the test fire.

Some photographs of the shear tab connections taken after the fire test are shown in Fig. 38. As shown, the standard shear tabs mostly remained straight with local elongation around the bolt holes. However, the extended shear tabs twisted as the floor specimen expanded in the east-west direction. The bottom bolts connected at the south ends of the girders exhibited some degree of bending. Additional post-test photographs are presented in Appendix A.11.

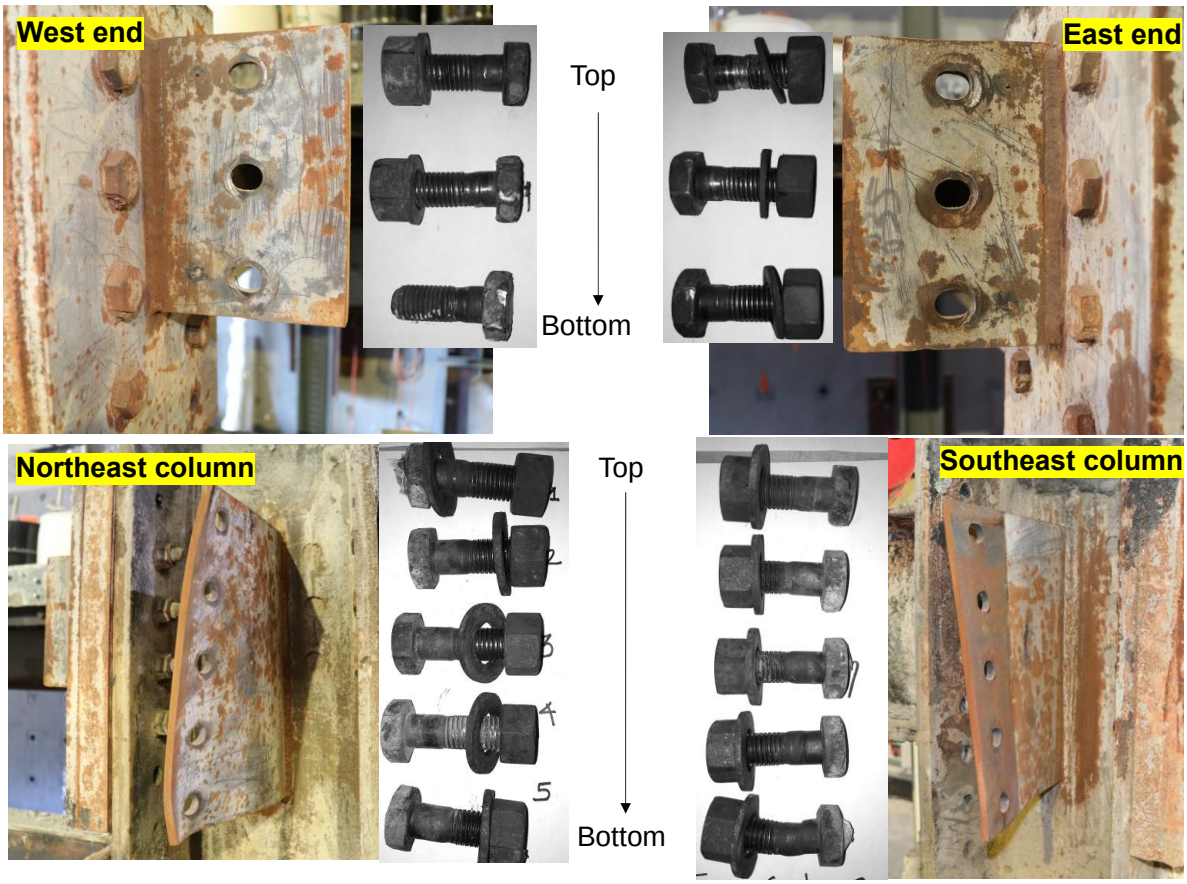

Fig. 38. Post-test photographs of the standard shear tab connections of the north edge beam (top) and the extended shear tab connections of the east girder (bottom).

4. Summary and Conclusions

The second fire experiment (Test #2) was conducted on the 9.1 m × 6.1 m composite floor to investigate the influence of the steel reinforcement scheme on the fire resilience of the full-scale composite floor subjected to combined mechanical and fire loading. This report has described details of the experimental design and construction, the fire test conditions, and the experimental test results. In this test, the slab reinforcement scheme of the test floor assembly consisted of No.3 deformed bars with the spacing of 30.5 cm, resulting in the equivalent area of 230 mm^2/m slab width. All other conditions remained identical or comparable to those used in the first experiment (Test #1) of this test program, including the specimen geometry, beam-end connections, test fire curves, imposed gravity loads, and passive fire protection of the exposed steel frame.

While sustaining a mechanical load of 125 kN, the test floor assembly was heated by the natural gas fueled compartment fire with the peak heat release rate approximately equal to 12 MW. The natural gas burners were switched off at 131 min, whereas mechanical loading was continued over a 2-hr cooling period.

Some key observations and conclusions drawn from Test #2 are summarized as follows:

1) The average upper layer gas temperature within the test bay was approximately 10 % higher than that specified in ASTM E119 standard and approximately 5 % higher than the temperature measured in Test #1. The peak average temperature was recorded at 1130 °C. The standard deviation in temperature measurements (from twelve thermocouples) was less than 50 °C, indicating practically uniform heating conditions beneath the test floor assembly.

2) The SFRM protected steel beams (W16×31) were heated to 850 °C on average at the bottom flanges until the test fire was extinguished. The top surface temperature of the floor slab reached nearly 200 °C during heating and further increased to 230 °C during the cooling phase of the test fire. A larger temperature variation existed among the embedded No. 3 reinforcing bars. The bars located within the shallow section of the floor slab were heated to 540 °C, whereas those placed on the top of the SFRM protected steel beams remained below 200 °C during fire loading.

3) The mid-panel vertical displacement reached 455 mm at 131 min in fire. The peak displacement of 475 mm was measured about 15 min after the test fire was extinguished. The vertical and horizontal displacements of the test assembly increased more slowly with temperature compared to those observed in Test #1. This result might be attributed to the slab continuity (through No.3 bars) in the hogging moment region, which were maintained during the heating phase.

4) The No.3 bars placed in the test floor slab appeared to effectively control the formation of large concrete cracks during heating. Most of concrete cracks including those in the hogging moment region were less than 5 mm wide after cooldown. Unlike Test #1, this floor specimen exhibited unique transverse cracks on the south half of the slab in addition to the longitudinal cracks along the beams. There were several spots indicating localized aggregate spalling at the transverse centerline of the test assembly and the slab

penetration holes for loading tubes. From the post-test inspections, only one longitudinal bar next to the southwest column was found to be ruptured.

5) The test fire in Test #2 caused extensive damage (ruptures) to the exposed steel deck compared to Test #1. All fire-exposed beams exhibited some degree of permanent global deflection and local buckling; however, all shear-tab connections appeared to be intact and robust after cooling. No steel ruptures in connection elements (plates, bolts and welds) were identified. All four extended shear tabs connecting the girders significantly bent due to thermal expansion of the floor specimen.

6) The floor specimen reinforced with No. 3 bars retained a large flexural strength even after cooled down from fire exposure. No additional structural damage was reported until the floor specimen was loaded to 90 % of the calculated nominal capacity at ambient temperature. This high post-fire residual strength might be attributed to combination of several factors including (1) the rotational restraint provided by the steel reinforcement in the hogging moment region, (2) the negligible damage in headed stud anchors which developed as-designed composite action between the steel beams and concrete slabs under flexural loading, and (3) the compressive strength of the concrete surrounding the headed studs which appeared to be less affected by thermal degradation as temperatures were measured lower than 200 °C in those locations.

This second test suggests that the fire resilience of the composite floor can be significantly improved by using a higher reinforcement ratio achieved with No.3 reinforcing bars as the slab reinforcement instead welded wire mesh. As future work, it is necessary to study the failure mechanism of the composite floor undergoing tensile membrane action in fire and to confirm the possibility of removing SFRM on the secondary beam(s) for economic construction, which will be of interest for the third experiment (Test #3) scheduled for early 2022. The experimental results presented in this paper can be used for validation of predictive models to perform parametric studies incorporating the variability in the steel reinforcement scheme (area, spacing, and material) for safer and cost-effective composite floor construction for fire safety.

References

[1] British Steel, "The Behaviour of multi-storey steel frame buildings in fire," Rotherham, 1999.

[2] F. Wald *et al.*, "Experimental behaviour of a steel structure under natural fire," *Fire Saf. J.*, vol. 41, no. 7, Oct. 2006, doi: 10.1016/j.firesaf.2006.05.006.

[3] C. Bailey, "Design of steel structures with composite slabs at the fire limit state," Garston, Unite Kingdom, 2000.

[4] C. Bailey, "Steel structures supporting composite floor slabs: design for fire," Garston, Unite Kingdom, 2001.

[5] C. G. Bailey, "Efficient arrangement of reinforcement for membrane behaviour of composite floor slabs in fire conditions," *J. Constr. Steel Res.*, vol. 59, no. 7, pp. 931–949, 2003, doi: 10.1016/S0143-974X(02)00116-5.

[6] B. Zhao, M. Roosefid, and O. Vassart, "Full Scale Test of a Steel and Concrete Compoiste Floor Exposed to ISO fire," *5th Int. Conferece Struct. Fire*, no. June, 2008.

[7] B. Zhao, M. Roosefid, and A. Breunese, "Connections of Steel and Composite Structures under Natural Fire Conditions (COSSFIRE)," Luxemburg, 2011.

[8] L. Lim and C. Wade, "Experimental Fire Tests of Two-Way Concrete Slabs," 2014.

[9] ISO, *Fire-resistance tests — Elements of building construction — Part 2: Requirements and recommendations for measuring furnace exposure on test samples*. Geneva: ISO, 2019.

[10] C. G. Bailey and W. S. Toh, "Behaviour of concrete floor slabs at ambient and elevated temperatures," *Fire Saf. J.*, vol. 42, no. 6–7, pp. 425–436, 2007, doi: 10.1016/j.firesaf.2006.11.009.

[11] American National Standards Institute/Steel Deck Institute, *ANSI/SDI C-2017 Standard for Composite Steel Floor Deck-Slabs*. Steel Deck Insititute (SDI), 2017.

[12] UL (Underwriters Laboratory). Fire Resistance Ratings – ANSI/UL 263. UL, Northbrook, IL, 2011..

[13] ASTM International, "E119-21 Standard Methods of Fire Test of Building Construction and Materials." ASTM International, West Conshohocken, PA, 2021.

[14] G. M. Newman, "The Fire Resistance of Composite Floor with Steel Decking-SCI Publication P56," Berkshire, 1990.

[15] AISC, *Specification for Structural Steel Buildings (ANSI/AISC 360-16)*. Chicago: AISC, 2016.

[16] ASCE, *Minimum Design Loads and Associated Criteria for Buildings and Other Structures*. Reston, VA: American Society of Civil Engineers, 2017.

[17] ASCE, *ASCE MOP 138 Structural Fire Engineering*, vol. 138. Reston, VA: American Society of Civil Engineers, 2018.

[18] L. Choe *et al.*, "Fire Resilience of a Steel-Concrete Composite Floor System: Full-Scale Experimental Evaluation for U.S. Prescriptive Approach with a 2-Hour Fire-Resistance Rating (Test #1)," Gaithersburg, MD, Oct. 2021. doi: 10.6028/NIST.TN.2165.

[19] C. Zhang, W. Grosshandler, A. Sauca, and L. Choe, "Design of an ASTM E119 Fire Environment in a Large Compartment," *Fire Technol.*, vol. 56, no. 3, pp. 1155–1177, 2020, doi: 10.1007/s10694-019-00924-7.

[20] American Concrete Institute, *Building Code Requriments for Strucutral Concrete (ACI 318-19)*. Farmington Hills, MI: American Concrete Institute, 2019.

[21] G. Clifton, A. Gillies, and N. Mago, "The Slab Panel Method: Design of Composite Floor Systems for Dependable Inelastic Response to Severe Fires," 2010.
[22] R. Sabelli, T. a Sabol, and S. W. Easterling, "Seismic Design of Composite Steel Deck and Concrete-Filled Diaphragms," *NEHRP Seism. Des. Tech. Br. No. 5*, no. 5, 2011.
[23] AISC (American Institute of Steel Construction). Manual of Steel Construction, 15th Edition. Chicago: AISC, 2017.
[24] ASTM International, "ASTM E8/E8-21 Standard Test Methods for Tension Testing of Metallic Materials." ASTM International, West Conshohocken, PA, 2021, [Online]. Available: https://www.astm.org/e0008_e0008m-21.html.
[25] ICC, *2018 International Building Code*. Country Club Hills, IL: ICC, 2018.
[26] C. Maluk, L. Bisby, and G. P. Terrasi, "Effects of polypropylene fibre type and dose on the propensity for heat-induced concrete spalling," *Eng. Struct.*, vol. 141, pp. 584–595, 2017, doi: 10.1016/j.engstruct.2017.03.058.
[27] M. Pour-Ghaz, J. Castro, E. J. Kladivko, and J. Weiss, "Characterizing Lightweight Aggregate Desorption at High Relative Humidities Using a Pressure Plate Apparatus," *J. Mater. Civ. Eng.*, vol. 24, no. 8, pp. 961–969, Aug. 2012, doi: 10.1061/(ASCE)MT.1943-5533.0000422.
[28] ASTM International, "C192/C192M-19 Standard Practice for Making and Curing Concrete Test Specimens in the Laboratory." ASTM International, West Conshohocken, PA, 2019.
[29] R. A. Bryant and M. F. Bundy, "The NIST 20 MW calorimetry measurement system for large-fire research," *NIST Tech. Note 2077*, 2019.
[30] B. N. Taylor and C. E. Kuyatt, "Guidelines for Evaluating and Expressing the Uncertainty of NIST Measurement Results: Appendix D1. Terminology," *Natl. Inst. Stand. Technol. Gaithersburg, MD*, p. D.1.1.2, 2001, [Online]. Available: http://physics.nist.gov/TN1297.
[31] OMEGA Engineering, "Super OMEGACALD XL Thermocouple Probes," 2021. https://assets.omega.com/pdf/test-and-measurement-equipment/temperature/sensors/thermocouple-probes/TJ36CAXL_NNXL.pdf.
[32] OMEGA Engineering, "Thermocouple Wire Duplex Insulated," 2021. https://assets.omega.com/pdf/cable-and-wire/thermocouple-and-rtd-wire-and-cable/XC_K_TC_WIRE.pdf.
[33] OMEGA Engineering, "High Temperature Wire with Nextel or Silica Yarn Fiber Insulation." .
[34] UniMeasure, "PA Series String Potentiometers." https://unimeasure.com/products/standard-series/.
[35] Tokyo Measuring Instruments Lab, "TML Strain Gagues." [Online]. Available: https://tml.jp/e/product/strain_gauge.
[36] MKS, "MKS Instruments." https://www.mksinst.com/.
[37] Olympus, "Delta XRF Analyzer." https://www.olympus-ims.com/en/xrf-xrd/xrf-handheld/.

Appendix A: Instrumentation, Raw Data, and Photographs

A.1. Mechanical Loading

Four servo-hydraulic actuators (each named as NW, NE, SW, and SE) were used to apply mechanical loads that were uniformly distributed at twenty-four points across the test floor slab. Those actuators were mounted at the NFRL basement below the fire test bay (Fig. 39). Each actuator provided mechanical loading on the test floor at six points spaced 152 cm apart (Fig. 40a). The beam strains were measured using strain gauges during mechanical loading at ambient temperatures only (Fig. 40b). Measured actuator loads, actuator displacements, and the beam strain values are provided in Fig. 41 and Fig. 42.

Fig. 39. Screenshot of the test video to monitor hydraulic actuators at the basement of the NFRL strong floor (prior to fire testing).

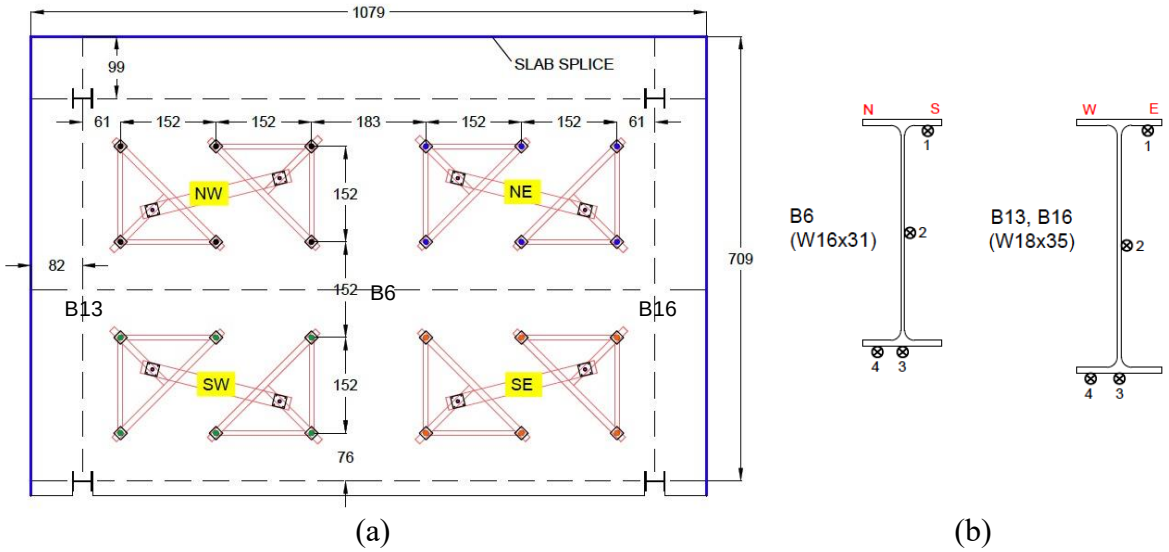

Fig. 40. Locations of (a) loading points tied to four hydraulic actuators (NE, NW, SE, SW) and (b) strain gauges installed at midspan of the test bay floor beams. Dimensions are in cm.

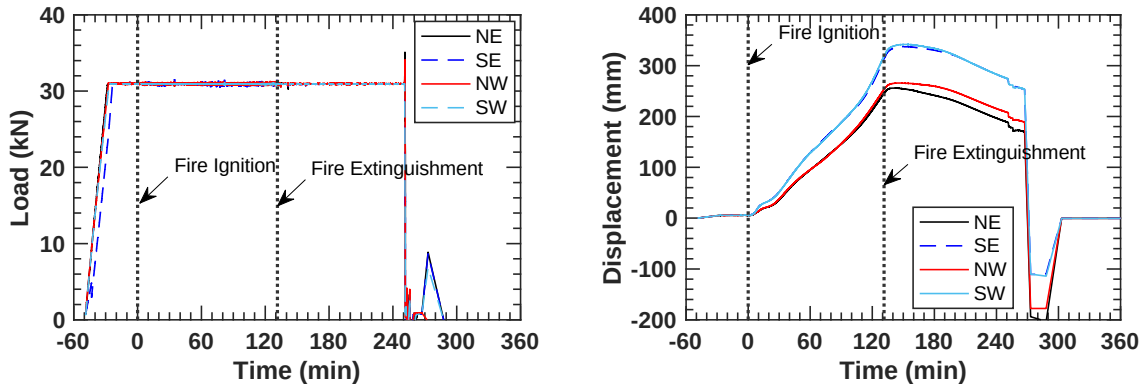

(a) (b)

Fig. 41. Actuator data: (a) mechanical force and (b) stroke displacement of four hydraulic actuators (NE, SE, NW, and SW) used in the test.

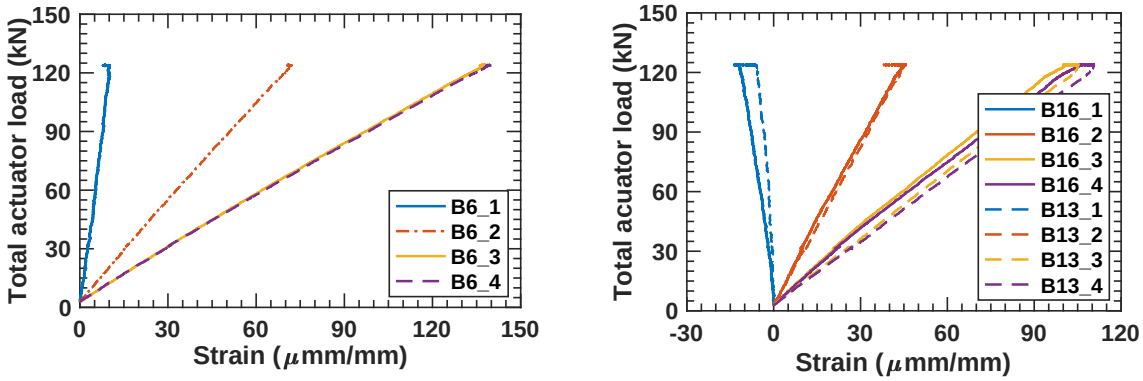

(a) (b)

Fig. 42. Beam strains prior during the ambient temperature mechanical loading: (a) secondary beam and (b) girders at midspan in the test bay.

A.2. Gas Temperature

OMEGACLAD sheathed thermocouples (model: TJ36-CAXL-14U-24) [31] were used to measure the gas temperatures inside the test compartment. Twelve thermocouple probes (TCC1 through TCC12) were mounted 30.5 cm (z = 346 cm) below the floor specimen soffit (i.e., the compartment ceiling) for gas temperature measurements. Two thermocouple trees were placed inside the test compartment, including the north tree 79 cm from the north wall (NorthTC) and the south tree 96 cm from the south wall (SouthTC). Thermocouple probes were located approx. 10 cm away from the exposed surface of Kaowool blanket wrapping the mounting stand. Photographs of some installed thermocouple probes are shown in Fig. 44.

The hottest spot was measured at TCC5 which was approximately 50 °C above the average upper layer gas temperature. TCC11 indicated the lowest temperature, about 50 °C below the average value. During cooling, temperatures of TCC6 decreased much quicker than TCC11.

In addition, during the first 15 min of heating, the gas temperatures measured at the north and south trees differed by a maximum of 100 °C, due to air intake through the south ventilation opening. However, this temperature variability also became smaller as the test fire continued longer than an hour.

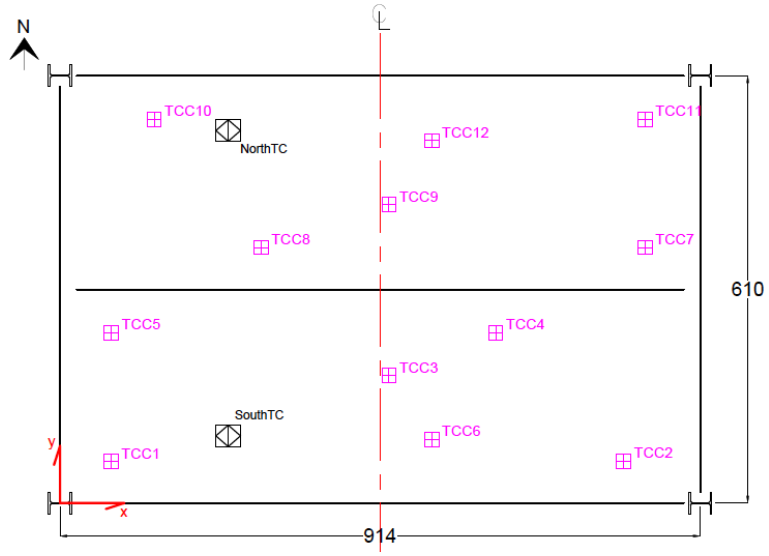

Name/ID	X East+	Y North+	Z Up+
TCC1	73	60	346
TCC2	805	60	346
TCC3	470	182	346
TCC4	622	242	346
TCC5	73	244	346
TCC6	531	90	346
TCC7	835	364	346
TCC8	287	364	346
TCC9	470	425	346
TCC10	134	547	346
TCC11	835	547	346
TCC12	531	517	346
NorthTC1	240	531	302
NorthTC2	240	531	201
NorthTC3	240	531	102
SouthTC1	240	96	302
SouthTC2	240	96	201
SouthTC3	240	96	102

Fig. 43. Locations of thermocouple probes used for gas temperature measurements within the fire test bay. The Z datum of NorthTC and SouthTC probes is at top surface of the compartment floor. Dimensions and coordinates are in cm.

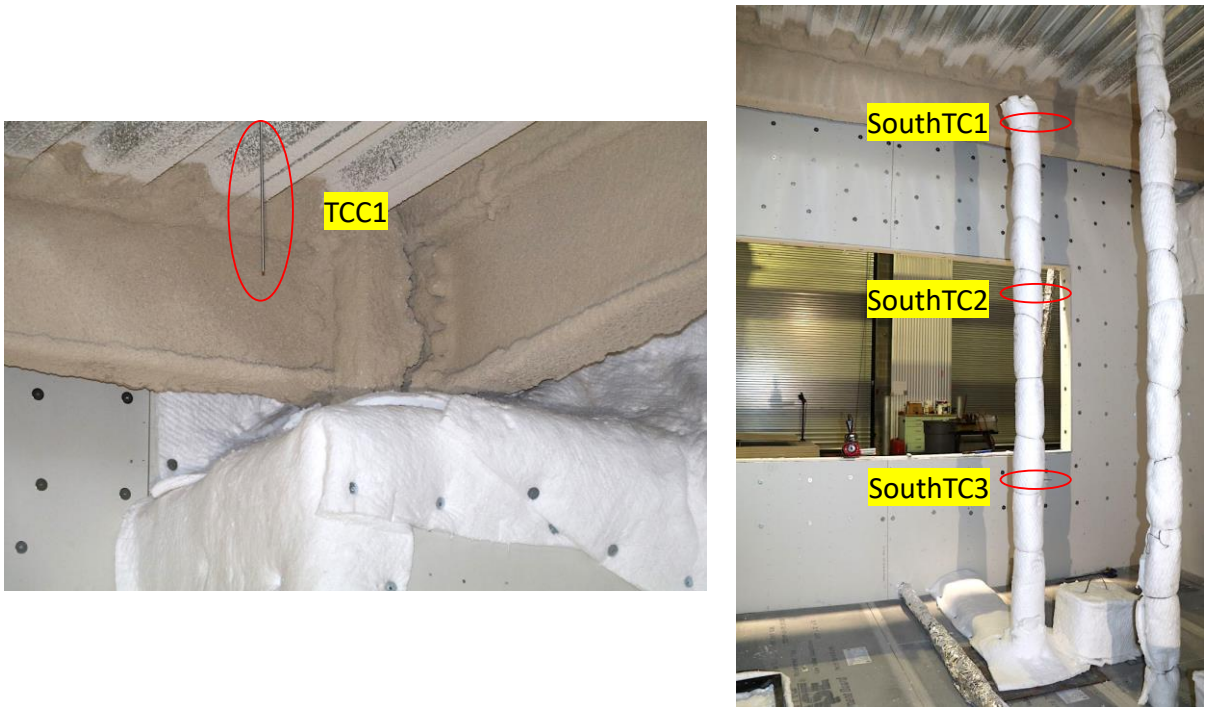

Fig. 44. Photographs of installed TCC1 and SouthTC probes.

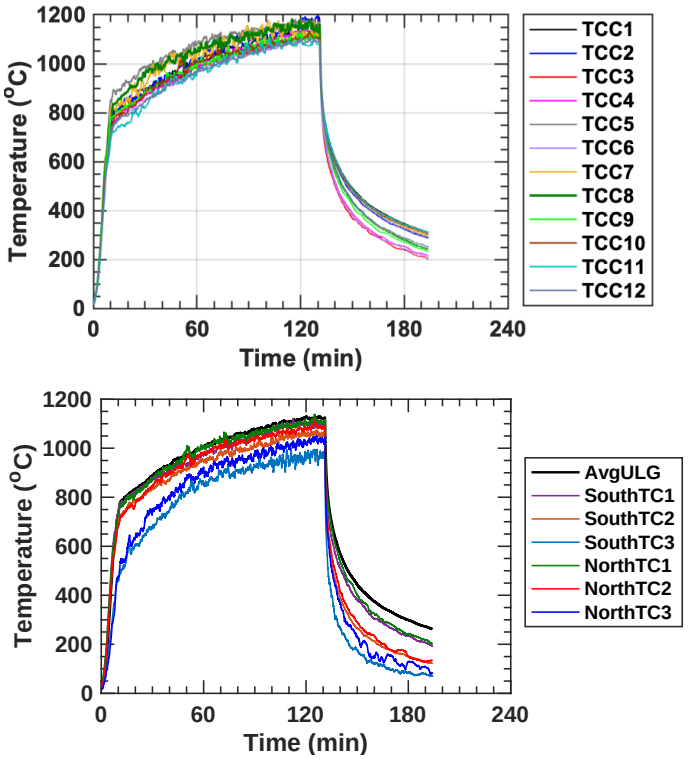

Fig. 45. Gas temperatures inside the test compartment. Fire was extinguished at 131 min.

A.3. Concrete Temperature

Glass sheathed thermocouples (model: GG-K-24) [32] were used to measure concrete temperatures. A total of ten thermocouple trees, made of the 10 cm diameter concrete cylinders, were placed in the test floor slab. Locations of these cylinders (TST1 through TST8) are shown in Fig. 46. In each cylinder, two to four thermocouples were secured through the thickness of the slab, except for TSTi_5* which was mounted 3 mm above the deck pan.

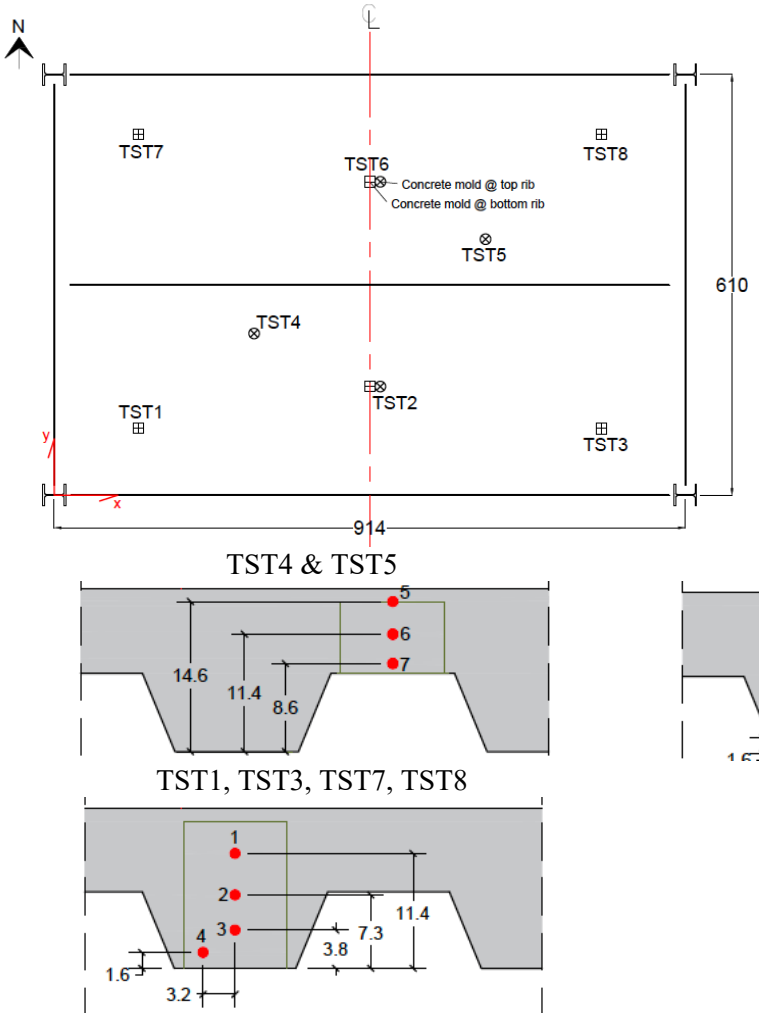

Section	Name/ID	X East+	Y North+
Bottom rib	TST1	122	97
Bottom rib	TST2	457	157
Top rib	TST2	472	157
Bottom rib	TST3	488	97
Bottom rib	TST4	290	234
Bottom rib	TST5	625	377
Bottom rib	TST6	457	454
Top rib	TST6	472	454
Bottom rib	TST7	122	523
Bottom rib	TST8	792	523

Fig. 46. Locations of thermocouples installed within the test floor slab. Dimensions and coordinates are in cm.

Table 12 shows the list of thermocouple probes used to estimate the average temperatures at specific depths which are plotted in Fig. 20. For this estimation, locations 1 and 2 only included TST1 and TST6 thermocouples only because thermocouples at other TST locations appeared to be significantly affected by concrete damage. With the same reason, locations 6 and 7 only included TST 4 through TST6 thermocouples. All raw data are plotted in Fig. 47, where some temperature readings (e.g., TST2_1, TST2_2, TST3_1, and TST3_2) started increasing rapidly after 60 min to 70 min into heating.

Table 12. List of thermocouples used to estimate the average temperatures plotted in Fig. 20.

Plot legend	Channel ID	Maximum standard deviation, °C
1	TST1_1, TST6_1	10
2	TST1_2, TST6_2	20
3	TST1_3, TST3_3, TST7_3, TST8_3, TST2_3, TST6_3	150
4	TST1_4, TST3_4, TST7_4, TST8_4, TST2_4, TST6_4	150
5	TST4_5, TST5_5	160
6	TST4_6, TST5_6, TST2_6, TST6_6	60
7	TST4_7, TST5_7, TST2_7, TST6_7	50
5*	TST2_5, TST6_5	110

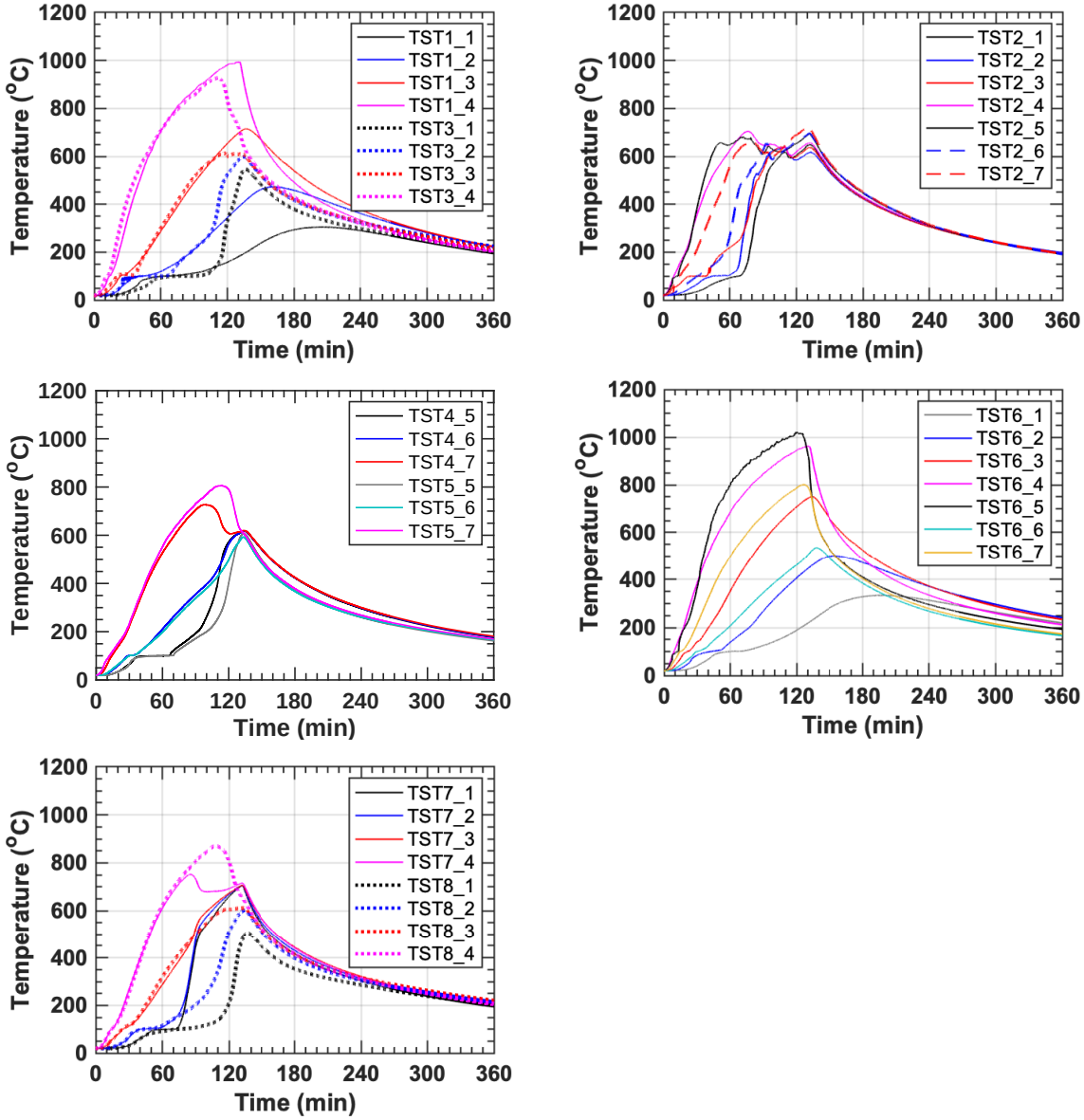

Fig. 47. Concrete temperatures through the depth of the test floor slab. Fire was extinguished at 131 min.

A total of eight thermocouples (labeled with TopSlab1 through TopSlab8) were mounted 3 mm below the top (unexposed) surface of the test bay slab. Locations of these thermocouples and raw temperature data are provided in Fig. 48 and Fig. 49, respectively. As shown, temperatures continued to rise during the cooling phase of the test fire (up to 1 h into cooling). The peak temperatures were in the range of 110 °C to 180 °C because of the use of the profiled steel decking. Temperatures measured at top of the deep slab section (TopSlab1, TopSlab2, TopSlab6, and TopSlab8) varied significantly, possibly due to variation in the moisture content at those locations at the time of fire testing. Table 13 shows the list of thermocouple probes used to estimate the average temperatures at specific depths which are plotted in Fig. 21a.

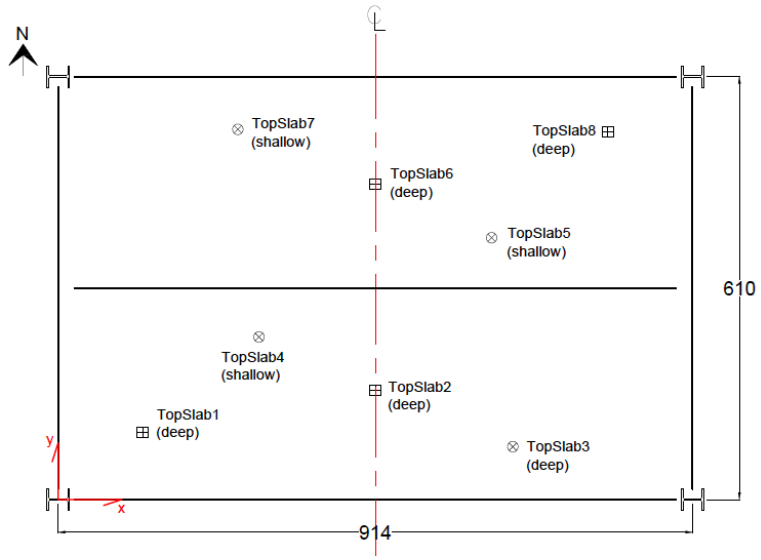

Section	Name/ID	X East+	Y North+
Deep	TopSlab1	122	97
Deep	TopSlab2	457	157
Deep	TopSlab3	655	76
Shallow	TopSlab4	290	234
Shallow	TopSlab5	625	377
Deep	TopSlab6	457	454
Deep	TopSlab7	259	533
Deep	TopSlab8	792	530

Fig. 48. Locations of thermocouple probes used for temperature measurements of top (unexposed) surface of the test floor slab. Dimensions and coordinates are in cm.

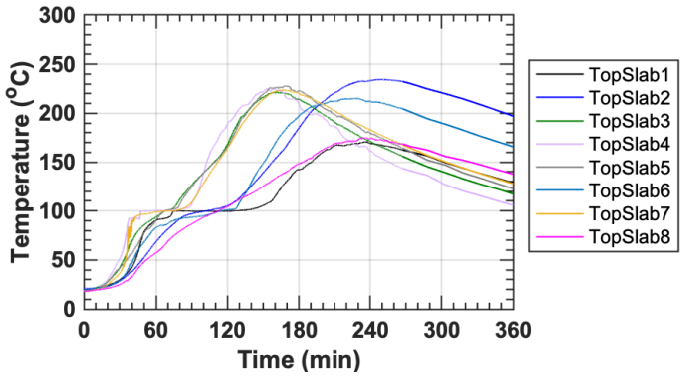

Fig. 49. Top surface temperatures of the test floor slab. Fire was extinguished at 131 min.

Table 13. List of thermocouples used to estimate the average temperatures plotted in Fig. 21a.

Plot legend	Channel ID	Maximum standard deviation, °C
Shallow	TopSlab3, TopSlab4, TopSlab5, TopSlab7	20
Deep	TopSlab1, TopSlab2, TopSlab6, TopSlab8	30

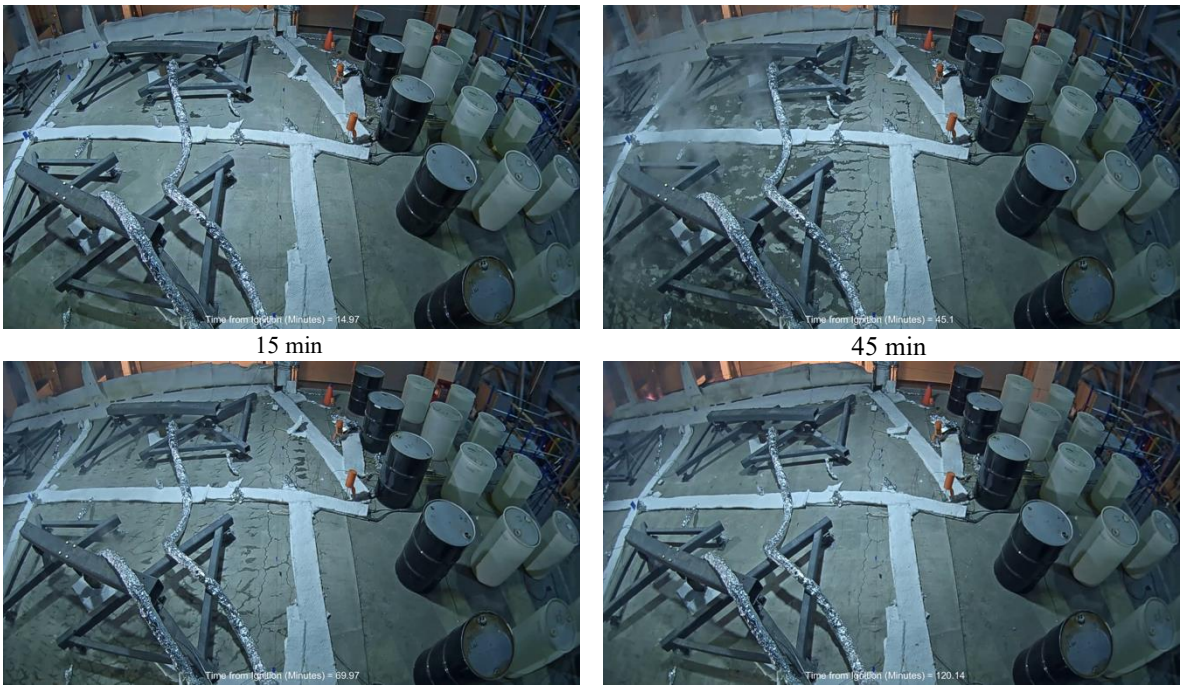

Fig. 50. Screenshots of the test video showing the west half of the test slab captured at 15 min, 45 min, 70 min, and 120 min following the fire ignition.

A.4. Reinforcing Bar Temperature

Glass sheathed thermocouples (model: GG-K-24) [32] were used to measure temperatures of embedded No. 3 bars in the test-bay floor slab. Locations of thermocouples and raw data are presented in Fig. 51 and Fig. 52, respectively. Temperatures of the No.3 bars above the steel beams and girders at midspan are measured using the S group thermocouples as described in Sect. A.5.

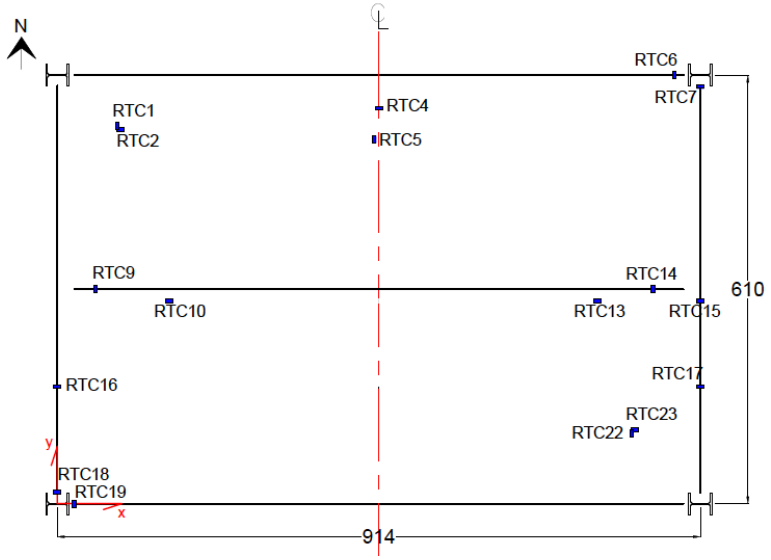

Name/ID	X East+	Y North+	Z Up+	Bar Orientation
RTC1	85	537	11.4	Transverse
RTC2	90	237	10.5	Longituidnal
RTC4	457	563	10.5	Longituidnal
RTC5	451	518	11.4	Transverse
RTC6	877	610	11.4	Transverse
RTC7	914	800	10.5	Longituidnal
RTC9	54	305	11.4	Transverse
RTC10	159	288	10.5	Longituidnal
RTC13	768	288	10.5	Longituidnal
RTC14	847	305	11.4	Transverse
RTC15	914	288	10.5	Longituidnal
RTC16	0	167	10.5	Longituidnal
RTC17	914	167	10.5	Longituidnal
RTC18	0	17	10.5	Longituidnal
RTC19	24	0	11.4	Transverse
RTC22	817	100	11.4	Transverse
RTC23	822	105	10.5	Longituidnal

Fig. 51. Distribution of thermocouple probes mounted on No.3 deformed bars. Dimensions and coordinates are in cm.

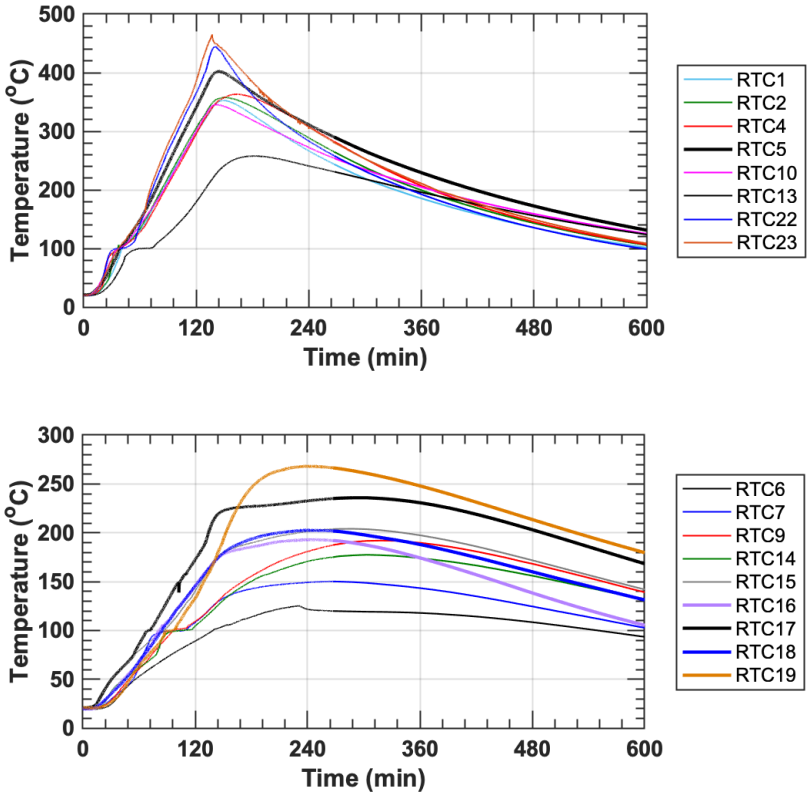

Fig. 52. Temperatures of No.3 deformed bars placed inside the test floor slab.

Table 14 shows the list of thermocouple probes used to estimate the average temperatures at specific depths which are plotted in Fig. 21b. For this estimation, thermocouples mounted on the bars not directly placed above the steel beams and girders as well as some TST group thermocouples mounted at a similar depth within the test slab (Refer to Sect. A.3).

Table 14. List of thermocouples used to estimate the average bar temperatures plotted in Fig. 21b.

Plot legend	Channel ID	Maximum standard deviation, °C
Deep Section	TST1_1, TST6_1, RTC1, RTC2, RTC4, RTC5, RTC22, RTC23	90
Shallow Section	TST4_6, TST5_6, TST6_6	60

A.5. Composite Section Temperature

For the composite beam sections, temperature measurements were performed using K-type thermocouples with two different wire insulation techniques: glass sheathed thermocouples (model: GG-K-24) mounted within the concrete slab and the ceramic sheathed thermocouples (model: XT-K-20-SLE) [33] directly peened on the surface of the steel beam shapes. An example of thermocouples installed prior to the slab cast and fireproofing spray is shown in Fig. 53. Locations of thermocouples and raw data are provided in Fig. 54 through Fig. 56. As shown, some temperature readings acquired at section 6 (TB6 and S6 groups) appeared to be significantly influenced by concrete cracks or failure in thermocouple probes particularly after 60 min into heating due to deformations in the test floor. Table 15 shows the list of thermocouple probes used to estimate the average temperatures at specific depths across the composite beam section, which are plotted in Fig. 23.

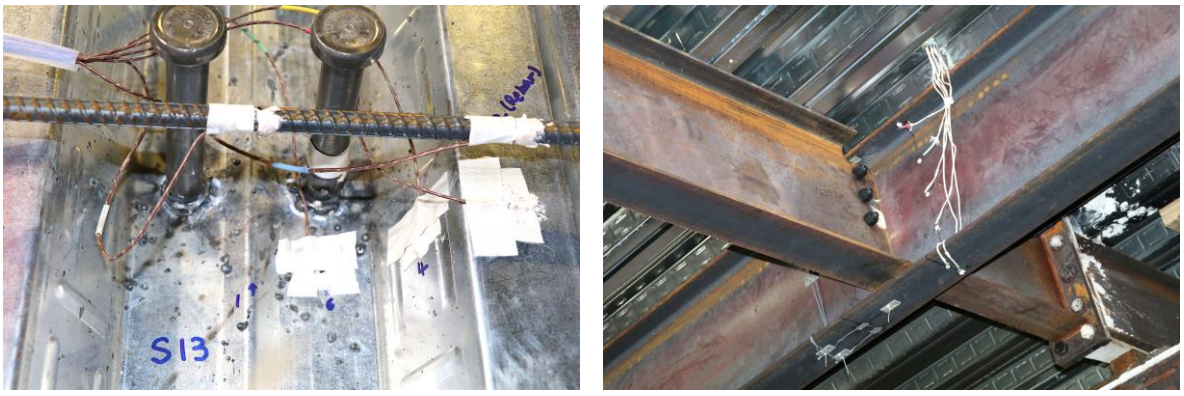

Fig. 53. Photographs of typical thermocouples installed in the composite girder near its midspan.

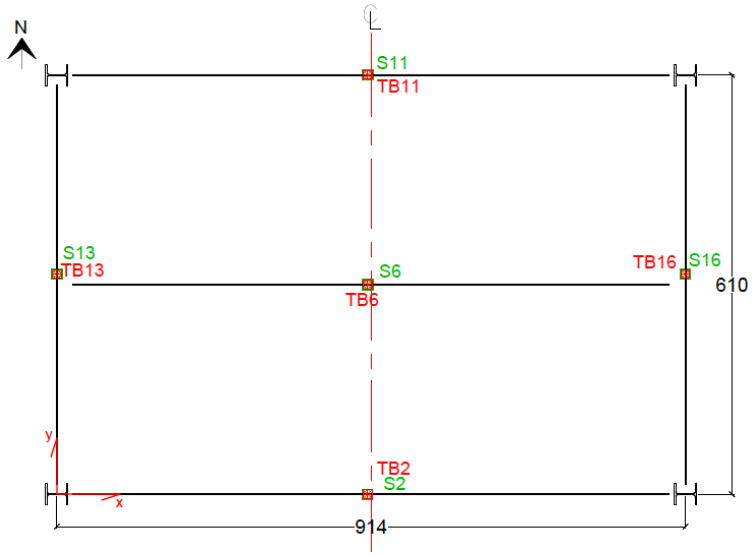

Name/ID	X East+	Y North+
S2, TB2	452	0
S6, TB6	452	305
S11, TB11	452	610
S13, TB13	0	320
S16, TB16	914	320

Fig. 54. Labels and locations of the group of thermocouples installed at the midspan composite beams (W16×31) and girders (W18×35). Dimensions and coordinates are in cm.

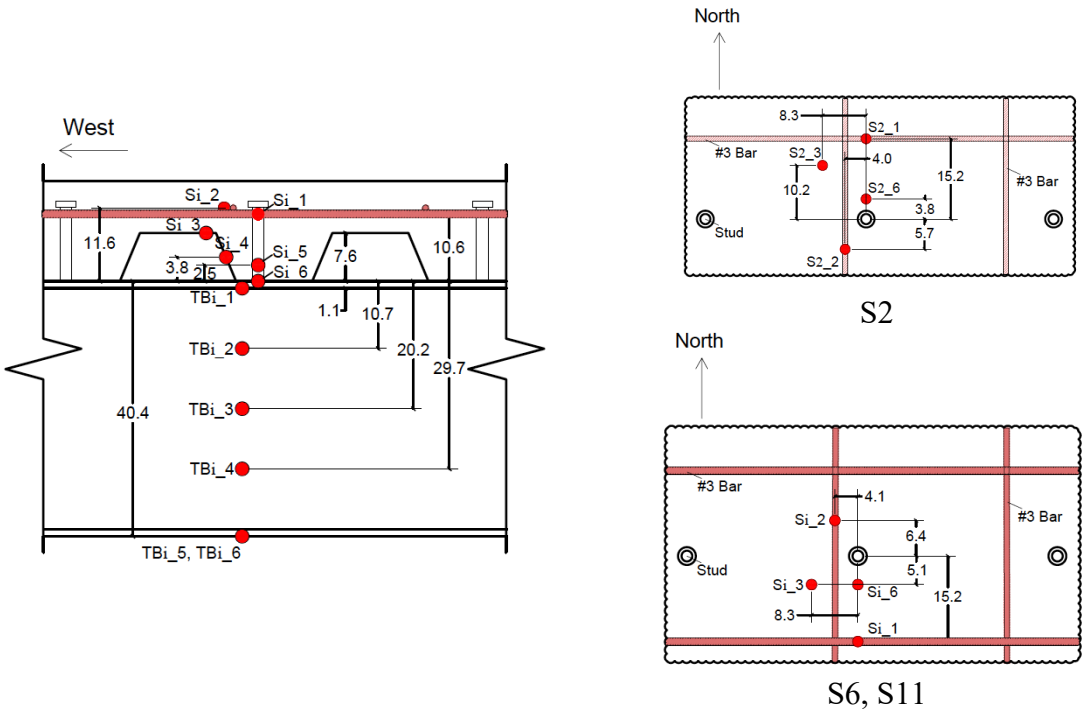

Fig. 55. Locations of individual thermocouples mounted at midspan of W16×31 composite beams, where i = thermocouple group number, 2, 6, or 11. Dimensions are in cm.

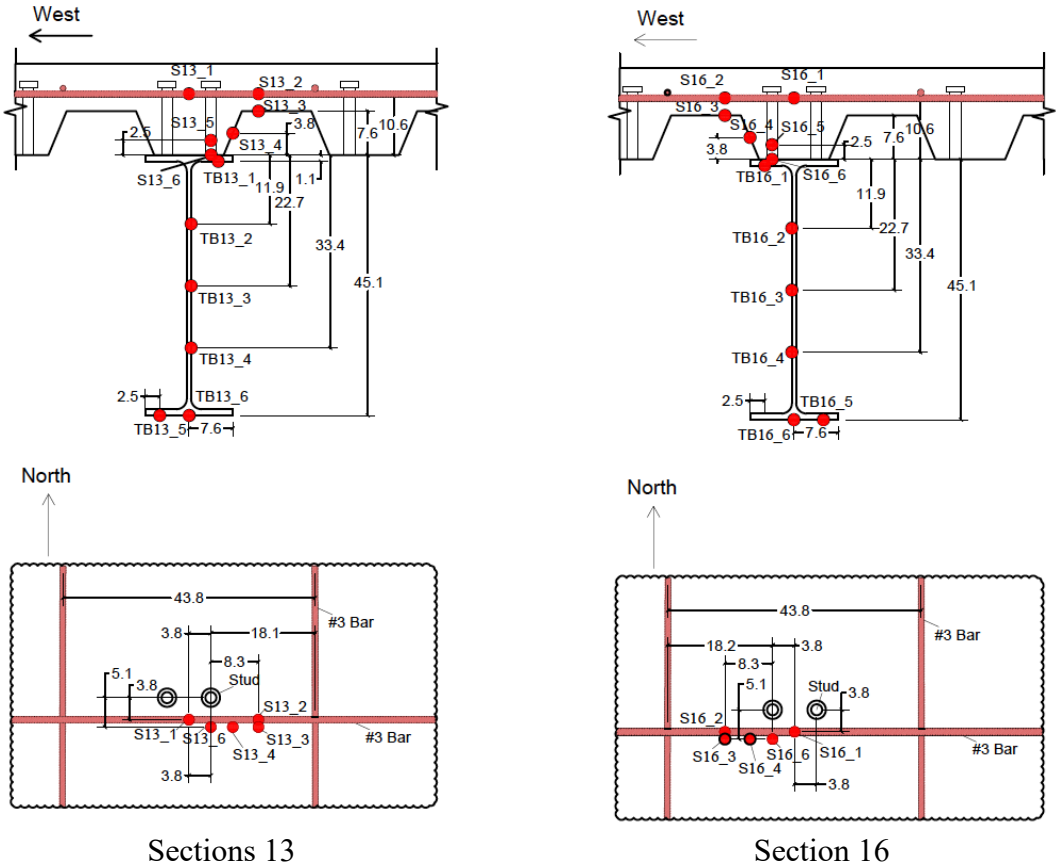

Fig. 56. Locations of individual thermocouples mounted at midspan of W18×35 composite girders, where i = thermocouple group number, 13 or 16. Dimensions are in cm.

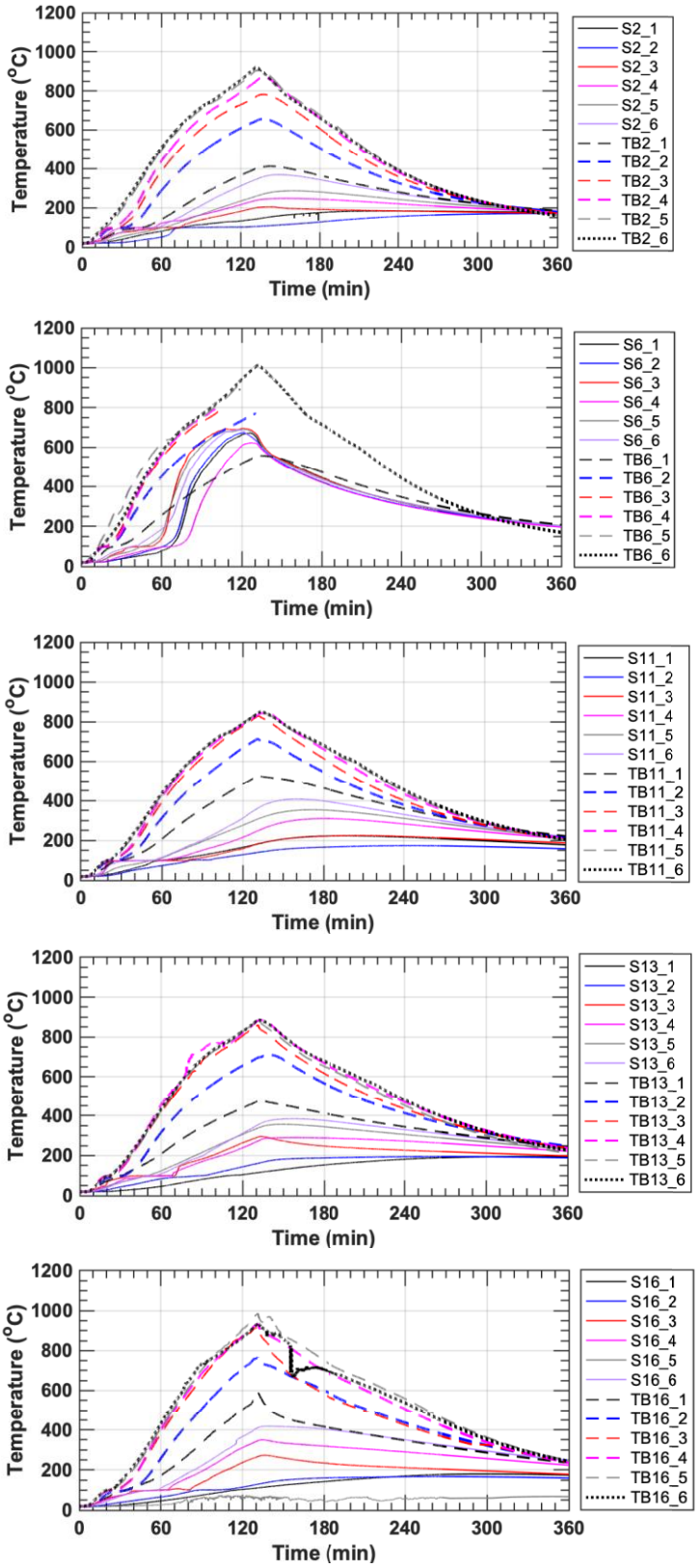

Fig. 57. Measured temperatures of midspan composite beam and composite girder sections in the test bay

Table 15. List of thermocouples used to estimate the average temperatures of composite beams and girders plotted in

	Composite Beam (W16×31)		Composite Beam (W18×35)	
Plot legend in Fig.	Channel ID	Max std, °C	Channel ID	Max std, °C
(1)	S2_1, S2_2, S6_1, S6_2, S11_1, S11_2		S13_1, S16_1	
(2)	S2_5, S6_5, S11_5		S13_5, S16_5	
(3)	S2_3, S6_3, S11_3		S13_3, S16_3	
(4)	TB2_1, TB6_1, TB11_1		TB13_1, TB16_1	
(5)	TB2_2, TB6_2, TB11_2		TB13_2, TB16_2	
(6)	TB2_3, TB2_4, TB2_5, TB2_6, TB6_3, TB6_4, TB6_5, TB6_6, TB11_3, TB11_4, TB11_5, TB11_6		TB13_4, TB16_4	

A.6. Steel Beam and Girder Temperature

Ceramic sheathed thermocouples (model: XT-K-20-SLE) [33] were used to measure temperatures of the steel beams and girders in the fire test bay. Temperatures of the SFRM-protected steel beams (W16×31) and steel girders (W18×35) were measured at various locations. Temperatures measured in the sections TB2, TB6, TB11, TB13, and TB16 are presented in Sect. B.4. TB17_3 was malfunctioned from the beginning of the test.

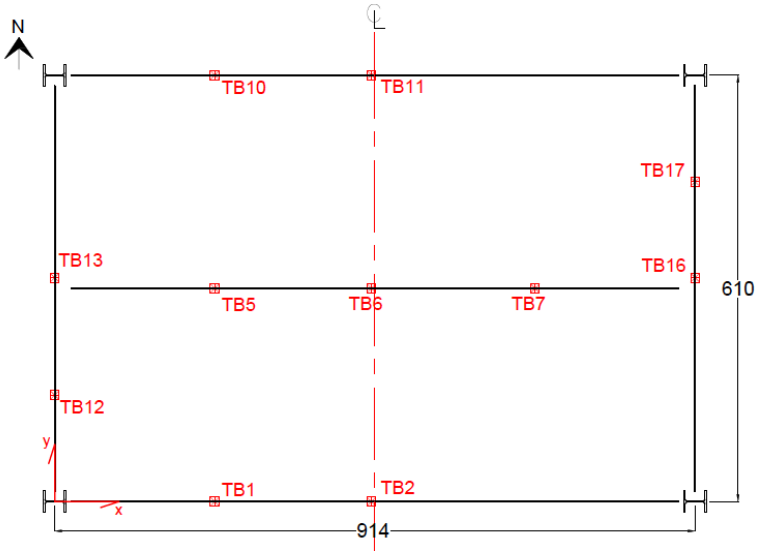

Name/ID	X East+	Y North+
TB1	229	0
TB5	229	305
TB7	686	305
TB10	229	610
TB12	0	152
TB17	914	457

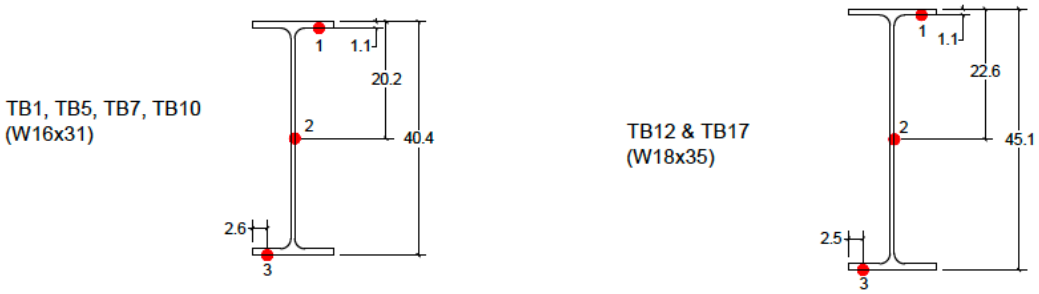

Fig. 58. Locations of thermocouples mounted on steel beams and girders of the test floor assembly. Dimensions and coordinates are in cm.

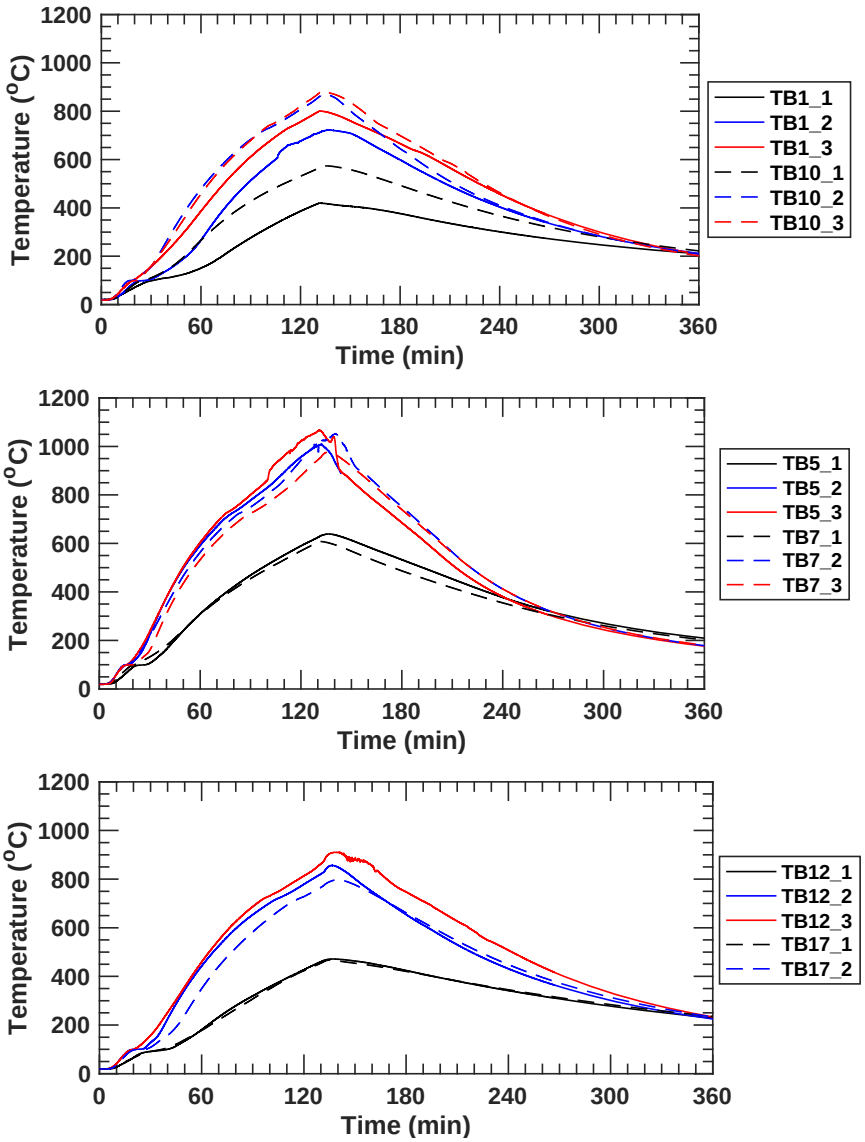

Fig. 59. Measured temperatures of steel beams and girders. Fire was extinguished at 131 min.

A.7. Steel Connection Temperature

Ceramic sheathed thermocouples (model: XT-K-20-SLE) [33] were used to measure temperatures on the beam-end connection regions. As shown in Fig. 60 (p. 71-74), the C group thermocouples were mounted on the steel connection elements protected with SFRM; the SC group thermocouples were installed inside the concrete slab and on the steel deck pan above the steel connections. Measured temperatures are plotted in Fig. 61 as a function of the fire exposure time.

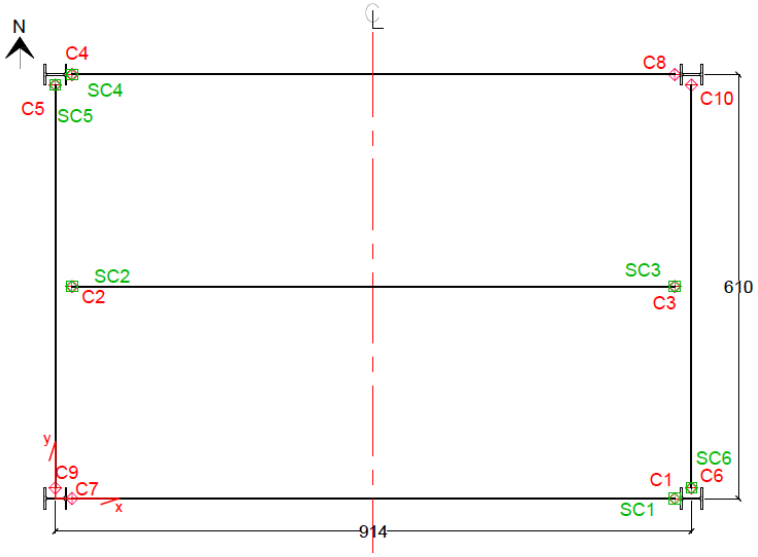

Name/ID	X East+	Y North+
C1, SC1	884	0
C2, SC2	8	305
C3, SC3	906	305
C4, SC4	30	610
C5, SC5	1	588
C6, SC6	914	22
C7	30	0
C8	884	610
C9	0	22
C10	914	588

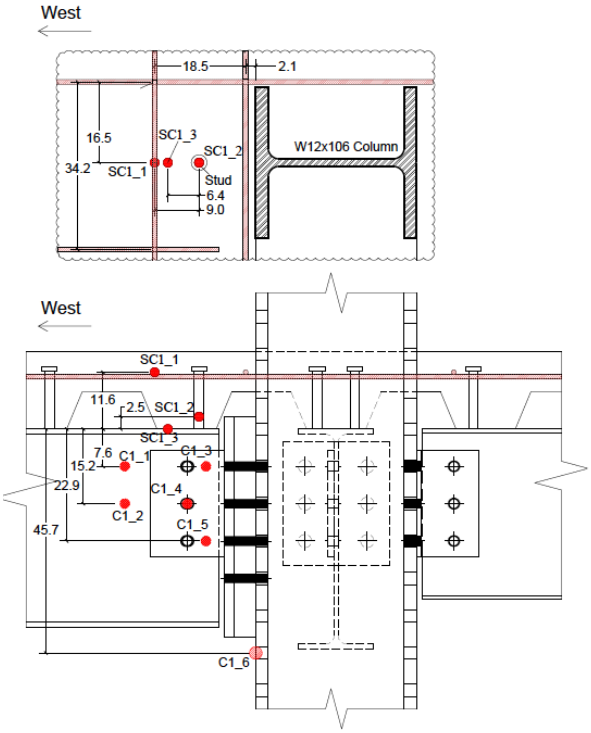

C1, SC1

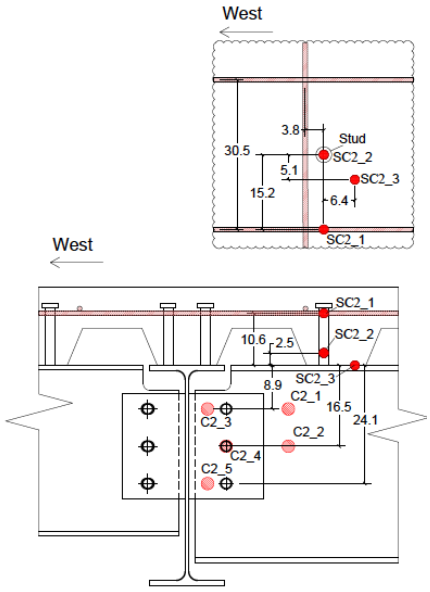

C2, SC2

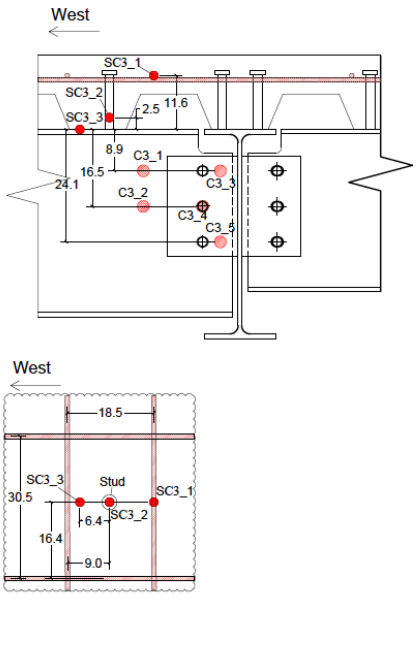

C3, SC3

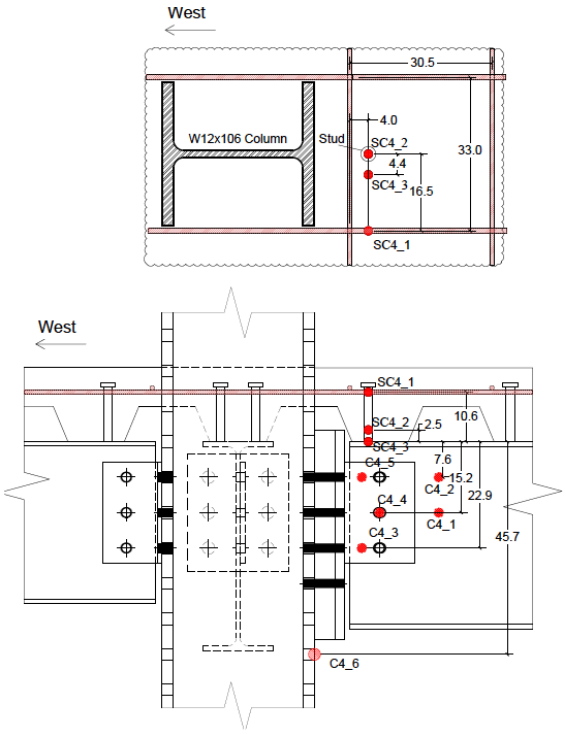

C4, SC4

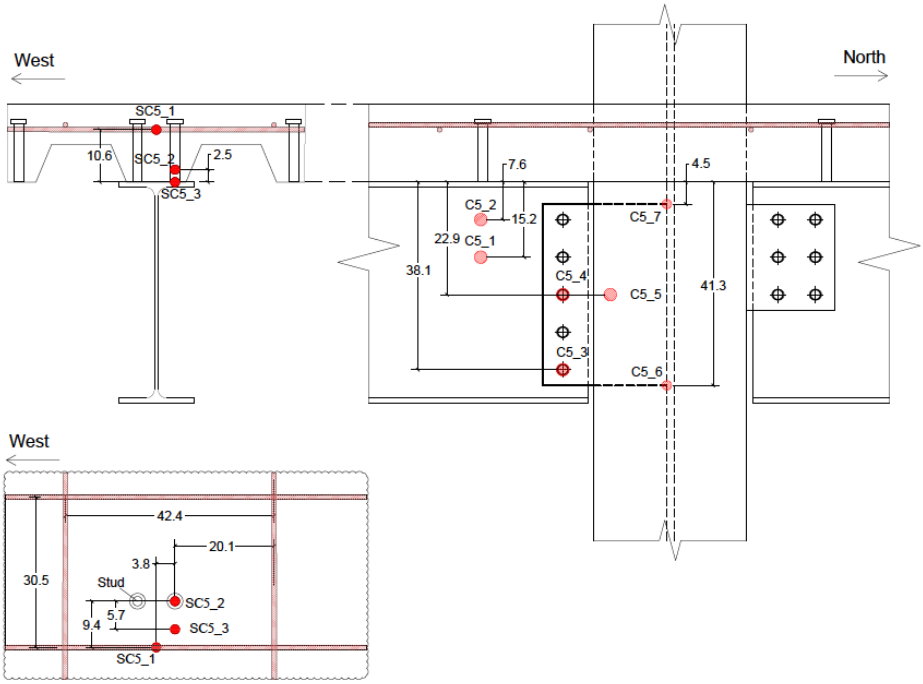

C5, SC5

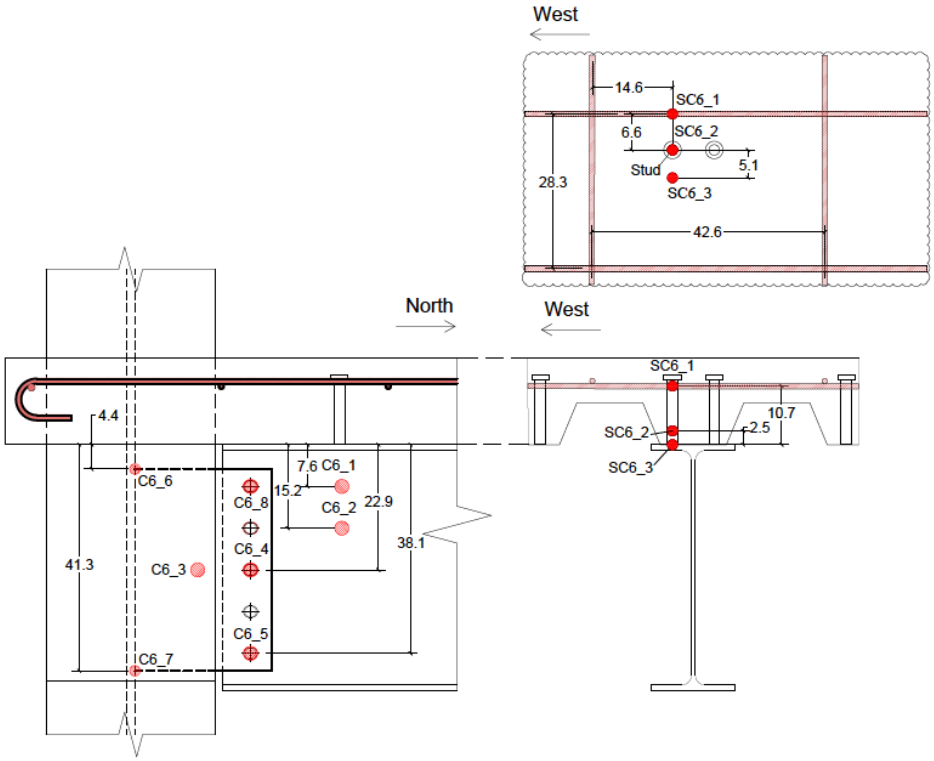

C6, SC6

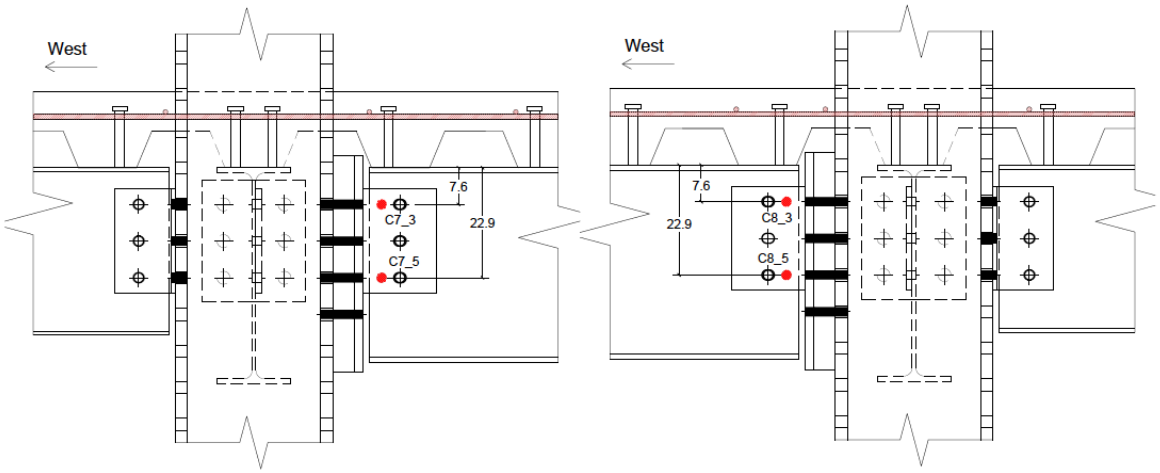

C7 (left), C8 (right)

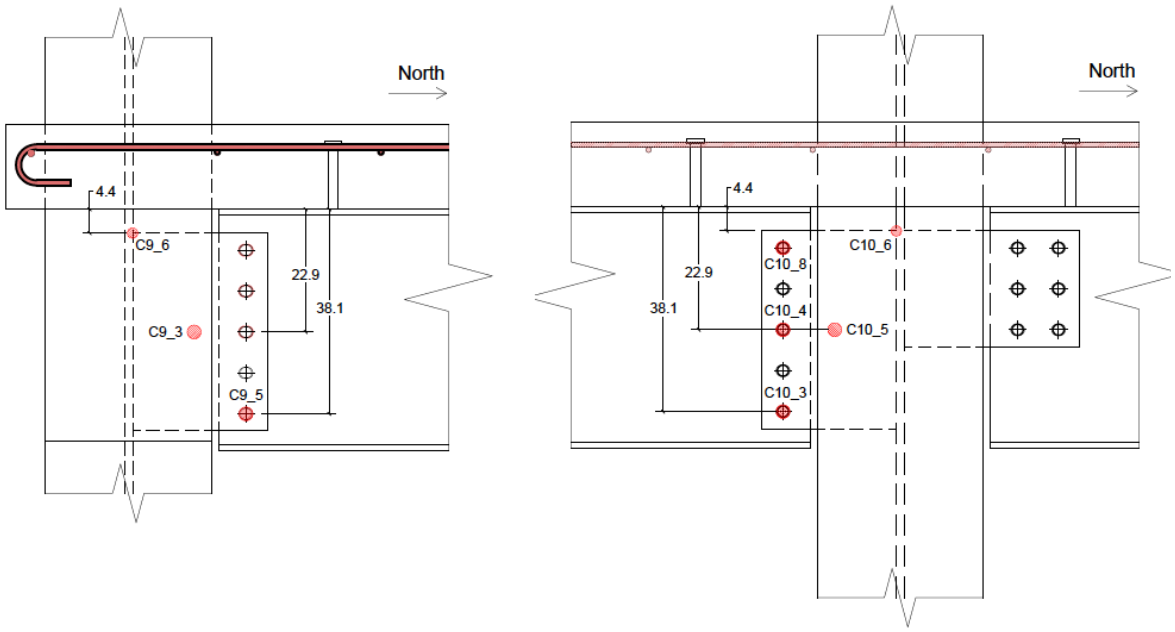

C9 (left), C10 (right)

Fig. 60. Locations of thermocouples mounted on the beam-end connection regions. Dimensions and coordinates are in cm.

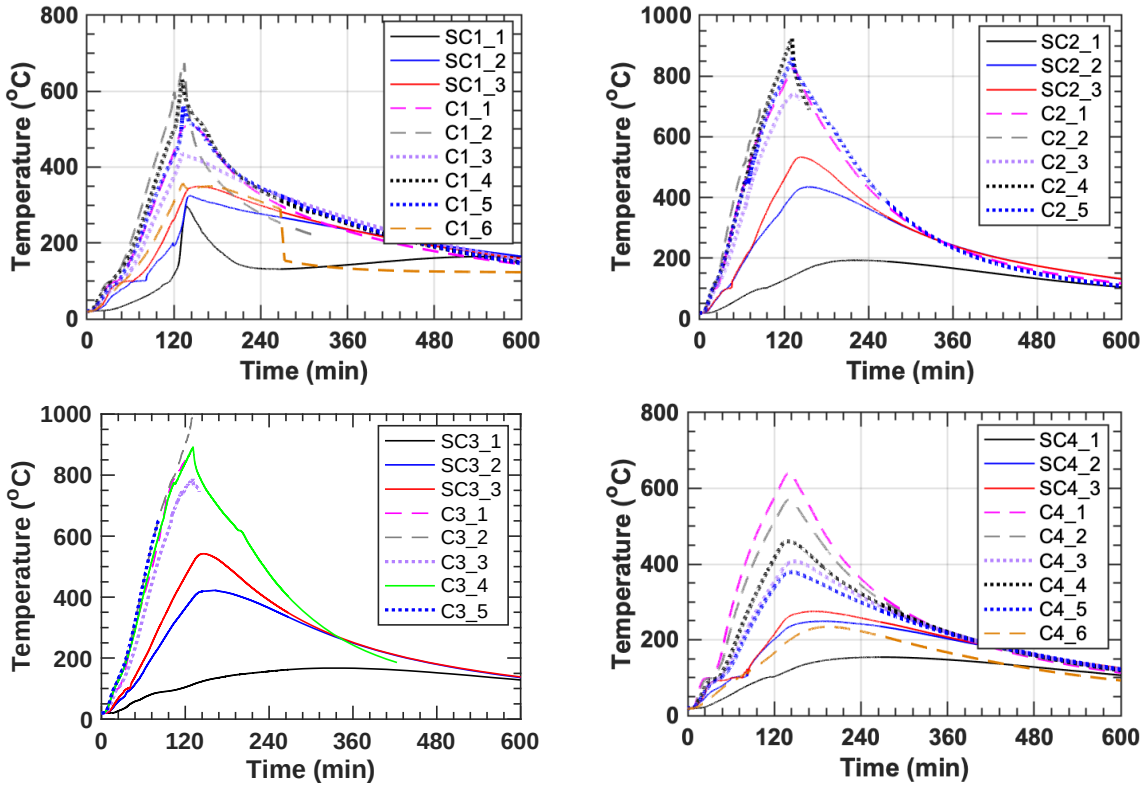

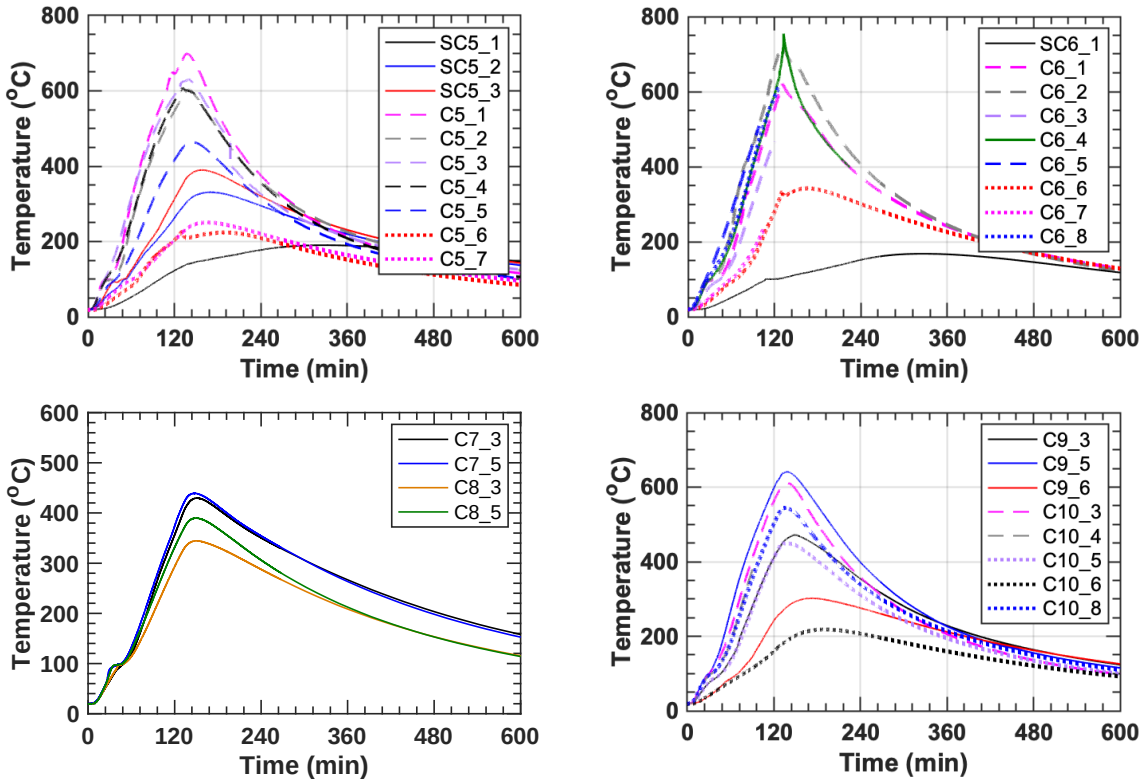

Fig. 61. Measured temperatures of the beam-end connection regions. Fire was extinguished at 131 min.

A.8. Displacement

Displacement measurements were performed using string potentiometers (model: PA series manufactured by UniMeasure [34]) All sensors were installed using mounting frames isolated from the test structure, except for VD11 which was used to measure the relative vertical displacement between the first and second story girders at midspan. Refer to Sect. 3.4 for locations of installed sensors. Fig. 62 shows the displacement data not presented in Sect. 3.4. The positive values on the y axes of the graph charts below indicate either the vertical displacement (VD) toward the strong (ground) floor or the horizontal displacement (HD) at various locations of the test building in response to thermal expansion of the test floor during fire. Some video snapshots showing the top of the test floor during fire loading are provided in Fig. 63.

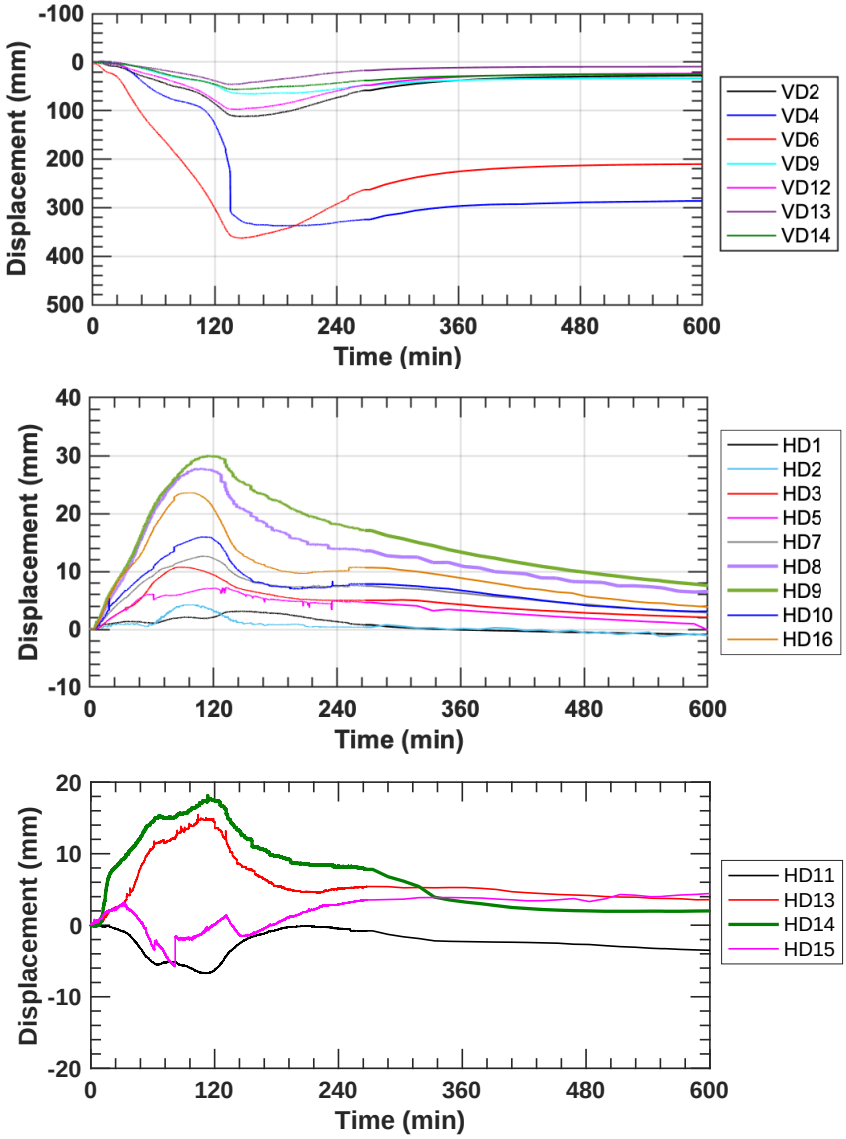

Fig. 62. Additional displacement data not included in Sect. 3.4.

Fig. 63. Video snapshots showing the test floor at 15 min and 120 min after fire ignition.

A.9. Additional Strain Measurements

Two different 120-ohm strain gauges, FLA-5-11 and QFLA-6-11 models [35] manufactured by Tokyo Measuring Instruments Lab., were mounted on the support columns and the surrounding beams to measure the change in strains in response to a compartment fire in the middle bay of the test building. Temperatures of those gauges remained below 50 °C. Locations of strain measurements are provided in Fig. 64. Column strains were measured at two levels. Strain gauges labeled with 0 through 3 were installed at 10 cm from the strong floor, and the remaining column strain gauges were installed at 34 cm from the strong floor.

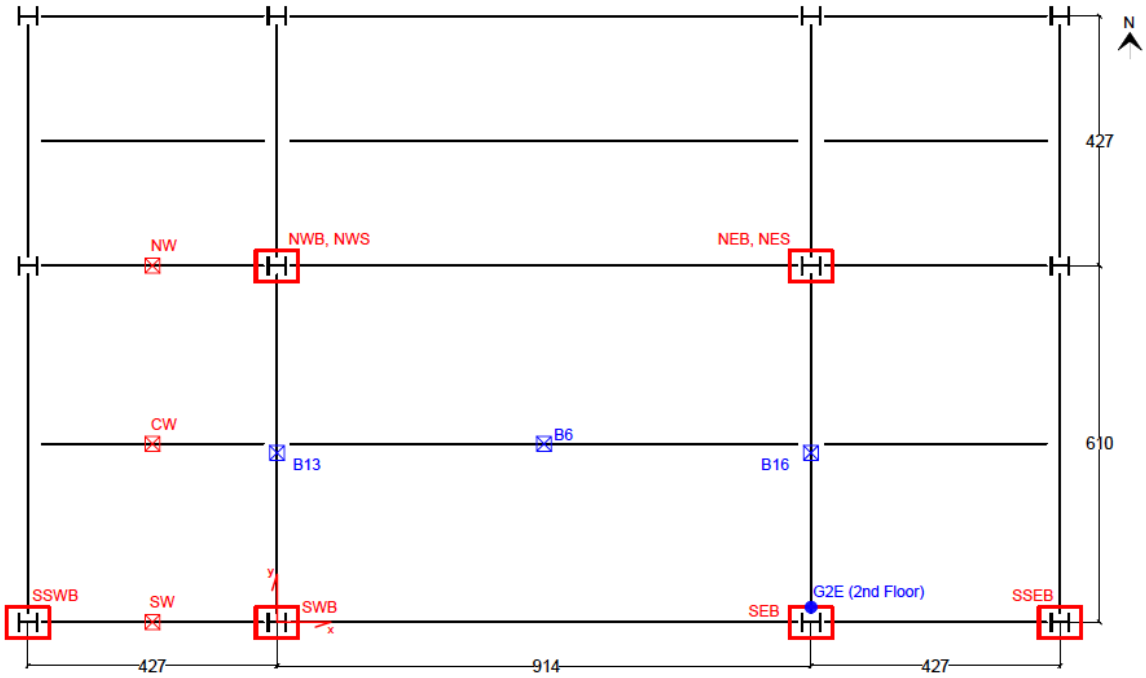

(a)

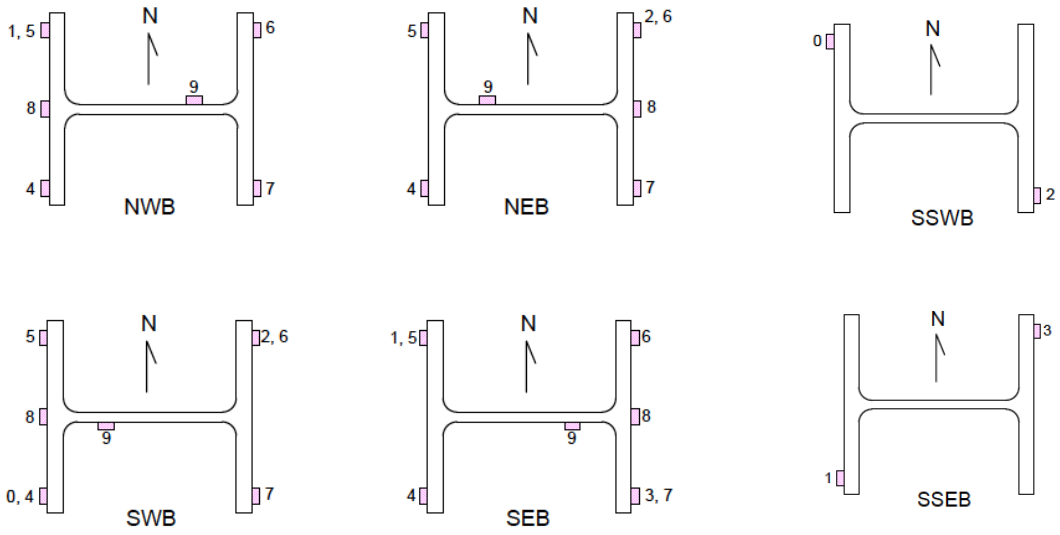

(b)

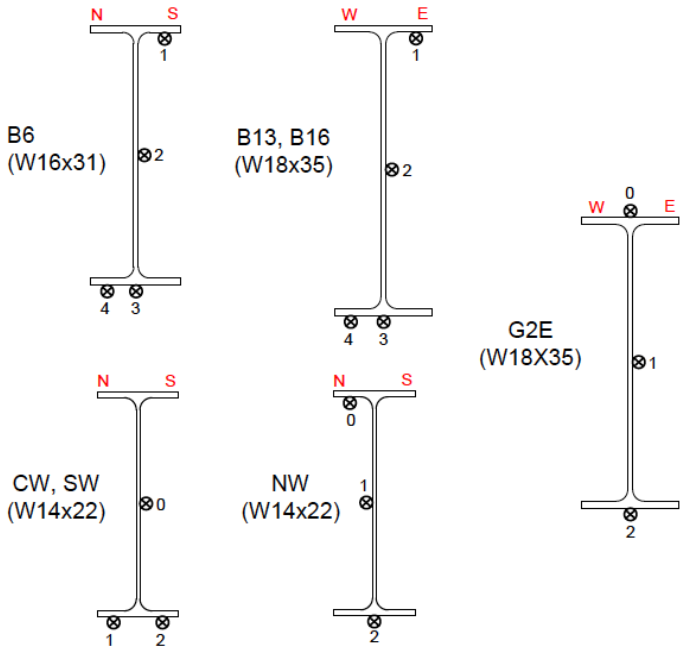

(c)

Fig. 64. (a) Locations and labels of strain measurements, (b) strain gauges installed at column base, and (c) strain gauges on the surrounding beams at the test floor level. Dimensions are in cm.

The column strains at a variety of locations are plotted in Fig. 65. As shown, the columns were subjected to variable bi-directional bending moments in response to thermal expansion or contraction of the test floor assembly. Based on the magnitude of strains, the northeast and northwest columns of the fire test bay were subjected to thermally induced lateral forces relatively smaller than those applied to the southeast and southwest columns. Local buckling of the north edge beam at their ends likely occurred around 70 min after ignition of the test fire as NWB and NEB reached their peak value at that time. Web local buckling of the girders at their ends likely occurred around 100 min when SWB and SEB reached their peak values. The strains in the west-bay beams at midspan are shown in Fig. 66. In the west-bay secondary beam, compressive forces increased until 60 min into heating and then began to decrease due to local buckling of the test-bay secondary beam. Refer to A.9 for post-test photographs of the deflected shapes of the beams and girders.

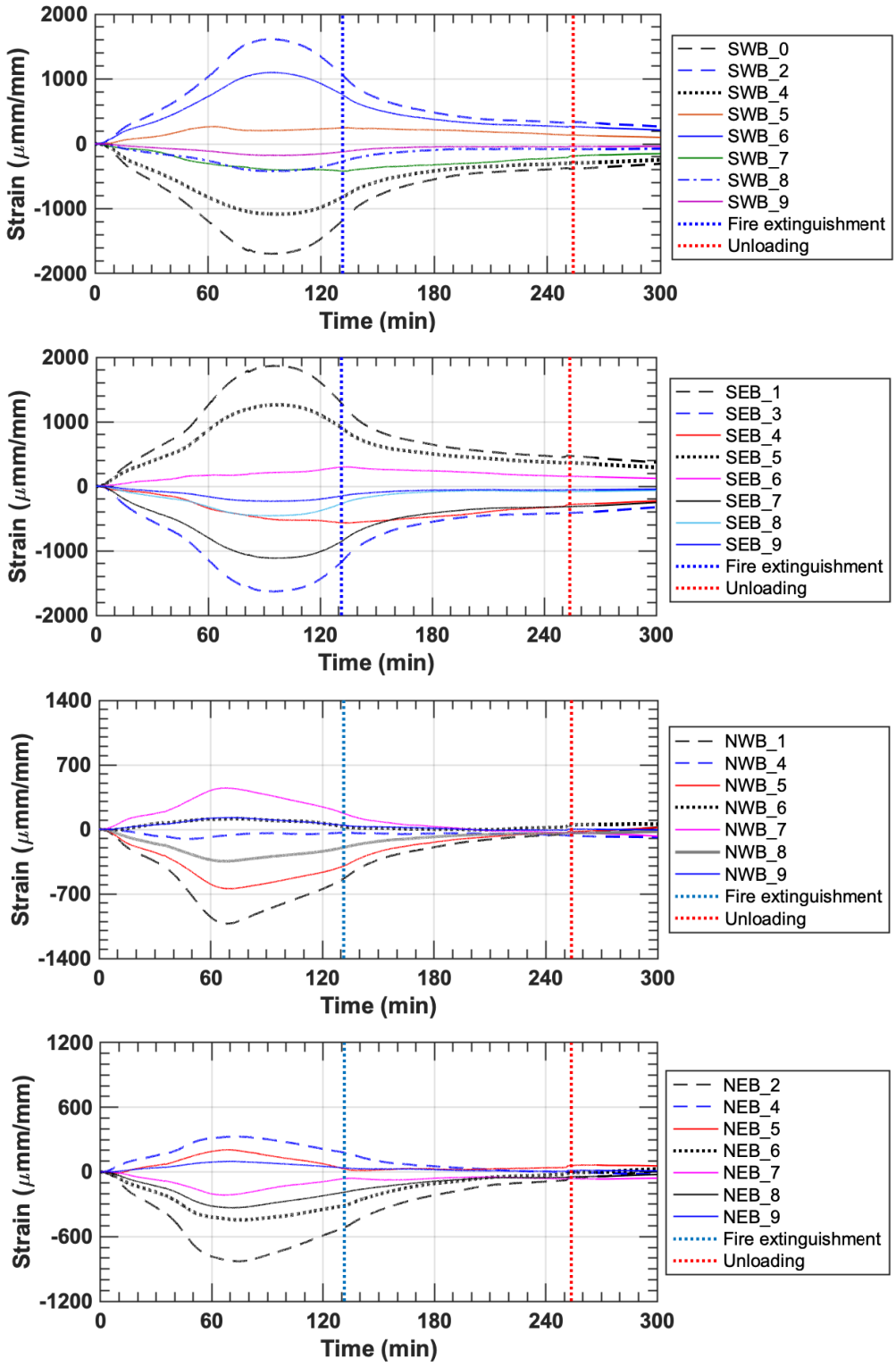

Fig. 65. Strains of test bay columns.

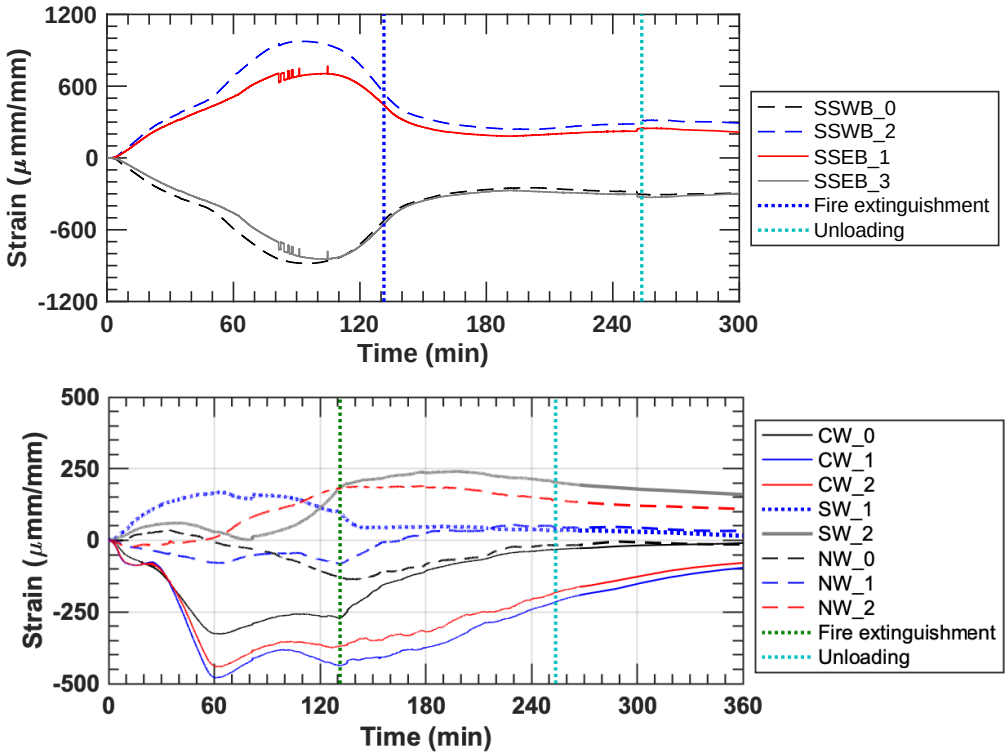

Fig. 66. Strains of surrounding columns (top) and steel beams (bottom).

A.10. Compartment Opening Velocity and Temperature

The flow of gases induced by the fire was measured at the southeast and northwest vents. A vertical array of bare bead thermocouples (Type-K) was used to estimate gas temperature at each vent. Gas velocity at selected locations was determined using bi-directional probes placed adjacent to the thermocouples. As shown in Fig. 67 and Fig. 68, three velocity probes were placed in the southeast vent and one velocity probe in the northwest vent. The pressure differential across the bi-directional probes was measured using precision capacitance manometers (MKS 220CD Baratron) [36]. Refer to Choe et al. [18] for details on the velocity measurement.

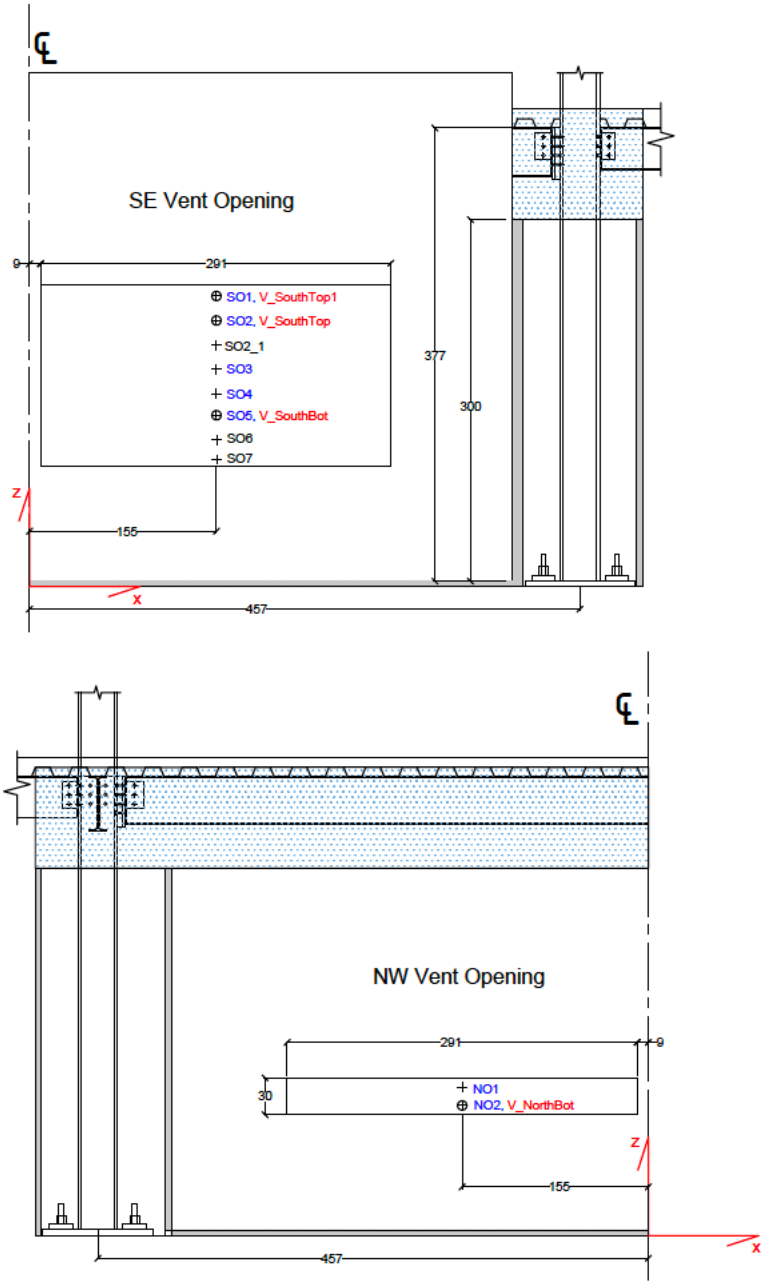

Name/ID	X East+	Z Up+
SO1	155	241
SO2	155	221
SO2_1	155	201
SO3	155	180
SO4	155	160
SO5	155	142
SO6	155	122
SO7	155	105
V_SouthBot	155	142
V_SouthTop	155	221
V_SouthTop1	155	241

Name/ID	X East+	Z Up+
NO1	-155	123
NO2	-155	108
NO3	155	123
V_NorthBot	-155	108

Fig. 67. Locations of opening velocity and temperature measurements. NO3 is located in the NE vent opening (not shown here). Dimensions and coordinates are in cm.

South opening

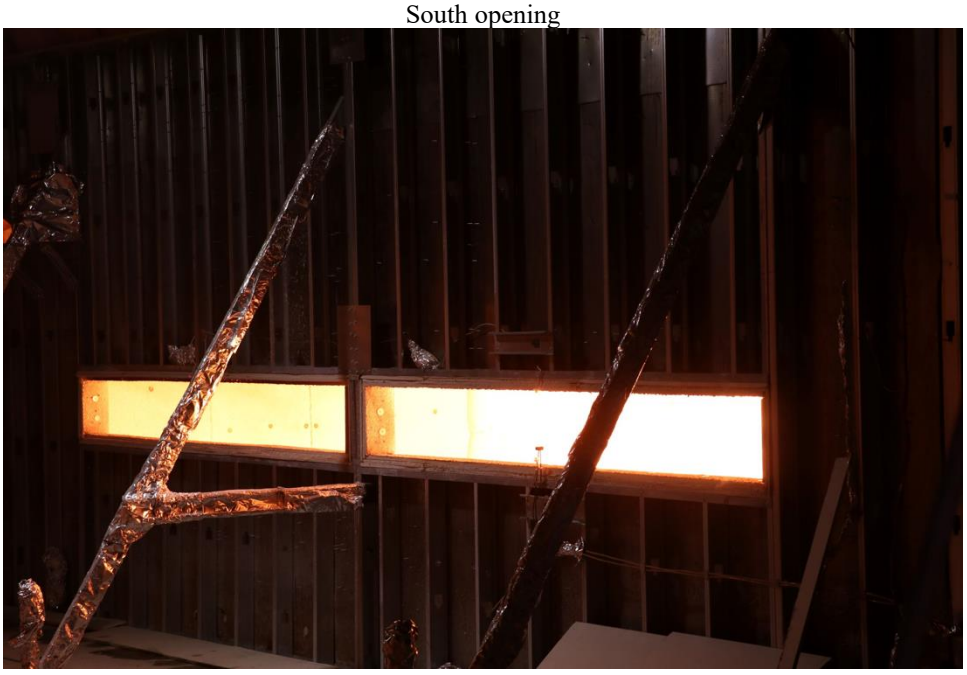

North opening

Fig. 68. Installed bi-directional probes and thermocouples on south and north vent openings of the test compartment during fire loading.

Gas temperatures and velocities measured at the south and north openings are shown in Fig. 69, along with the average upper layer gas temperature (AvgULG) measured using twelve TCC thermocouples descried in Sect A.2. Positive velocity indicates hot gases flowing out of the compartment, while negative velocity indicates ambient air flowing into the compartment.

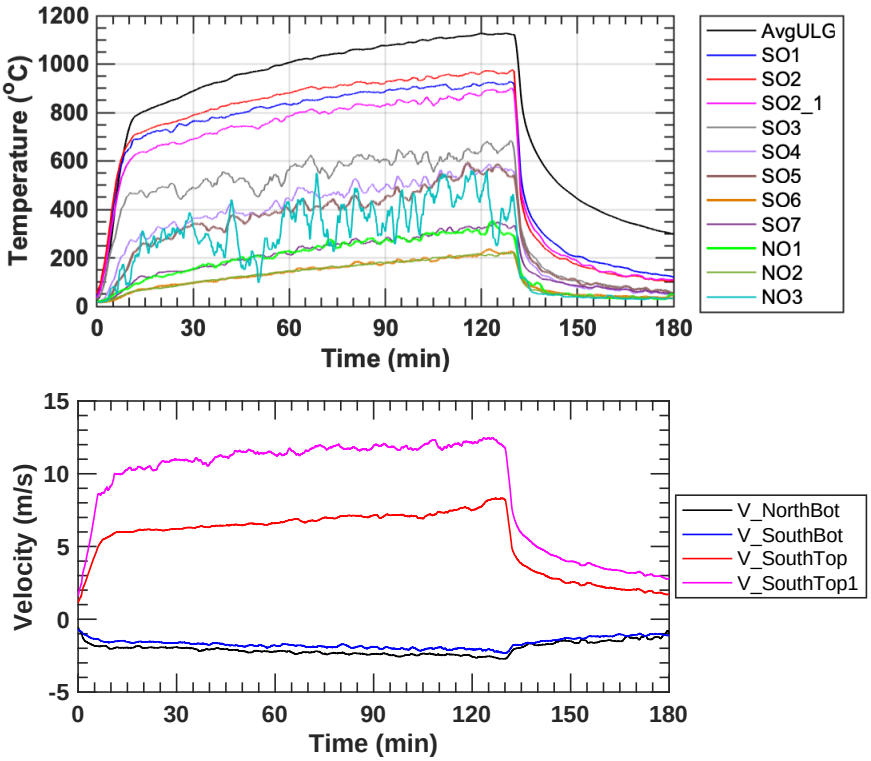

Fig. 69. Vent opening temperatures and gas velocities. Plotted are the moving average values over 120 s.

A.11. Additional Post-Test Photographs

No apparent breakout failures were identified during the initial visual inspection. Hence, the concrete slab was removed to examine the headed stud anchors at the beam ends. As shown in Fig. 70, the stud anchors only exhibited minor shear deformations although the vertical displacement of the secondary beam reached greater than the beam span/20 ratio at elevated temperatures, similar to the displacement limit prescribed in the ASTM E119 standard.

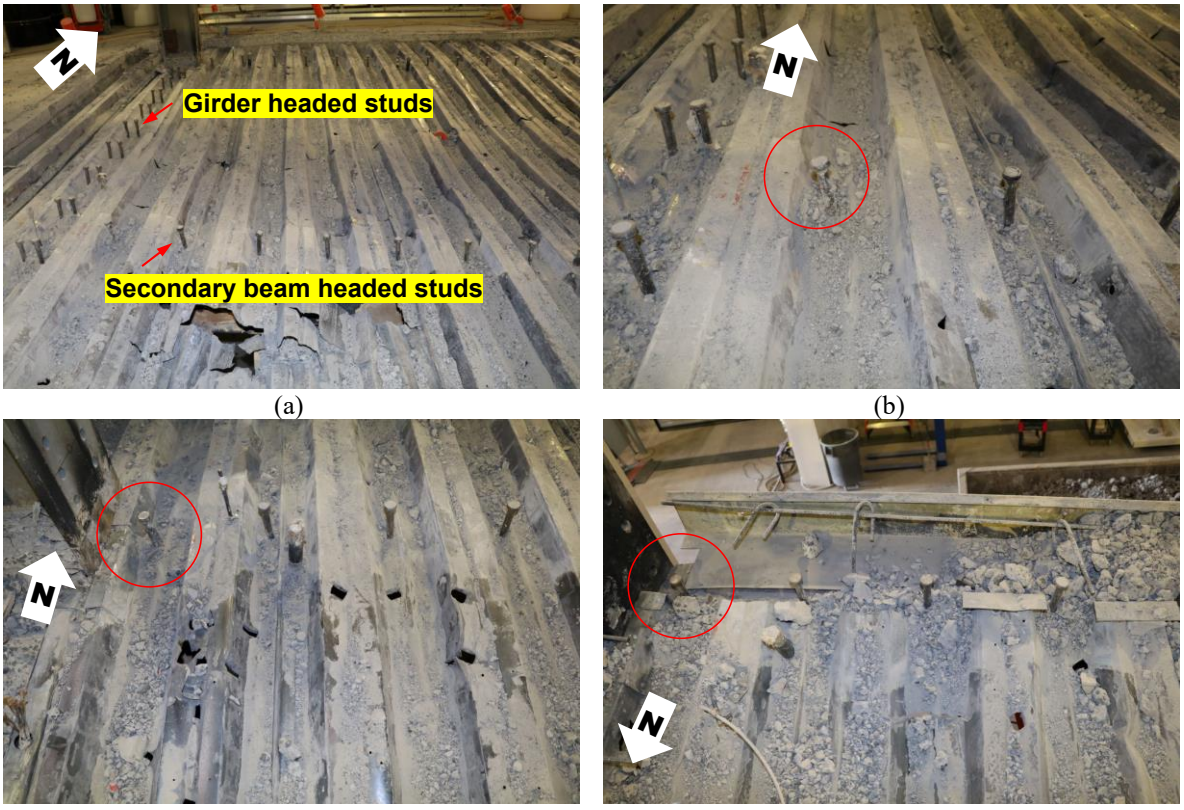

Fig. 70. Post-test photographs of headed studs after concrete removal: (a) Northwest steel decking; (b) Secondary beam; (c) North edge beam; (d) South edge beam. The beam-end stud is in a red color ring.

Some photographs of the shear tab connection after the fire test are shown in Fig. 71. Although severe flange and web local buckling was present at the ends of all three W16×31 beams, only minor deformations were identified around bolt holes and bolt shank. This was because the bottom flange of the W16×31 beams was bearing against the web of the girder or the column flange introducing large compressive forces as these beams expanded under fire loading (Fig. 71a-c). The girders had local web buckling only at their ends since the girder flange never put into contact with the web of the support columns due to a large initial setback distance and significantly stressed the bottom bolt as the girders expanded during heating.

Post-test photographs of the support beams and girders are shown in Fig. 72 through Fig. 75. It is noteworthy that the west girder exhibited a local rupture of the bottom web toe at the north end because of web local buckling (Fig. 76).

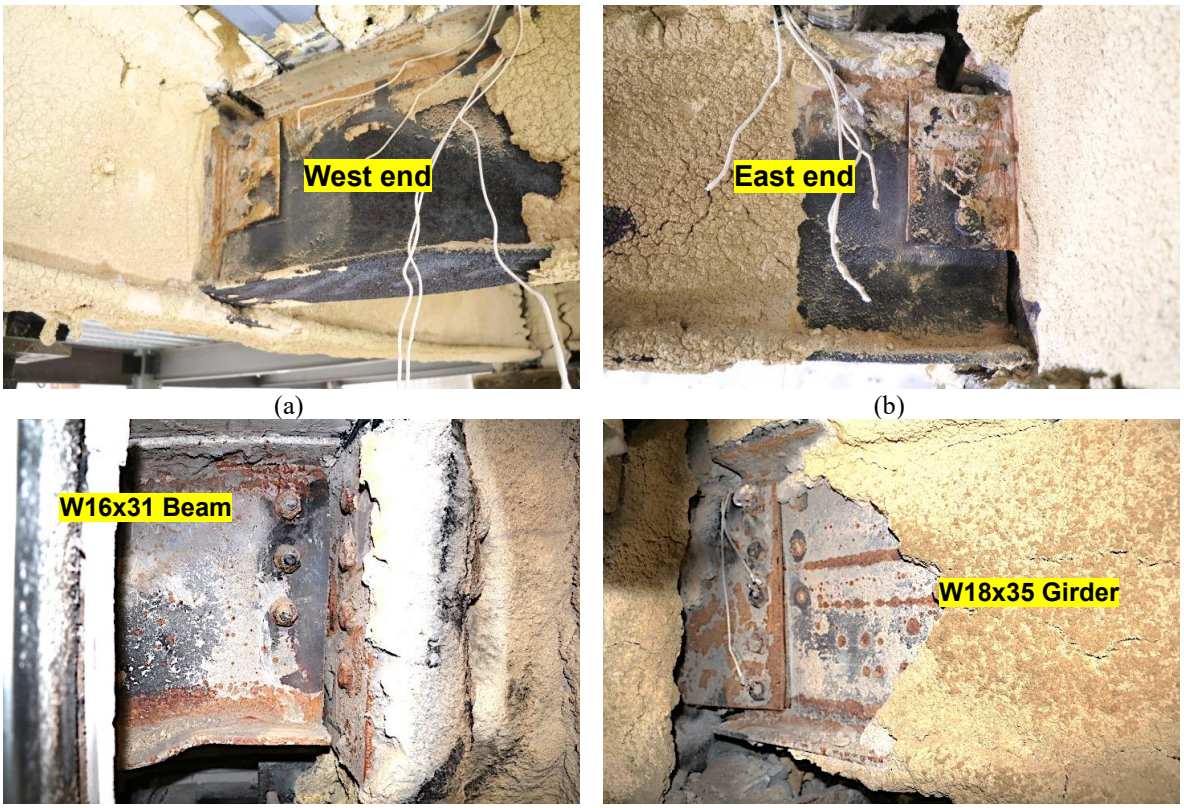

Fig. 71. Post-test photographs of shear tab connections: (a-b) secondary beam, (c) north beam, and (d) east girder. Fireproofing was removed manually.

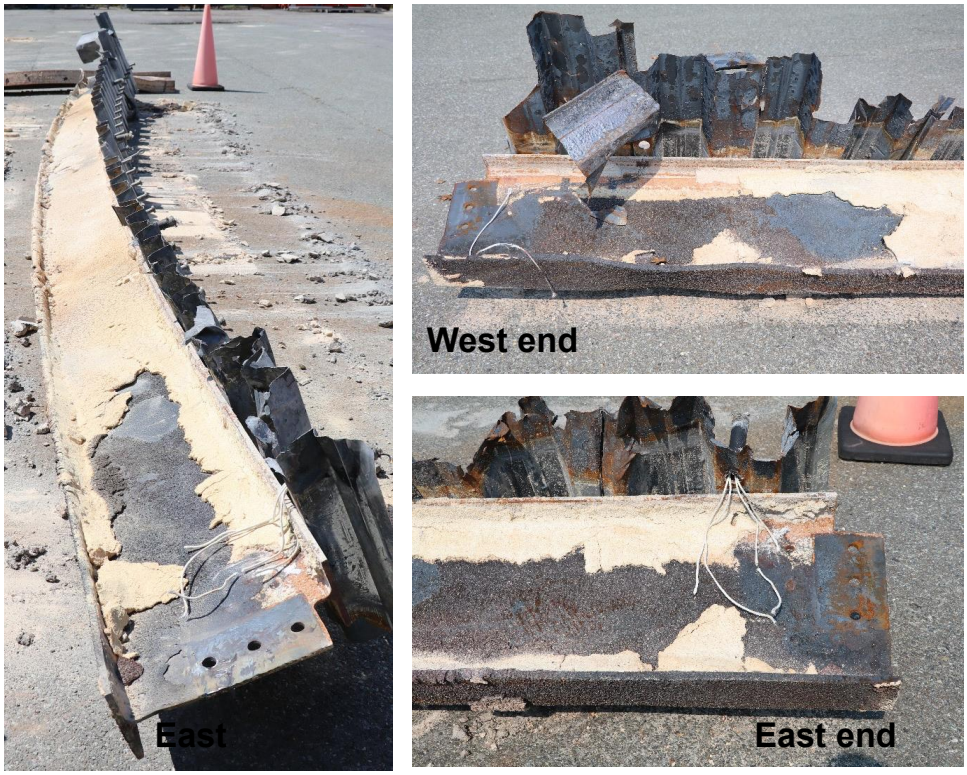

Fig. 72. Post-test photographs: Secondary beam.

Fig. 73. Post-test photographs: South edge beam.

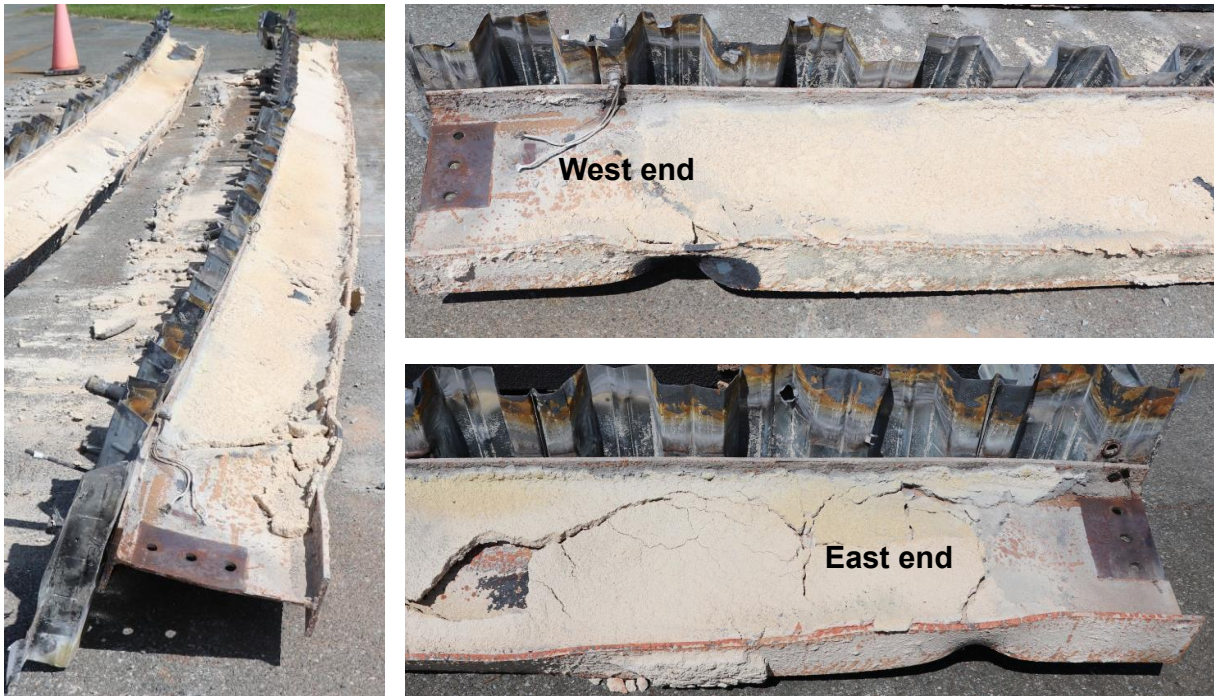

Fig. 74. Post-test photographs: North edge beam.

Fig. 75. Post-test photographs: Test-bay girders (left) and north and south ends of the west girder (right).

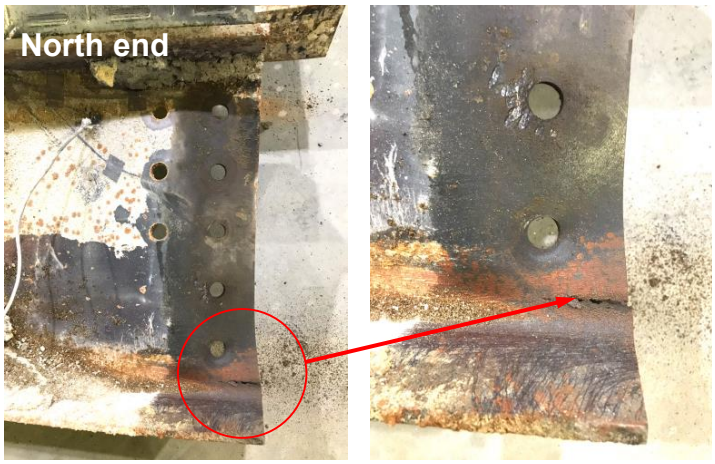

Fig. 76. Post-test photographs: West girder with rupture of the bottom web toe.

A.12. High-Temperature Discoloration of SFRM

After the fire testing, there were two spots toward the ends of the secondary beam where the fire exposed SFRM turned black and charcoal color as shown in Fig. 77. Those locations were directly above the east and west burners. A handheld XRF (X-ray fluorescence) analyzer manufactured by Olympus [37] was utilized to measure chemical compositions of the samples collected from the secondary beam at two different locations (the west end and midspan) after cooling. A comparison of some scanned results is shown in Fig. 78, along with the unused SFRM powder. Although a further study is needed, this SFRM discoloration was likely caused by high-temperature oxidation or phase change of the steel heated beyond 1000 °C. Refer to TB5 and TB7 temperatures in Sect. A.6. The charcoal-colored sample contained about 51 % iron by mass, whereas the unused sample or other exposed sample contained about 2 %.

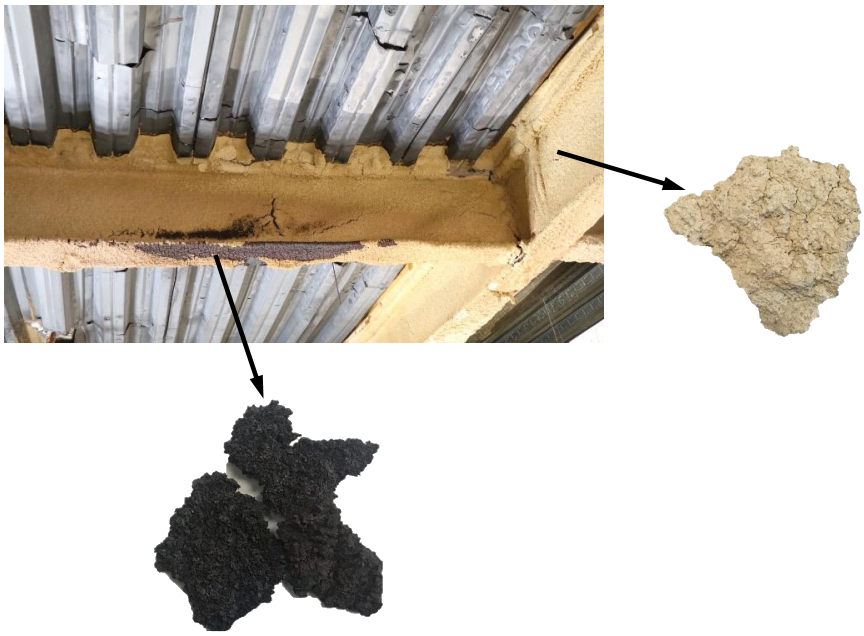

Fig. 77. Samples of fire exposed SFRM applied on the support steel beam framing.

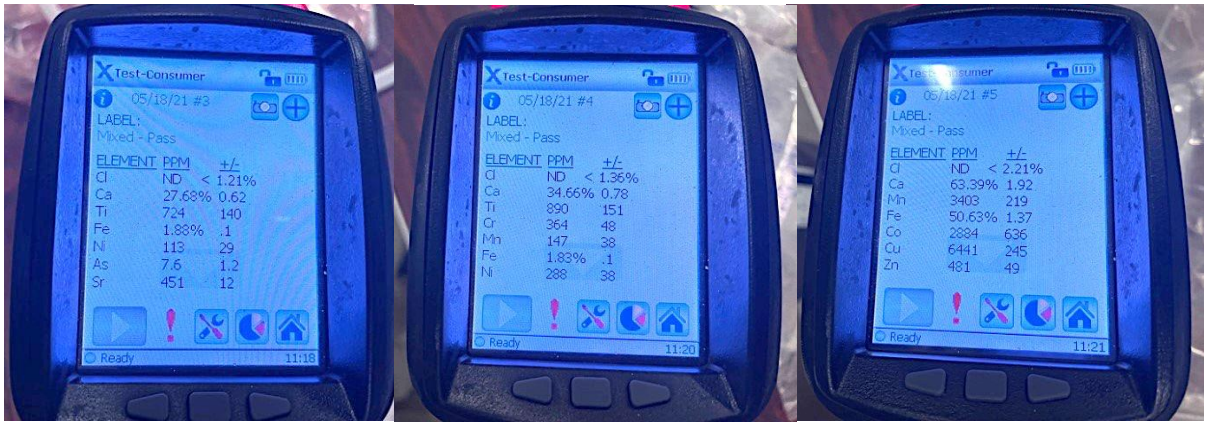

Southwest Type 5MD Powder (Color: Tan) | SFRM Sample @ Midspan (Color: Beige) | SFRM Sample @ West End (Color: Black)

Fig. 78. Chemical compositions of SFRM samples measured using a handheld XRF analyzer